

Quantum Dot Josephson Junctions in the Kondo Regime

Inauguraldissertation

zur
Erlangung der Würde eines Doktors der Philosophie
vorgelegt der
Philosophisch-Naturwissenschaftlichen Fakultät
der Universität Basel

von

Alexander T. Eichler
aus Basel BS



Basel, 2010

Genehmigt von der Philosophisch-Naturwissenschaftlichen Fakultät
auf Antrag von
Prof. Dr. C. Schönenberger
Prof. Dr. J. Nygård
Dr. M. Weiss

Basel, den 08. Dezember 2009

Prof. Dr. Eberhard Parlow
Dekan

Für dich, Nadine

Contents

Introduction: A New Set of Rules	vii
1 Theory	1
1.1 Electrical conduction through carbon nanotubes	1
1.2 Carbon nanotube quantum dots	3
1.3 The Kondo effect	8
1.4 The BCS theory of superconductivity	11
1.5 Andreev transport	14
1.6 The proximity effect	16
1.7 The Josephson junction	17
2 Fabrication and Measurement Methods	23
2.1 General device fabrication	23
2.2 Topgated carbon nanotube devices	25
2.3 Topgated nanowire devices	26
2.4 Final steps	26
2.5 Room temperature measurements	28
2.6 Measurements at low temperature	29
3 Even-Odd Andreev Transport due to the Kondo Effect	35
3.1 Introducing remarks	36
3.2 Results	36
3.3 Even charge state	40
3.4 Odd charge state	40
3.5 Summary	42

4	Tuning the Josephson Current With the Kondo Effect	45
4.1	Introducing remarks	45
4.2	Setup details and junction parameters	47
4.3	Results	47
4.4	Additional data	54
4.5	Summary	57
5	Topgated Ge/Si Nanowires with Superconducting Leads	59
5.1	Introducing remarks	59
5.2	Results	60
5.3	Summary	65
6	Topgated Carbon Nanotubes with Superconducting Leads	67
6.1	Introducing remarks	67
6.2	Results for device A	69
6.3	Results for device B	72
6.4	Conclusion for devices A and B	78
7	Summary and Outlook for Chapters 3-6	81
8	AMR Measurements in Thin Films	83
8.1	Introducing remarks	83
8.2	The anisotropic magnetoresistance effect	84
8.3	Sample preparation	85
8.4	Measurement setup	85
8.5	Results for ‘AMR 4a’	86
8.6	Results for ‘AMR 6b’	88
8.7	Summary	90
A	Fabrication and Measurement Information	99
	Publication List	105
	Curriculum Vitae	107
	Acknowledgements	109

Introduction: A New Set of Rules

Nanoscale electronics enjoys continuous attention due to its proximity to information technology. Driven by an unbroken craving for smaller and faster building blocks, semiconductor industry keeps stretching the limits of what is technologically feasible regarding the fabrication and application of silicon transistors. With the rapid progress of miniaturization, these devices have already left the realm of pure classical physics, and are entering that of quantum mechanics. Information technology will have to face a new set of rules, where electrons, carriers of charge information units, engage in a highly correlated dance that qualitatively modifies the overall electrical behaviour of transistors. Of course, this is not only a challenge, but also an opportunity for revolutionary new concepts. Major technology companies have long ago started to investigate the physics of strongly correlated electron systems, often in close collaboration with academic research.

Two of the most topical phenomena in this context are superconductivity and the Kondo effect. Both rely on the formation of a new ground state for electrons, both have dramatic consequences for electrical transport at low temperatures, and both were initially discovered and observed in extended structures. While superconductivity relates to diffusion free transport ensuing from the creation of multiple electron pairs, the Kondo effect manifests itself as a cloud of localized conduction electrons around a single magnetic impurity. With the advent of nanoscale fabrication techniques, it is now possible to study such effects at the level of individual electronic states. Quantum dots, artificial structures in which electrons behave essentially as inside an atom, are used as highly versatile and precise tools by experimental physicists. Unlike bulk materials, quantum dots offer the chance to tune nearly all relevant parameters of the system. Measurements of the electrical transport through individual states in a quantum dot present information about the physics governing these states, and their response to changes in the system parameters.

In this thesis, we will look at measurements that were performed dur-

ing my PhD studies in the group of Christian Schönenberger in Basel. By attaching superconducting electrodes to a quantum dot, we realize a Josephson junction, where supercurrents pass through a short constriction of non-superconducting material. In our case, this happens to be a set of energetically discrete electronic states. By application of a gate voltage, we control the sequential filling of these states, creating a situation that gives rise to the Kondo effect. Thus, we are able to study the interplay between the Kondo effect and superconductivity in great detail.

Chapter 1 presents an overview of the theoretical concepts that are used throughout the thesis. Chapter 2 describes the device fabrication, including the growth of carbon nanotubes as basic material for quantum dots. The results of our experimental work are presented in chapters 3-6, followed by a summary and outlook. Finally, chapter 8 gives an account of a side project concerned with measurements on the anisotropic magnetoresistance in thin films. Since the topic is not directly related to the main part of this thesis, it is presented as a stand-alone segment.

It is with a great sense of joy and satisfaction that I look back on my time in this group, because I had the chance to work in such a motivating environment on such a fascinating project. I can only hope that some of this joy is transferred to the reader, because ultimately, I believe it is joy that drives us onwards.

Chapter 1

Theory

1.1 Electrical conduction through carbon nanotubes

Single-wall carbon nanotubes (SWCNT) combine a number of interesting features that place them among the most versatile model systems for electrical transport experiments in mesoscopic physics[1; 2]. The atomic structure of SWCNTs resembles that of a single sheet of graphene rolled into a seamless cylinder (Fig. 1.1), and the precise roll-up direction and diameter determine whether it is metallic or semiconducting. Carbon nanotubes often grow in bundles or ropes, or they appear nested within each other, which we refer to as multi-wall carbon nanotubes (MWCNT). A more complex atomic structure obviously results in a more intricate electronic behaviour. We will limit our discussion to SWCNTs as the most desirable material for transport experiments on a single-electron level.

Individual SWCNTs can easily be contacted to metallic leads. By depositing two electrodes onto a previously selected SWCNT, a junction is created between source (S) and drain (D) electrodes, which in general can consist of a normal metal, a ferromagnet, or even a superconductor (Fig. 1.2a)[3; 4; 5]. In the next section, we will look at the formation of tunnel barriers at the SWCNT/lead interfaces and the consequences resulting from it. At this point, though, we treat the interfaces as perfectly transparent contacts. The diameters of SWCNTs range from less than one to few nanometers, and their length is typically of the order of several micrometers, which makes it possible to define the leads in a top-down approach. Throughout this thesis, we will assume that the substrate underneath the device consists of highly doped Si which can be used as a backgate electrode (BG). A 400 nm

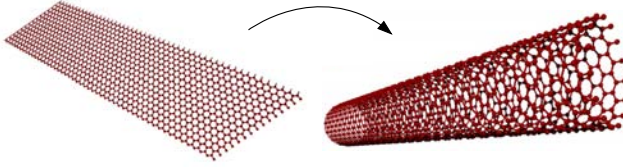


Figure 1.1: The structure of an SWCNT is that of a single sheet of graphene rolled into a cylinder. Illustration by courtesy of Dino Keller.

thick layer of SiO_2 serves as an isolation between the BG and the device (Fig. 1.2b). The fabrication process and material properties are explained in more detail in chapter 2. When the mean free path of charge carriers in the carbon nanotube, l , exceeds its circumference, the situation is that of a one-dimensional conductor between two bulk metals with just one conduction channel[6; 7]. In a SWCNT, this conduction channel is fourfold degenerate due to the spin degree of freedom and the orbital degeneracy, which can intuitively be accounted for by the two orientations around the SWCNT circumference (clockwise and anti-clockwise)[8].

The electronic mean free path l in a metallic SWCNT can exceed $1 \mu\text{m}$ [9]. For a nanotube segment with length $L < l$, an electron does not scatter on its way between the two leads and the SWCNT acts as a ballistic conductor with a vanishing four-point resistance. However, the two-point resistance will not drop below a universal value independently of l . The corresponding voltage drop takes place at the interface between the leads and the SWCNT, where a current is redistributed from many channels in a lead to the four channels available in the SWCNT. The conductance G following from this is captured in the Landauer-Büttiker formalism[10; 11] that describes charge transport through M transport channels with a respective transmission of T ($0 \leq T \leq 1$):

$$G = \frac{e^2}{h} \sum_{i=1}^M T_i \quad (1.1)$$

Here, e is the electron charge. In the case of perfect transmission ($T = 1$) at the interface, this formula yields a maximum conductance of $4 \frac{e^2}{h}$ for a SWCNT sample with four channels, corresponding to a resistance of $6.45 \text{ k}\Omega$.

In order to observe the rich physics of charge transport through quantum dots, though, it is necessary to introduce tunnel barriers at those interfaces, which will decrease the transmission ($T < 1$).

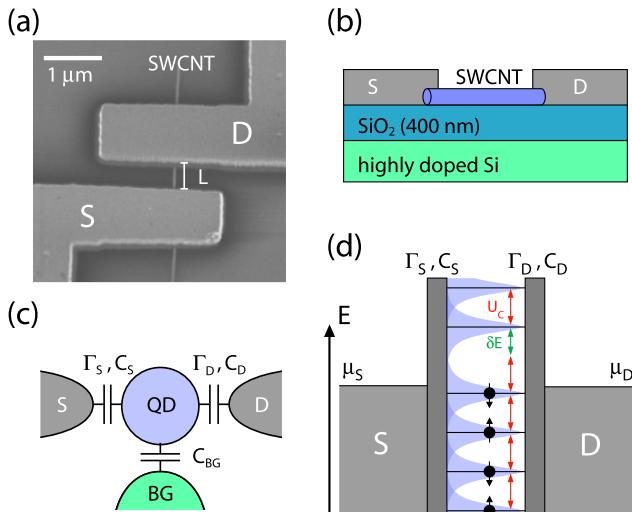


Figure 1.2: **a** Scanning electron microscope (SEM) picture of a SWCNT contacted to source (S) and drain (D) electrodes. The section of the nanotube bridging the gap between S and D, L , defines the size of the resulting QD. **b** The highly doped Si substrate serves as a backgate electrode (BG). **c** Schematic of a QD with S and D leads and a capacitively coupled BG. **d** The discrete electronic levels on the QD are separated by the orbital energy δE and the charging energy U_C .

1.2 Carbon nanotube quantum dots

In any real device, tunnel barriers form at the contact interfaces. The height of these barriers depends in a critical fashion on the lead metal, the purity of the interface, the diameter of the contacted SWCNT, and on whether the SWCNT is semiconducting or metallic (see fabrication for details). The Schottky barrier[12] appearing at a metal-semiconductor interface is responsible for the fact that semiconducting SWCNTs typically have a much higher two-point resistance than metallic ones.

A SWCNT contacted to source and drain electrodes via tunnelling contacts is a prime example of a ‘quantum dot’ (QD)[13; 14]. Electrons from the leads can enter or leave the QD by tunnelling through the barriers at the interfaces, which are characterized by their coupling strength, $\Gamma_{S,D}$, and the capacitance of the QD to the corresponding lead, $C_{S,D}$ (Fig. 1.2c). The tunnelling rates through the barriers equal $\Gamma_{S,D}/\hbar$. Inside a quantum dot, the electrons are spatially confined in three dimensions and can only occupy a set of discrete states for which they exist as standing waves (Fig. 1.2d). The energy that separates these states is denoted ‘orbital energy’ in analogy to the discrete electronic states of an atom, and will be written as δE . The four electrons residing in one of these orbital states are again separated in energy due to the Coulomb interaction arising between them, so the state splits up into four levels¹. Every electron approaching the QD will feel a repulsion due to the charge of the electrons already dwelling there. This Coulomb repulsion, or ‘charging energy’, is written as U_C , and relates to the total capacitance C_{tot} of the QD as $U_C = \frac{e^2}{2C_{tot}}$. Generally, U_C can in good approximation be regarded as constant in metallic SWCNTs.

At this point, it is interesting to remark that while δE is a manifestation of quantum mechanics, U_C relies on a purely classical process. However, the charging energy of a single electron is much too small to appear in a typical macroscopic measurement. It is only due to the mesoscopic size of a QD, and the correspondingly small capacitance C_{tot} , that we can observe single electron charging in such a system.

Let us now take a look at electrical transport through a QD. We assume that the leads consist of a normal metal with an energy-dependent electronic occupation given by the Fermi-Dirac probability distribution function:

$$f_{FD}(E) = \frac{1}{e^{\frac{E-\mu}{k_B T}} + 1} \quad (1.2)$$

Here, E is energy, k_B the Boltzmann constant, T the temperature, and μ the chemical potential, which in general can be different for the two leads. At low temperatures, this distribution function becomes very sharp, so we can treat it as a step function, with all available electronic levels occupied below μ and none above it. In Fig. 1.2d, this is represented by grey and white areas, respectively. All levels on the QD with an energy below or equal to μ will then be filled, and all higher levels empty. As illustrated by blue Lorentzian shapes, each level is energy-broadened due to $\Gamma = \Gamma_S + \Gamma_D$. This can be understood in terms of the Heisenberg uncertainty principle $\Delta E \Delta t \gtrsim \frac{\hbar}{2}$,

¹In a real device, defects in the atomic structure often lift the K-K’ degeneracy, which leads to twofold degenerate orbitals

which states that a process lasting a time Δt may violate classical energy conservation up to ΔE . In our example, if the total tunnelling rate Γ/\hbar is large, electrons stay on the QD only for a short time Δt and can borrow an energy ΔE to enter a level that lies above $\mu_{S,D}$ and is classically inaccessible.

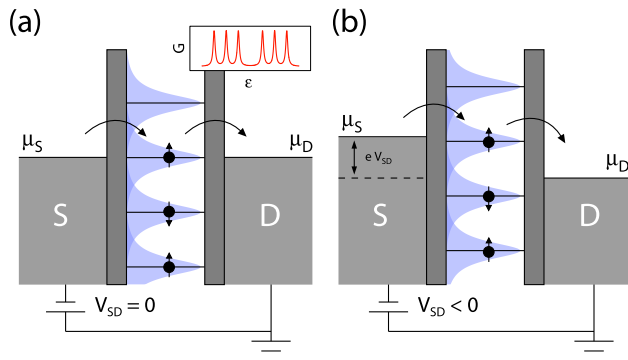


Figure 1.3: **a** A measurement of G versus the level position ϵ shows a peak whenever a level is aligned with μ_S and μ_D . In an experiment, ϵ is controlled by applying a voltage V_{BG} to the BG. **b** A negative voltage V_{SD} applied to S shifts μ_S upwards.

Electrical transport takes place if an electron can enter the QD from one lead (S) and leave it towards the other (D). In the QD regime, $\Gamma < U_C, \delta E$, so neighbouring levels overlap only slightly. As a consequence, transport of an electron from S to D requires that a level is aligned with $\mu_{S,D}$, as depicted in Fig. 1.3a. If the chemical potential of the leads lies in the middle of two levels, electrons cannot enter and leave the QD at will, so transport is low. As a function of the level position ϵ , the conductance G through the QD will therefore oscillate between peaks (‘on resonance’) and valleys (‘off resonance’). This results in the so-called ‘Coulomb oscillations’ which are shown in the inset of Fig. 1.3a. Usually, ϵ is controlled by a BG that is capacitively coupled to the QD (Fig. 1.2c). Since the voltage applied to the BG, V_{BG} , is directly accessible in an experiment, we will from now on speak in terms of V_{BG} instead of ϵ . In addition, the small overlap between neighbouring levels means that only one channel is effectively available for electrical transport, even though the orbital is fourfold degenerate. Intuitively, it is obvious that as soon as an electron occupies one of the four levels, the other three are shifted upward by U_C and cannot partake in transport. The large charging energy thus reduces the maximum conductance on resonance to e^2/h rather than $4e^2/h$.

So far, our discussion was limited to equilibrium transport, i.e. $\mu_S = \mu_D$. We will now consider the effects of a bias voltage (V_{SD}) applied to the leads, such that $\mu_S = \mu_D + eV_{SD}$ (Fig. 1.3b). Note that D is on ground potential while V_{SD} is applied to S, and that due to the negative electron charge e , a negative V_{SD} shifts μ_S upwards and vice versa. In this case, all levels on the QD lying between μ_S and μ_D can partake in electron transport, and G increases whenever a new level enters this window. In the following, we will use G to denominate the **differential** conductance dI/dV instead of the linear conductance $\Delta I/\Delta V$. As long as $V_{SD} = 0$ or for conductors with a linear I/V curve, there is no difference between the two quantities, but for nonlinear I/V curves, dI/dV produces a peak whenever $\Delta I/\Delta V$ increases, which facilitates the graphical representation of data. In a measurement of G as a function of V_{SD} and V_{BG} , alignment of a level with μ_S or μ_D will result in ridges of high differential conductance, as marked by blue lines in Fig. 1.4. These high differential conductance lines form a characteristic pattern, the so-called ‘Coulomb blockade diamonds’ (CB diamonds). Inside a CB diamond, electron transport is blocked because no level is within the energy window defined by μ_S and μ_D . All levels below μ_D are filled, and all levels above μ_S remain empty, so the number of electrons on the QD is a fixed integer N . Since CB diamonds correspond to regions where the QD is stable against charge fluctuations, such a graph is often referred to as a ‘charge stability diagram’. By driving V_{BG} to more positive voltages, a new level becomes accessible, and the number of electrons on the QD changes from N to $N + 1$ (bright grey to dark grey diamond). For zero bias voltage ($V_{SD} = 0$), the transition from N to $N + 1$ takes place exactly at the nodes of two adjacent CB diamonds, and a measurement of G versus V_{BG} restores the familiar Coulomb oscillation pattern (red graph at the top).

The charge stability diagram of a QD holds much information about the energy scales involved. From the size of a CB diamond, we can estimate U_C , and the additional size of every fourth diamond corresponds to δE . The full width at half maximum (FWHM) of a CB peak yields Γ as long as $k_B T \ll \Gamma$. Furthermore, we can extract the various capacitances by looking at the slopes of a diamond, because they determine the efficiency of V_{BG} , i.e. how much voltage we have to apply to the BG in order to shift ϵ by a certain amount. Fig. 1.5 illustrates this in detail. In situation **1**, S and D are on the same potential and aligned with one level on the QD (bright blue). If we apply a negative voltage V_{SD} to S, μ_S shifts upwards while μ_D remains fixed on ground potential. The capacitive coupling of S to the QD induces a gating effect that shifts ϵ by $eV_{SD} \frac{C_S}{C_{tot}}$. In order to restore alignment of the level with D, which is the condition for resonant tunnelling, we need to apply a negative voltage to the BG such that $\Delta V_{BG} \frac{C_{BG}}{C_{tot}} = -\Delta V_{SD} \frac{C_S}{C_{tot}}$. The slope s_- of the bright blue line leading from situation **1** to **2** is therefore

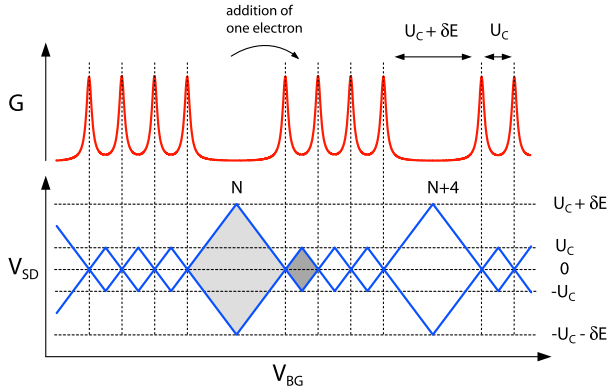


Figure 1.4: A measurement of G versus V_{SD} and V_{BG} shows a peak whenever a level is aligned with μ_S or μ_D . The resulting characteristic pattern (‘Coulomb blockade diamonds’) is drawn in blue. Each diamond corresponds to an integer number of electrons on the QD, and its size is determined by U_C and δE .

$\frac{\Delta V_{SD}}{\Delta V_{BG}} = -\frac{C_{BG}}{C_S}$. In situation **2**, $eV_{SD} = U_C$, and S is aligned with the upper level (dark blue).

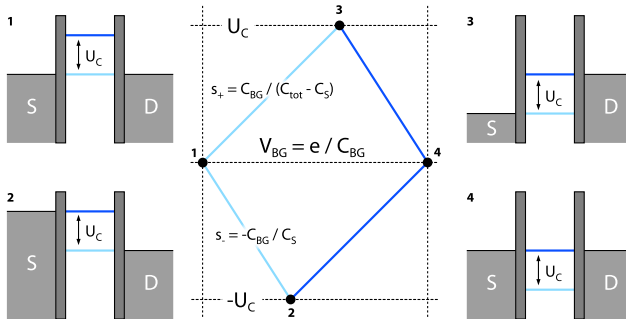


Figure 1.5: The slopes of the sides of a diamond are determined by the capacitances of the QD to S, D, and the BG. If V_{SD} is changed, V_{BG} must be driven accordingly to keep the level aligned and thus meet the condition for resonant tunnelling.

We can calculate the slope s_+ leading from **1** to **3** in a similar way. A

positive V_{SD} will lower μ_S and shift ϵ downwards by $eV_{SD} \frac{C_S}{C_{tot}}$. The level is aligned with S once more if we apply $\Delta V_{BG} = \Delta V_{SD} (1 - \frac{C_S}{C_{tot}}) \frac{C_{BG}}{C_{tot}}$, and the slope s_+ is consequently $s_+ = \frac{C_{BG}}{C_{tot} - C_S}$. From **2** (**3**) to **4**, it is the alignment of the upper level with S (D) that is responsible for the resonance condition, so the lines connecting the two edge points are drawn in dark blue. The slopes are calculated analogously to the examples above, and turn out to be s_- (**2** to **4**) and s_+ (**3** to **4**).

1.3 The Kondo effect

The Kondo effect was first studied in bulk metals. It was found that magnetic impurities can drastically influence the conductance through a metal. An explanation was brought forward by Kondo that suggests the formation of a many-body ground state[15]. In recent years, the Kondo effect has experienced a revival in mesoscopic physics thanks to the tunability of QD systems[16; 17; 18]. In a QD, it is possible to control the parameters that are responsible for the Kondo effect, and thus test many theoretical predictions.

Whenever the number N of electrons occupying the QD is odd, the QD will carry an unpaired spin $s = 1/2$, in contrast to $s = 0$ for even N . The magnetic moment of an unpaired spin will act like a magnetic impurity in a bulk metal, and enhance the electrical transport through the QD. Below the so-called Kondo temperature T_K , the spins of the electrons in S and D will start screening the magnetic moment on the QD. They will form a many-body spin singlet state extending over both leads and the QD ('Kondo state'). The screening is achieved by high-order spin-flip processes through the QD, such that the effective mean value of the spin is $s = 0$ for timescales much longer than one of these events. In addition to screening the unpaired spin on the QD, these spin-flip processes open up an additional conductance channel through the QD that manifests itself in resonances at the tunnel barriers. The resonances are pinned to μ_S and μ_D (Fig. 1.6a). For $V_{SD} = 0$, these two resonances are aligned, and a peak in G is observed. It is important to understand that the Kondo effect does not require the QD level to be resonant. As long as the spin singlet state prevails, the conductance channel will be accessible for transport even far away from resonance. As a result, a ridge of high differential conductance ('Kondo-ridge') is observed throughout a CB diamond with odd N (Fig. 1.6b).

For $V_{SD} \neq 0$, the two resonances follow μ_S and μ_D and lose their alignment. The virtual states needed for the spin-flip processes acquire a finite lifetime, resulting in a suppression of the resonance peak amplitude. An applied magnetic field B will cause a splitting of the energies for 'spin-up' and 'spin-down' levels and, accordingly, a splitting of the resonance peaks with

the Zeeman energy $E_{Ze} = \frac{1}{2}g\mu_B B$ [18; 19]. Here, μ_B is the Bohr magneton, and $g = 2$ the Landé factor. The splitting of the Kondo resonances reflects the fact that the level degeneracy on the QD is lifted, and a finite energy is necessary to enable spin-flip processes. For $V_{SD} = \pm 2E_{Ze}/e$, this energy is provided by the potential difference between μ_S and μ_D , whereupon two of the split resonances are again aligned (Fig. 1.6c). We see therefore a splitting of the Kondo ridge in the stability diagram, corresponding to $V_{SD} = \pm g\mu_B B/e$ (Fig. 1.6d).

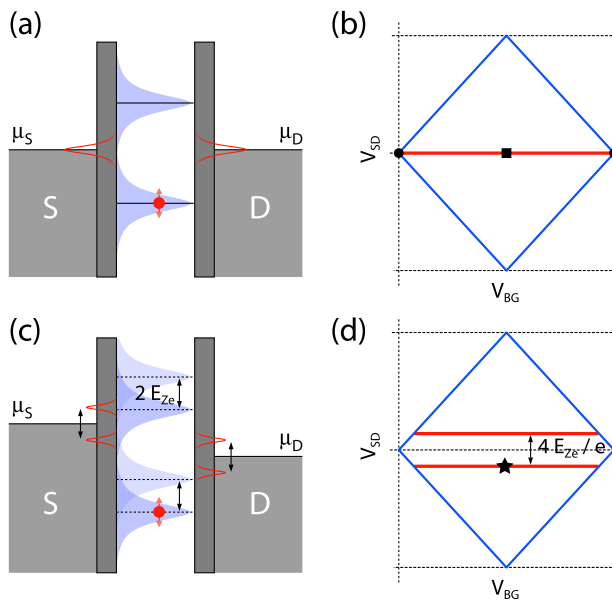


Figure 1.6: **a** Schematic of the Kondo effect. The unpaired spin on the QD is screened by electron spins in the leads, and a spin singlet state forms. Additional resonances appear at the tunnel barriers due to the hybridization of electrons in S and D. **b** For $V_{SD} = 0$, the two resonances are aligned, and a peak in G is observed throughout the CB diamond, the so-called ‘Kondo-ridge’. The black symbols designate $\epsilon = 0$ (square) and $\epsilon = \pm U_C/2$ (dots). **c** A magnetic field causes a splitting of the QD levels with the Zeeman energy E_{Ze} (black arrows), and thus a splitting of the Kondo resonances at the tunnelling barriers. **d** The Kondo ridge splits into two components at $V_{SD} = \pm g\mu_B B/e$. A black star marks the situation shown in Fig. 1.6c.

A theoretical understanding of the Kondo effect arises from the Anderson

model. It describes a single, localized orbital (QD) between two electron reservoirs (S, D). Tunnelling of electrons between the reservoirs and the orbital is allowed, and the occupation of the orbital, N , can take values of 0, 1, or 2. Due to the Pauli principle, two electrons can only coexist in the orbital if they have opposite spins, such that the total spin on the QD amounts to $s = 0$. Interaction with all other orbitals is neglected. For $N = 1$, the Anderson model predicts the formation of a Kondo spin singlet state as discussed above. The binding energy of this many-body state is identified as $k_B T_K$, where k_B is the Boltzmann constant. Above T_K , the Kondo singlet state is broken up by thermal excitations.

Solutions of the Anderson model make predictions about the dependence of T_K on various parameters. Close to the middle of a CB diamond ($\epsilon = 0$), N , and thus the charge, is well defined and we expect the Kondo temperature to behave as

$$T_K = \sqrt{U_C \Gamma / 2} e^{-\frac{\pi}{8U_C \Gamma} |4\epsilon^2 - U_C^2|}, \quad (1.3)$$

where $\epsilon = \pm U_C / 2$ corresponds to a resonant situation[20]. The half width at half maximum of the Kondo resonance with respect to V_{SD} is directly related to the Kondo temperature (HWHM $\sim k_B T_K$), and reflects the evolution of $T_K(\epsilon)$, i.e. the width increases as the level is tuned away from $\epsilon = 0$. However, we have to be aware that this analysis is only valid for $\epsilon \ll U_C$. As we approach the resonant condition, N is not well defined anymore. We then enter the mixed-valence regime, which is beyond the scope of this thesis.

A fully developed Kondo state turns the QD completely transparent. For $T \ll T_K$, the maximum differential conductance G_0 of the Kondo resonance depends only on the asymmetry of the coupling to the leads, as described by the Breit-Wigner formula

$$G_0 = \frac{2e^2}{h} \frac{4\Gamma_S \Gamma_D}{(\Gamma_S + \Gamma_D)^2}, \quad (1.4)$$

where a symmetric coupling $\Gamma_S = \Gamma_D$ yields $G_0 = 2e^2/h$ [21]. An increase in temperature will decrease G , until the Kondo resonance is suppressed around T_K . The temperature dependence of G/G_0 follows the empirical form

$$G(T) = G_0 [1 + (2^{1/s} - 1)(T/T_K)^2]^{-s} \quad (1.5)$$

with $s = 0.22$ for spin $s = 1/2$ [17].

1.4 The BCS theory of superconductivity

We have so far been looking at electrical transport through a QD with normal leads, as depicted in Fig. 1.3. Let us now turn our attention towards a QD coupled to two superconducting leads. The electrical transport in the leads is then described by the theory of Bardeen, Cooper, and Schrieffer (BCS)[22]. After a quick introduction to the BCS theory, we will review a number of consequences resulting from superconducting leads, especially with regard to electrical transport. Striving for a simple picture of superconductivity, we restrain ourselves to the theory we need to interpret the results in this thesis[23; 24; 25].

The hallmark feature of superconductivity is that the electrical resistance R in certain metals drops to zero below a characteristic ‘critical temperature’ T_C . This appears to be in contradiction to a picture that relates electrical resistance to scattering of electrons at phonons, i.e. vibrational excitations of the metal lattice. In such a picture, R drops with T because phonons are suppressed, and for $T = 0$, it is expected that the lattice offers no resistance to free conduction electrons at all. However, R remains finite due to scattering at lattice defects like impurity atoms, which is largely independent of T . Naturally, this model can account neither for a vanishing resistance as observed below T_C in superconducting materials, nor for the fact that the transition at T_C is very sharp. How can we understand such an astounding observation?

The BCS theory provides a microscopic model to explain superconductivity. Just like the Kondo effect, superconductivity requires the formation of a new many-body ground state. At the base of this BCS ground state lies an attractive interaction between electron pairs in a sea of conduction electrons. On the one hand, the CB interaction is responsible for a repulsive force between any two electrons, even though it will be partly shielded by other charges around them. On the other hand, free electrons create local distortions in the atomic lattice of the metal, which in turn can act attractively upon other electrons. If this indirect attraction overcomes the Coulomb repulsion, two electrons can couple to form a so-called Cooper pair (Fig. 1.7a). In s-wave superconductors, a Cooper pair consists of two electrons with opposite spin and thus possesses a total spin $s = 0$. Thanks to the integer spin, Cooper pairs do not have to obey Fermion statistics, and can occupy a many-body ground state. This is the BCS ground state Ψ , which describes the sum of all Cooper pairs in the material. Within Ψ , all Cooper pairs have the same momentum k^* , so their individual momenta k relative to Ψ are zero². Furthermore, there is a strong spatial overlap be-

²Often, Cooper pairs are described as having zero spin and momentum. This descrip-

tween Cooper pairs, because the typical length scale of a Cooper pair wave function, ξ_0 , exceeds the average distance among superconducting electrons by far. We call ξ_0 the ‘BCS coherence length’, and use it as a fundamental parameter to characterize a superconductor.

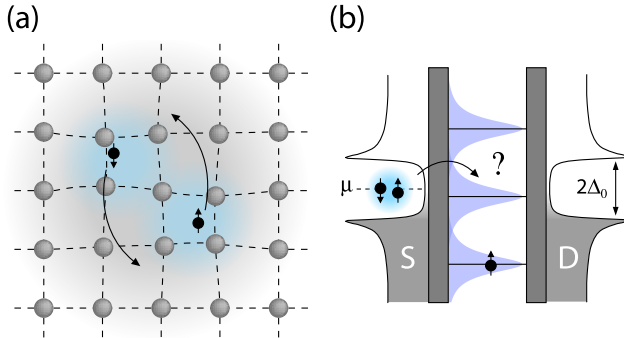


Figure 1.7: **a** Two electrons with opposite spin can couple via the atomic lattice to form a Cooper pair. This allows them to condense into the BCS ground state. **b** A gap forms in the DOS of the leads. No unpaired electrons (‘quasi-particles’) are allowed in this energy window. If Cooper pairs can tunnel through the QD, a Josephson current will ensue.

How does the formation of a collective ground state explain the vanishing resistance in a superconductor? As mentioned above, the most general cause for electrical resistance is scattering of electrons, i.e. changes in momentum of individual electrons. In Ψ , all Cooper pairs must have the same momentum, so scattering of a single Cooper pair requires a momentum change for all other Cooper pairs accordingly. Since this would be associated with a very high cost in energy, scattering of Cooper pairs is completely suppressed, and a dissipation-free current flows through the metal. Still, this current cannot become infinite, but is limited by the density of Cooper pairs. In order to understand what the Cooper pair density depends on, we must first introduce the ‘BCS gap parameter’ Δ_0 .

For $T = 0$, a certain fraction of electrons condenses into Cooper pairs at the chemical potential μ . The exact fraction depends on material properties. It is clear, for instance, that a change of mass of the lattice atoms will change the phonon interaction among them, and thus the attractive force

tion neglects the collective momentum k^* , which is necessary to explain a measured supercurrent.

between electrons that gives rise to the formation of Cooper pairs. This effect was verified with superconductors containing different isotopes of a given material, and provided an early hint that phonon interaction might be responsible for superconductivity. Electrons form Cooper pairs because this represents an energetically lower state. The energy difference per electron is written as Δ_0 , and the energy required to break up a Cooper pair amounts to $2\Delta_0$. We call Δ_0 the BCS gap parameter because it shows up as a gap in the density of states (DOS) of unpaired electrons, $N_S(E)$. Some caution is necessary at this point, because the excitations for unpaired electrons, i.e. their energy spectra in the superconductor, are not identical to those of electrons in a normal metal. To mark the difference, we will refer to unpaired electrons in a superconductor as ‘quasi-particles’. Qualitatively, though, the picture remains the same, because quasi-particles and electrons stand in a one-to-one correspondence. Like in a normal metal DOS $N(0)$, all states far below μ are filled with electron-like quasi-particles, and all states far above μ are empty, i.e. filled with hole-like quasi-particles³. The main modification for quasi-particles is found in the vicinity of μ , where a gap of width $2\Delta_0$ opens up in $N_S(E)$. Inside the gap (for energies $|E - \mu| \leq \Delta_0$), no quasi-particles are allowed, and the corresponding states are shifted to the edge of the gap. The resulting DOS has the form

$$\frac{N_S(E)}{N(0)} = \begin{cases} \frac{|E-\mu|}{\sqrt{(E-\mu)^2 - \Delta_0^2}} & \text{for } |E - \mu| > \Delta_0 \\ 0 & \text{for } |E - \mu| < \Delta_0 \end{cases} \quad (1.6)$$

and is depicted in Fig. 1.7b. Again, grey and white areas represent electron-like and hole-like states, respectively. The peaks at $E - \mu = \pm\Delta_0$ are not infinitely sharp as expected from Eq. 1.6, but slightly broadened in anticipation of ‘realistic’ experimental data.

The BCS theory can relate the density of Cooper pairs, N_{CP} , to the gap parameter as $N_{CP} \propto \Delta_0^2$. At elevated temperatures $T > 0$, some of the Cooper pairs are broken up by thermal excitations, and the gap is reduced correspondingly. We replace therefore Δ_0 by $\Delta = \Delta(T)$. An approximate solution[26] for $\Delta(T)$ yields

$$\Delta(T) = \Delta_0 \tanh(1.74\sqrt{T_C/T - 1}) \quad (1.7)$$

where T_C appears as the temperature at which $\Delta(T)$ vanishes completely, so $\Delta(T_c) = 0$. Microscopically, this means that thermal excitations in the atomic lattice become too strong for any Cooper pair to survive, and the metal reverts to the normal state. For conventional superconductors, T_C

³In the normal state, we referred to filled and empty electron states. In the superconducting state, we call them electron-like and hole-like quasi-particles.

has a universal relation to Δ_0 , and we find $\Delta_0 = 1.76k_B T_C$.

Having gained a qualitative understanding of the microscopic process that gives rise to a dissipation-free current below a critical temperature T_C , we should also devote some attention to the effect of a magnetic field. Luckily, We will merely need to understand why a magnetic field can suppress superconductivity. We can therefore skip most of this wide topic, and then finally return to charge transport through a QD.

One of the most notable features of superconductivity is that a small magnetic field B is completely expelled from the inside of a superconductor (Meissner effect[27]). Whenever B penetrates the superconducting metal, a charge flow is generated to counter the field. In the case of Cooper pairs, this charge flow creates no dissipation, and the Cooper pairs are accelerated until the magnetic field they generate is exactly opposite to B . However, this charge flow comes with a cost in energy, and at some point this energy equals the binding energy 2Δ , so Cooper pairs are broken up into quasi-particles. Depending on their size, bulk Al contacts are driven into the normal state by a magnetic field of 0.1-0.4 T. This is very useful for studying a system in the normal state without changing the temperature.

Now that we are aware of the major features of superconductivity, we can go back to electrical transport through a QD. Looking at Fig. 1.7b, we can guess some of the implications we should expect. On the one hand, it is not obvious whether Cooper pairs can tunnel through single electrical states on the QD at all. If so, this will induce a Josephson current, which is a supercurrent through a small non-superconducting material. On the other hand, quasi-particles from S cannot resonantly tunnel to empty states in D as for normal leads, because electron-like and hole-like quasi-particle states are separated by a gap. However, we will see how so-called Andreev-reflections allow quasi-particle tunnelling.

1.5 Andreev transport

The upper left part of Fig. 1.8 illustrates a QD coupled to two superconducting leads with $V_{SD} = 0$ and $2\Delta \ll U_C$. We look at an off-resonant situation, where tunnelling occurs through the Γ -broadened tails of neighbouring levels (blue shape). With normal leads, these tails give rise to a finite G even in the middle of a CB diamond. This is no longer possible for superconducting leads, because the gap in $N_S(E)$ separates electron-like and hole-like quasi-particle states, so in order to tunnel from S to D, an electron-like quasi-particle must be excited above the gap. A superconducting DOS in the leads causes thus a suppression of background quasi-particle tunnelling at $V_{SD} = 0$ (situation **1** in center part of Fig. 1.8).

Tunnelling from S to D becomes possible for $V_{SD} = -2\Delta/e$ (Fig. 1.8 lower left). Electron-like states in S are now energetically aligned with hole-like states in D, and charge transport is enabled. The onset of quasi-particle tunnelling is marked by a peak in G (situation **2**). Far from a resonant condition, this process is independent of V_{BG} , and we observe ridges inside the diamond at constant bias voltage, $V_{SD} = \pm 2\Delta/e$. Close to resonance, this is not true anymore, and the peaks converge towards $V_{SD} = 0$. The exact behaviour is rather complex and will not be further discussed in this thesis [28; 29; 30].

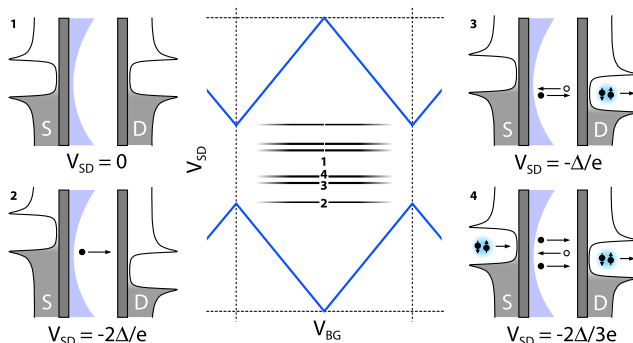


Figure 1.8: Direct quasiparticle tunnelling is not possible for $|V_{SD}| < 2\Delta/e$ (left side). However, Andreev reflections can give rise to charge transport through high order processes (right side). These processes show up as modifications in a measurement of G versus V_{BG} and V_{SD} (center). Note that the CB diamonds themselves are shifted in bias voltage. They close not at $V_{SD} = 0$ on resonance, but at $V_{SD} = \pm 2\Delta/e$, reflecting the changed DOS in the leads.

We have seen that direct quasi-particle tunnelling is only possible above $|V_{SD}| = 2\Delta/e$, so we expect a gap of width $4\Delta/e$ where $G = 0$. However, we find that higher order processes generate subgap features. The upper right of Fig. 1.8 displays a so-called Andreev reflection[31; 32]. An electron-like quasi-particle enters the QD from S and is reflected as a hole-like quasi-particle at the right tunnel barrier. Charge and energy are conserved by the appearance of a Cooper pair in D, so a net charge of $2e$ is transported from S to D. The reversed process can take place with a Cooper pair coming in from S (not shown). The charge transport is the same for both Andreev reflections, and a peak in G is observed at $V_{SD} = \pm\Delta/e$ (situation **3**).

Multiple Andreev reflections (MAR) occur at even smaller bias voltages[33]. For $V_{SD} = 2\Delta/ne$, a process involving n quasi-particles is allowed, as shown

in the lower right part of Fig. 1.8 for $n = 2$ (corresponding to situation 4). However, the probability of higher order processes decreases due to the number of tunnelling events they require. In this thesis, we will not see any MAR for $n > 2$.

1.6 The proximity effect

After analysing quasi-particle tunnelling at finite V_{SD} , we will now focus on Cooper pair transport, i.e. supercurrent through the QD for $V_{SD} = 0$. For this, we follow the Ginzburg-Landau theory[34] and introduce a complex order parameter $\psi(\mathbf{r}) = |\psi(\mathbf{r})|e^{i\phi(\mathbf{r})}$ that allows us to consider spacial variations in the superconductor. Although the BCS theory is a very successful model for conventional bulk superconductors, it cannot easily account for such variations, e.g. a QD. We can reconcile this new parameter $\psi(\mathbf{r})$ with our previous picture of superconductivity by viewing it as a one-particle wave function that describes the position of a Cooper pair. $|\psi(\mathbf{r})|^2$ can be identified with the density of Cooper pairs, N_{CP} . $|\psi(\mathbf{r})|$ is therefore constant as long as no Cooper pairs are created or destroyed, and all changes in the behaviour of the supercurrent are related to the phase ϕ . The length scale over which variations in $\psi(\mathbf{r})$ take place, ξ , turns out to be identical to ξ_0 for pure superconductors well below T_C , but can in general differ from it. This implies that $\psi(\mathbf{r})$ does not vanish abruptly at the boundary of a superconducting material, but decays gradually (Fig. 1.9a). Above T_C , we find $\psi(\mathbf{r}) = 0$, and the normal state is recovered. We do not need to understand the Ginzburg-Landau theory in depth, but it is important to know where the phase ϕ stems from that plays a role in the description of the Josephson effect.

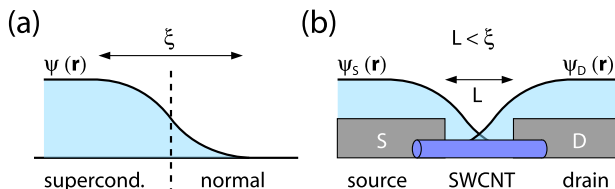


Figure 1.9: **a** The Ginzburg-Landau order parameter $\psi(\mathbf{r})$ decays over a length scale ξ at the interface of a superconductor. A finite Cooper pair density is therefore found in the normal metal close to the boundary (proximity effect). **b** The proximity effect causes transport of Cooper pairs through a non-superconducting junction like a SWCNT if the junction length L is smaller than ξ .

The SWCNT that constitutes our QD is not a superconductor. We can picture it as a normal metal (with quantized electrical levels) between two superconductors separated by a distance L . For $L < \xi$, the two order parameters $\psi_{S,D}(\mathbf{r})$ will not die out completely, and will be coupled over the SWCNT (Fig. 1.9b). In the limit of perfect coupling, the two phases $\phi_{S,D}$ are identical, while a phase difference $\Delta\phi$ occurs for partial coupling. The finite Cooper pair density inside the SWCNT ('proximity effect') gives rise to a supercurrent I_J through the normal metal junction.

1.7 The Josephson junction

The appearance of a supercurrent I_J through a non-superconducting material was theoretically predicted by Josephson[35]. We refer to the device as 'Josephson junction', and to I_J as 'Josephson current'. The material between the superconductors ('weak link') can in general be a normal metal, an insulating barrier, or even a small constriction in the superconductor itself. In our case, the SWCNT acts as a normal metal between two superconducting leads. The fact that the tunnel barriers at the interfaces cause the formation of a QD, such that Cooper pairs need to tunnel through quantized electrical levels from S to D, presents an additional complication that will be treated later on.

The supercurrent through an ideal Josephson junction has a maximum value I_C and depends on $\Delta\phi$ as

$$I_J = I_C \sin(\Delta\phi), \quad (1.8)$$

so $I_J = 0$ if the two superconductors are perfectly coupled and $\Delta\phi = 0$. We call Eq. 1.8 the first Josephson equation. A Josephson current will flow for finite phase differences, with $I_J = I_C$ at $\Delta\phi = \pi/2$. Indeed, the Josephson current provides a measure of the coupling of $\psi_{S,D}(\mathbf{r})$. It is apparent from Eq. 1.8 that in order for I_J to be constant, $\Delta\phi$ needs to be stable as a function of time. However, it turns out that $\Delta\phi$ can change in time as

$$\frac{d(\Delta\phi)}{dt} = \frac{2eV}{\hbar}, \quad (1.9)$$

where V is a voltage drop over the Josephson junction. This constitutes the second Josephson equation. It tells us that an applied voltage will cause the phase difference between the two superconductors to drift, such that the Josephson current oscillates with time. A current measurement will then not extract I_C , but a reduced supercurrent or no supercurrent at all, depending on the junction characteristics.

What value do we expect for I_C ? For a simple tunnel junction geometry,

the Ambegaokar-Baratoff theory relates I_C to the normal state resistance R_N of the junction. At $T \ll T_C$, we get

$$I_C R_N = \frac{\pi \Delta}{2e}, \quad (1.10)$$

where all material properties are included in R_N . For discrete energy levels between two superconductors, we obtain a result from the theory of Beenakker and van Houten[36]. In contrast to the case of a tunnel junction, $I_C R_N$ is not constant anymore, but depends on the level position. The value of I_C is quantized with the number of participating transport channels, M , and goes up to

$$I_C = M \frac{e \Delta}{\hbar} \quad (1.11)$$

for a constriction with $L \ll \xi_0$. Note that M takes the place of R_N in the sense that it relates I_C to the normal state electronic transport. However, by inserting $R_N = \frac{\hbar}{e^2}$ for a transparent SWCNT QD in the CB limit, we do not recover the Ambegaokar-Baratoff limit. The introduction of discrete energy levels has thus consequences for the qualitative description of the Josephson junction. Of course, $L \ll \xi_0$ is not a good approximation for a SWCNT QD. Nevertheless, we can use Eq. 1.11 to estimate an upper limit for the expected supercurrent, and obtain $I_C \sim 25$ nA.

We have so far gained a feeling for the Josephson current as a function of a bias voltage. In the following, we will take a look at the behaviour of Josephson junctions under a finite bias current I . Throughout this thesis, we assume a sinusoidal $I_J(\phi)$ relation as in Eq. 1.8, because it turns out that experimental data fit well to that assumption.

A convenient model for treating Josephson junctions under realistic conditions is the resistively and capacitively shunted junction model (RCSJ)[23]. There, the real Josephson junction is represented by an ideal Josephson junction (carrying a current $I_J(\phi)$) in parallel to a junction capacitance C_J and a junction resistance R_J that accounts for quasi-particle transport. In our case, quasi-particle tunnelling is subject to CB, which means that C_J is of the order of 10^{-15} F or smaller, and $R_J \geq \frac{\hbar}{2e^2}$. However, this is a DC resistance. We will see that frequencies above GHz are relevant for the junction characteristics even for a DC bias current. At such frequencies, the electromagnetic environment provides considerable shunting through the capacitance C between the leads, and this in turn creates a high frequency damping. In the **extended** RCSJ model, a capacitance C between the leads and a total lead resistance R are therefore taken into consideration in addition to I_J , R_J , and C_J (Fig. 1.10a)[37; 38; 39]. The dynamics of $\Delta\phi$ in the

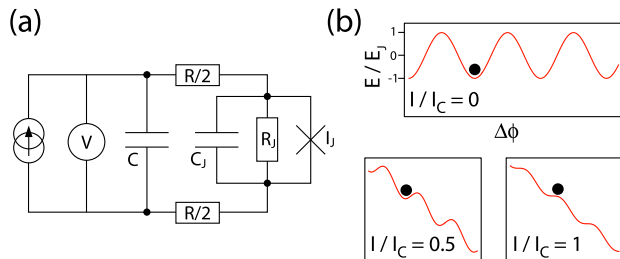


Figure 1.10: **a** The extended RCSJ model takes into account a junction resistance R_J and capacitance C_J as well as the resistance R and capacitance C of the leads. I_J represents an ideal Josephson junction. **b** The dynamics of $\Delta\phi$ under applied current bias I is reminiscent of the motion of a particle in the so-called ‘washboard potential’.

presence of an applied bias current follows from a differential equation that is analogous to the motion of a particle of mass $(\frac{\hbar}{2e})^2(C(1 + \frac{R}{R_J}) + C_J)$ in an effective ‘washboard potential’ of the form

$$U(\Delta\phi) = \frac{\hbar}{2e}(I_C \cos(\Delta\phi) - I\Delta\phi) \quad (1.12)$$

and with damping that is characterized by a quality factor Q . Fig. 1.10b illustrates this intuitive picture. At $I = 0$, the particle (black dot) is trapped in a minimum of the washboard potential with barriers of height $E_J = \frac{\hbar}{2e}I_C$, where E_J is the Josephson coupling energy. Excited by thermal voltage fluctuations, the particle tries to jump over the potential barriers with an attempt frequency that is essentially the plasma frequency

$$\omega_p = \sqrt{\frac{2eI_C}{\hbar(C(1 + \frac{R}{R_J}) + C_J)}} \quad (1.13)$$

for $I < I_C$ ⁴. As long as $k_B T \ll E_J$, these attempts remain unsuccessful, and $\Delta\phi$ is constant. Increasing the current bias I corresponds to tilting the potential landscape, as shown in Fig. 1.10b for $I/I_C = 0.5$. The barriers shift accordingly, and the particle has an increased probability of overcom-

⁴In microscopic Josephson junctions, ω_p becomes large due to the small capacitances involved. The damping provided by C at such high frequencies becomes significant for the overall characteristics of the Josephson junction, and makes it necessary to consider C and R in the first place[40]. For larger junctions, the effect of the electromagnetic environment is usually negligible, and the conventional RCSJ model is a sufficiently precise description.

ing them. At some point, thermal fluctuations will enable it to jump over the barrier, and depending on Q it will get trapped in the next minimum or escape altogether. In the following paragraphs, we will review the two important cases of **underdamped** and **overdamped** Josephson junctions. Finally, when $I \geq I_C$, there exist no stable points in $U(\Delta\phi)$ anymore. The particle slides down the potential drops, so I_J oscillates as described in Eq. 1.8. The measurable supercurrent washes out completely, and effective charge transport occurs exclusively through quasi-particle channels.

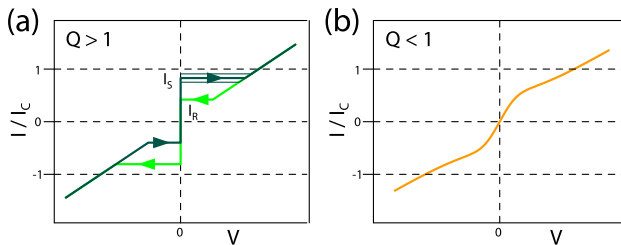


Figure 1.11: **a** Underdamped Josephson junctions displays hysteretic $I-V$ curves. $I_S < I_C$ due to premature switching. **b** In contrast, overdamped Josephson junctions show no sharp switching at all, but a smooth, non-hysteretic transition from a dissipative supercurrent branch to the resistive branch.

One of the most important parameters of a Josephson junction is the quality factor

$$Q = \frac{1}{\omega_p(RC + \frac{\hbar}{2eI_C R_J})} \quad (1.14)$$

that determines the damping of the system for $0 < I < I_C$. In our mechanical picture, the damping is present as friction that dissipates the ‘kinetic energy’ of the particle as it moves along the tilted washboard potential. In an **underdamped** junction, $Q > 1$ and the particle experiences little friction[38]. Once it is lifted over a barrier by thermal fluctuations, there is no mechanism to trap it again. The particle is free to slide down the potential slope (‘running state’), whereupon the measurable supercurrent drops to zero. A plot of the voltage V dropping over the junction in response to I is shown in Fig. 1.11a. Starting from $I = 0$, a positive bias current is applied (dark green). As long as $\Delta\phi$ remains trapped, this current is dissipation-free, and no voltage results. We call this the ‘supercurrent branch’. The position at which the junction passes into a running state is not predictable,

because even for $I < I_C$, the particle has a finite chance of escaping its minimum, and this chance increases exponentially as I approaches I_C . The scattering of the switching current I_S is depicted by several parallel lines. This means that we cannot measure I_C from such an $I - V$ curve, but only a lower limit. In order to extract the true supercurrent I_C , we need to repeat the measurement many times and compare the distribution of I_S to the expected statistical form. Above I_S , the supercurrent is washed out. The applied I is then transported through the junction by dissipative quasiparticle tunnelling as discussed previously (see ‘Andreev transport’), and a finite differential resistance dV/dI arises, which is why we refer to this as the ‘resistive branch’. Upon driving I back to zero, the supercurrent is recovered at the ‘retrapping current’ I_R (bright green). Underdamped Josephson junction are hysteretic, i.e. $I_R < I_S$ in general.

For **overdamped** Josephson junctions, the situation is different[39]. In this case, the motion of the particle in the tilted washboard potential is dominated by large friction that quickly dissipates any surplus kinetic energy. The particle will still try to overcome the potential barriers that confine it, but even if it succeeds, it will be trapped in the next minimum rather than go into a running state. Instead of a sharp switching, we therefore see a smooth transition from a dissipative supercurrent branch to a resistive branch, where the friction is finally overcome by the force driving the particle down the inclined potential (Fig. 1.11b). The $I - V$ curve is completely reproducible because, in fact, it already includes the statistical process that allows $\Delta\phi$ to shift. It is important to understand that the observation of finite dV/dI at $I \ll I_C$ is in agreement with the supercurrent picture. The voltage drop across the junction corresponds to the slow, but steady shifting of $\Delta\phi$ along the potential in the presence of damping. Due to the dissipative supercurrent branch, the extraction of I_C is not straightforward for this case either. However, we can evaluate I_C from a single measurement by fitting the $I - V$ curve to a solution of the extended RCSJ model,

$$I(V) = \left\{ I_c \operatorname{Im} \left[\frac{I_{1-i\eta}(I_c \hbar / 2ek_B T)}{I_{-i\eta}(I_c \hbar / 2ek_B T)} \right] + \frac{V}{R_J} \right\} \frac{R_J}{R_J + R}, \quad (1.15)$$

where $\eta = \hbar V / 2eRk_B T$, and $I_\alpha(x)$ is the modified Bessel function of complex order α [39].

Chapter 2

Fabrication and Measurement Methods

In this chapter, we describe the methods and processes used for sample fabrication and measurements. For detailed information and recipes, please refer to appendix A.

2.1 General device fabrication

All devices that we present in this thesis are fabricated on thermally oxidized Si wafers. The substrate is highly doped to make it conducting, while the SiO_2 serves as a flat, insulating surface for the device (Fig. 2.1a). In order to remove dust particles and organic impurities from the wafer, we perform several cleaning steps before starting with the actual microfabrication.

We grow single-wall carbon nanotubes (SWCNT) on the wafer by the chemical vapour deposition (CVD) method[41]. Wafer pieces are covered with catalyst particles and heated to 950°C in a furnace under a non-reactive atmosphere. The gas is then replaced by CH_4 for 10 minutes. During this time, CH_4 molecules dissociate at the catalyst particles on the wafer surface, and carbon atoms grow into SWCNT. The length and quality of the SWCNT depends in a critical fashion on the growth parameters and on the exact composition of the catalyst[42].

Individual SWCNT are contacted to metallic leads in several steps using electron beam lithography. Fig. 2.1 illustrates this technique: The wafer is spin-coated with a layer of polymethylmethacrylat (PMMA) from a solution in chlorobenzene (Fig. 2.1b). The wafer is baked out to remove the solvent, and then placed in a scanning electron microscope (SEM). Local exposure

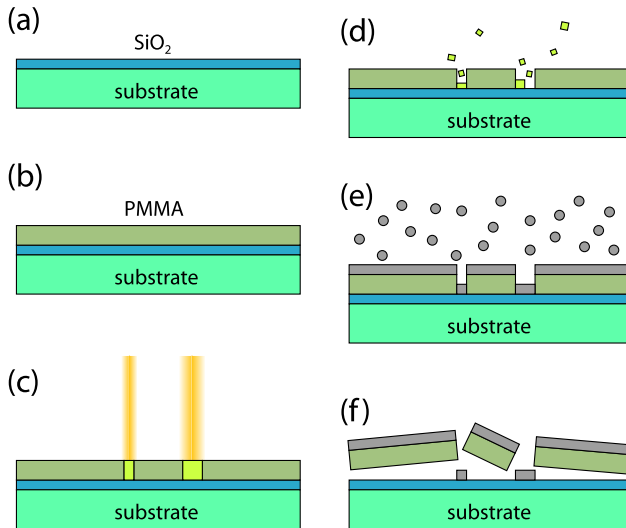


Figure 2.1: Electron beam lithography: **a** Si wafer with SiO_2 on top. **b** Spin coating with PMMA. **c** Patterning with electron beam. **d** Removal of exposed PMMA in a chemical developer. **e** Metal deposition by evaporation. **f** Removal of PMMA mask. A patterned metal film is left on the surface.

of the PMMA to an electron beam (Fig. 2.1c) cuts the polymer chains into smaller pieces that can be dissolved by a chemical developer (Fig. 2.1d). The remaining PMMA is used as a mask during the deposition of metal in the subsequent step: The wafer is placed opposite to a metal source that is heated under vacuum, either by an electron beam or by wires running around the source. The wafer is covered by a film of evaporated metal from the source (Fig. 2.1e) and finally rinsed in Acetone (Fig. 2.1f). In this last step, the PMMA mask is dissolved, and only the metal film in direct contact with the wafer surface is left. In this way, submicrometer-sized structures can be patterned with the electron beam.

The first lithography provides a frame of terminals with bonding pads, and a grid of markers serving as coordinate system in the middle of that frame (Fig. 2.2a). We choose Au as material for this film, both because of its high conductance and because it is easily visible under the SEM, in contrast to e.g. Al. However, to make sure that no SWCNT accidentally creates a short between two terminals, it is useful to underlay the Au layer with SiO_2 , and Ti

for adhesion. Individual SWCNT are selected by SEM, and their position relative to the marker grid is determined. In a second lithography, these SWCNT are contacted to source (S) and drain (D) contacts (Fig. 2.2b). For all devices presented here, we employ Al as bulk superconductor, and a Ti layer to establish good electrical contact to the SWCNT. After the second lithography, the device looks as depicted in Fig. 2.2c, and corresponds to the setup used in chapters 3 and 4.

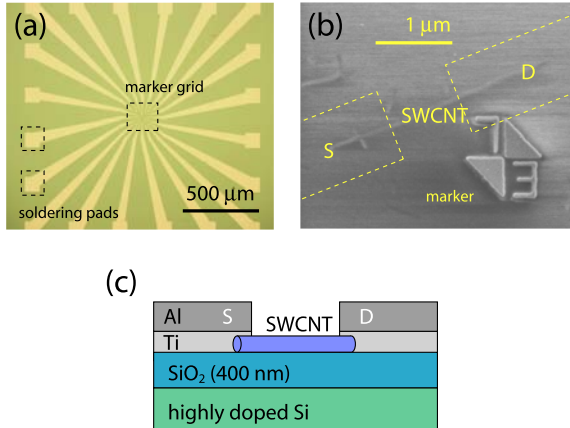


Figure 2.2: **a** In a first lithography, large pads for bonding and a marker grid are deposited (optical microscope image). **b** Individual SWCNT are selected and their position relative to the marker grid is determined. A second lithography contacts them to S and D leads (SEM micrograph). **c** Schematic for a SWCNT with two superconducting leads.

2.2 Topgated carbon nanotube devices

The devices in chapter 6 feature thin metal fingers lying on top of the device as topgates (TG). Naturally, we desire a purely capacitive coupling between the device and the TG. In order to avoid charge transport, we first cover the device with an insulating layer of Al₂O₃ that we grow by atomic layer deposition (ALD). The ALD recipe is calibrated to produce 5 nm of Al₂O₃. Afterwards, we design the TG in a third lithography using Pd, which is non-corroding and cheaper than Au. Fig. 2.3a shows how the Al₂O₃ layer covers the structure isotropically. Since it is transparent in a SEM micrograph,

we can still image the leads and the SWCNT at the end of the fabrication process, as demonstrated in Fig. 2.3b.

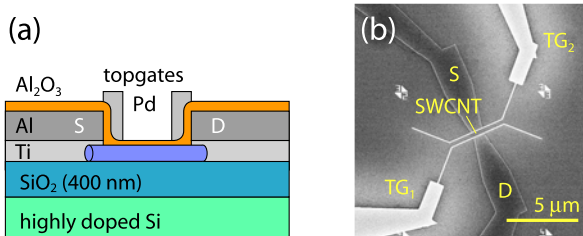


Figure 2.3: **a** Schematic of a SWCNT with two leads and TG. An ALD Al_2O_3 layer is used to prevent charge transport from the TG to the device. **b** SEM micrograph of a finished device.

2.3 Topgated nanowire devices

We follow a different approach in chapter 5, where we discuss a device consisting of a Ge/Si core/shell nanowire (NW) with superconducting S and D leads and TG. In this case, the quantum dot (QD) is not formed between tunnel barriers at the interface of the NW to the leads, because these interfaces are highly transparent. Instead, we make use of the fact that the NW consist of semiconducting material that can easily be depleted by an applied voltage. It has been shown that TG can define tunable tunnel barriers inside Ge/Si core/shell NW by depleting the charge carriers locally[43]. A QD is formed between two such barriers, whose coupling to the leads can be tuned by the TG voltage, V_{TG} . A sketch of such a device is presented in Fig. 2.4a, and a SEM micrograph in Fig. 2.4b. The fabrication process is very similar to that of a SWCNT device, with the exception that the NW are deposited from a solution instead of being grown by the CVD method. Once the Al leads are patterned, the sample should not be exposed to temperature above $\sim 120^\circ$ anymore to avoid unwanted annealing effects between the leads and the Ge core of the NW. This means that subsequent PMMA bakeout steps or ALD processing take place at reduced temperatures.

2.4 Final steps

Once the lithographical fabrication process is over, the sample undergoes a couple of final steps before it can be cooled down. The wafer is cleaved into

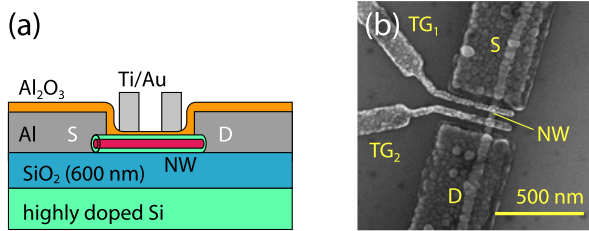


Figure 2.4: **a** Schematic of a NW with two leads and TG. An ALD Al_2O_3 layer is used to prevent charge transport from the TG to the device. **b** SEM micrograph of a finished device.

smaller pieces (max. 5 mm squared) which we glue into chip carriers. Different glues have their advantages and disadvantages: we use two-component epoxy for the sample in chapter 3, and undiluted PMMA for later samples. In contrast to epoxy glue, PMMA is readily dissolved in acetone without heating or sonicating the sample, which allows us to remove the sample from the chip carrier and transfer it to a different measurement environment.

Each chip carrier contains 20 terminals that correspond to measurement lines in the cryostats, and we connect these terminals to the bonding pads on the chip through Al bonding wires. The Si substrate of the wafer is connected to one of the terminals by silver paint (chapter 3) or by removing some PMMA and scratching the SiO_2 layer before the last evaporation step, and bonding on the metal pad that is established thereby (chapters 4-6). The substrate can thus act as a backgate (BG) electrode. Both methods yield reliable connections, but silver paint is prone to creating a mess, and the second solution is to be preferred for its reversibility. Finally, the chip carrier is mounted into the chip socket on the cold finger of the cryostat. The setup used in chapter 4 is not designed for chip carriers. Instead, the sample is glued directly onto the cold finger of the cryostat, and the bonding wires run from the bonding pads to Cu terminals on the cold plate.

These last steps are very delicate because the device is connected to macroscopic metal parts, and any voltage spike that occurs during handling can cause the SWCNT or NW to burn. It is therefore crucial to employ proper grounding for all tools and machines at this stage, especially for bonding and mounting the sample.

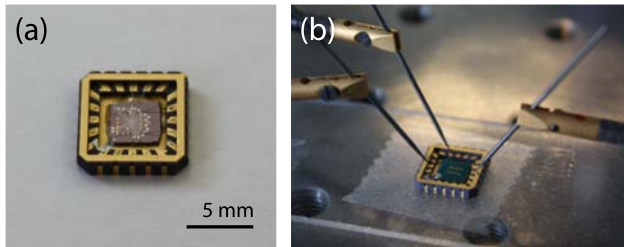


Figure 2.5: **a** Finished sample bonded in a chip carrier. **b** Room temperature measurements of the device conductance are performed in a needle probe setup.

2.5 Room temperature measurements

It is often convenient to take conductance measurements at room temperature, either to monitor changes in individual devices during the fabrication process, or to decide which devices are promising candidates and justify a cooldown procedure. For this, we depend on two different setups.

In a **needle probe station**, the bonding pads on the chip are contacted by metal tips whose position is controlled via micrometer screws. It is not necessary to bond the device, and since the measurement takes place in ambient air, mounting the sample and operating the needle probe station is straightforward. This setup is chosen for checks between fabrication steps, and for selection of suitable devices.

A **testbox** is useful to check a finished sample, including bonding wire connections and chip carrier. Again, the measurement takes place in ambient air and requires little time or effort. If the sample is about to be cooled down, the last test at room temperature is preferably performed in the cryostat itself, with a closed Faraday cage but under ambient pressure. This holds the advantage that the sample does not need to be transferred anymore after the test, because as mentioned before, mounting and dismounting the sample is risky.

In either setup, the wiring is kept simple. The room temperature differential conductance G_{RT} is probed in a voltage biased measurement with a lock-in amplifier (current measurement mode, $V_{AC} = 1$ mV). For the devices we discuss in this thesis, all energy scales are much smaller than thermal excitations at room temperature, $k_B T_{RT} \sim 25$ meV. Due to thermal broadening, the energy levels overlap strongly and it is impossible to resolve single levels spectroscopically. Instead, a measurement of G_{RT} yields a rough estimate

of the maximum conductance through the device, and reveals in the case of a SWCNT whether it is semiconducting or metallic. Metallic SWCNT are expected to display Kondo features and superconducting proximity effect at low temperature if $G_{RT} \leq 100 \text{ k}\Omega$.

2.6 Measurements at low temperature

In order to resolve single energy levels in a QD, one must lower the thermal excitations well below the involved energy scales. On the one hand, this is achieved by phonon cooling, i.e. decreasing the temperature T_{ph} of the atomic lattice excitations in the metal leads of the device. For this, we employ a range of different cryostats. On the other hand, the effective temperature of the conduction electrons, T_{el} , is reduced by filtering high frequency noise in the leads. Since we are performing electrical transport measurements, T_{el} is the relevant parameter. However, below $\sim 1 \text{ K}$, T_{el} and T_{ph} start to decouple, and even though we reach $T_{ph} < 100 \text{ mK}$ in some systems, the effective T_{el} can be higher. Under such circumstances, an efficient filtering setup becomes crucial for good measurements. We will in the following review different types of cryostats before taking a look at electrical filters and other parameters that need to be controlled.

The most basic way of cooling a sample is to dip it into liquid Helium (^4He) with a dipstick. This is simply a hollow metal rod through which the measurement wires are running, with the sample fixed at the lower end. ^4He evaporates at a temperature of $T_{He} = 4.2 \text{ K}$ at 1 bar, which corresponds to an energy of $k_B T_{He} = 360 \mu\text{eV}$. This method is quick, easy, and reliable, but cannot reach temperatures below 4.2 K. No filtering is used in the wiring. T_{ph} can be reduced by placing the dipstick inside a vacuum chamber that is in turn immersed in a ^4He bath, which we refer to as **^4He cryostat**. In this case, the cooling power is provided by continuous evaporation of liquid ^4He . Through a needle valve, small amounts of ^4He are introduced into the inner vacuum chamber (IVC), where they evaporate instantly in the low pressure. The cooling power generated by this evaporation is sufficient to achieve a stable T_{ph} of about 1.7 K.

A different approach is realized in a **^3He cryostat**. ^3He is a rare isotope of He that needs to be produced artificially and is accordingly expensive. The boiling point of ^3He is lower than that of ^4He , and by evaporating ^3He in a cryostat, we reach $T_{ph} \sim 300 \text{ mK}$. However, since it is unaffordable to use a bath of ^3He analogous to a ^4He cryostat, a closed circuit is used where ^3He is evaporated from a liquid phase. Naturally, this implies that the cooling power cannot be provided continuously, because after 24 to 36 hours, all ^3He is bound and needs to be recondensed (single shot operation). An outer ^4He

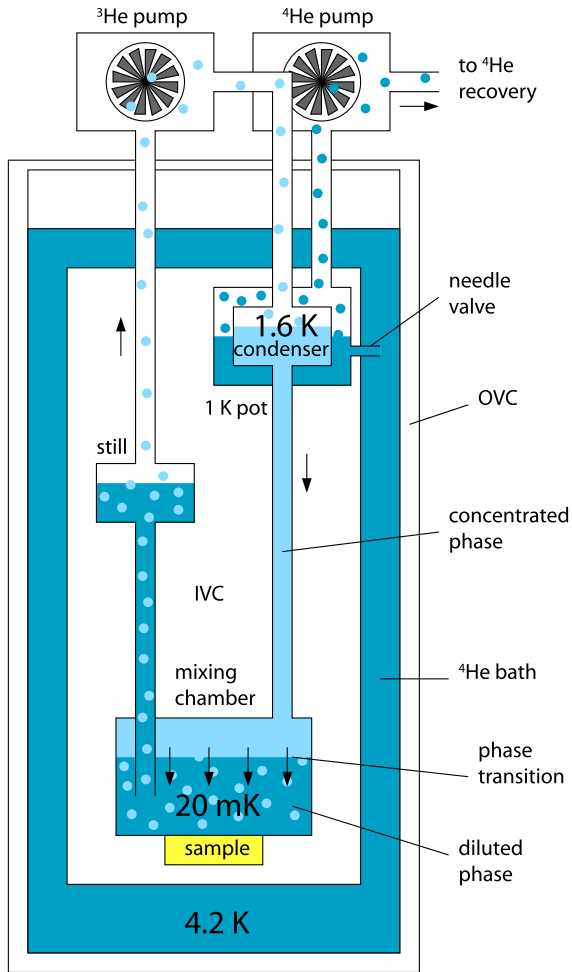


Figure 2.6: Schematic of a $^3\text{He}/^4\text{He}$ dilution refrigerator. ^3He is represented by light blue, ^4He by dark blue.

system is responsible for precooling and liquefying the ^3He . The temperature reached with a ^3He cryostat is adequate to observe superconductivity in Al leads ($T_C = 1\text{ K}$ for Al).

If one wants to access $T_{ph} < 100$ mK, a ${}^3\text{He}/{}^4\text{He}$ dilution refrigerator is a suitable solution (Fig. 2.6). By far the biggest part of the data shown in this thesis was obtained in a dilution refrigerator, with T_{ph} as low as 20 mK. Here, the cooling mechanism depends on a mixture of the two He isotopes which separates into a concentrated ${}^3\text{He}$ rich phase and a diluted ${}^3\text{He}$ poor phase below 0.86 K[44]. Similar to any evaporation from a liquid to a gas, ${}^3\text{He}$ atoms are driven across the boundary between the phases, providing cooling power in the process. This takes place in the ‘mixing chamber’ of the cryostat, which is consequently the coldest part of the setup. To prevent the ${}^3\text{He}$ from accumulating in the dilute phase and saturating, the ${}^3\text{He}$ is pumped away from the mixing chamber and leaves the diluted liquid in the ‘still’ at about 0.7 K. It enters the cryostat again through the ‘condenser’, where it becomes liquid in the concentrated phase. From the condenser, the ${}^3\text{He}$ flows to the mixing chamber and into the diluted phase once more. Again, a separate ${}^4\text{He}$ system is needed for precooling, and especially to liquefy the ${}^3\text{He}$ gas in the condenser. This is done with a ‘1 K pot’ that evaporates ${}^4\text{He}$ through a needle valve in analogy to a ${}^4\text{He}$ cryostat. An outer vacuum chamber (OVC) and a liquid nitrogen bath (not shown) serve to insulate the ${}^4\text{He}$ bath.

What is the fundamental difference between a dilution refrigerator and a ${}^3\text{He}$ cryostat? Essentially, both draw their cooling power from the transition of liquid ${}^3\text{He}$ from a liquid state into a diluted state, either by evaporation or by mixing with ${}^4\text{He}$. However, the equilibrium concentration of ${}^3\text{He}$ in a gas phase tends towards zero as T_{ph} becomes very small, and all ${}^3\text{He}$ condenses in the liquid phase. This means that the cooling power is greatly reduced below a certain temperature, because no evaporation takes place anymore. In contrast, the equilibrium concentration of ${}^3\text{He}$ in the dilute phase of a ${}^3\text{He}/{}^4\text{He}$ mixture is finite even as T_{ph} approaches zero, and we obtain a cooling power well below the base temperature of a ${}^3\text{He}$ cryostat.

All the aforementioned cryostats can be used in combination with a superconducting coil magnet immersed in the ${}^4\text{He}$ bath. By varying the current that runs through a superconducting coil, an adjustable, homogeneous field is created. As long as the coil forms a closed, superconducting loop, the magnet is in the so-called ‘persistent mode’. The current in the loop decays then only very slowly (not at all in an ideal system). In order to change the current, a small part of the coil is heated, whereupon it enters the normal state and breaks the superconducting loop. Our magnet can produce fields of up to 8 T at 4.2 K, although we only use fields of 1 – 2 T.

One important ingredient for low temperature measurements are electrical filters. At $T_{ph} < 1$ K, the electrical temperature T_{el} starts to decouple from T_{ph} . The main obstacle against achieving low T_{el} is high frequency noise in the MHz/GHz regime, which stems from stray fields of electrical instruments

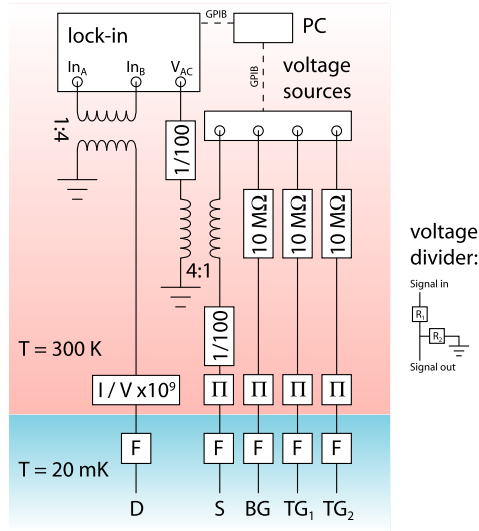


Figure 2.7: Typical setup for voltage biased measurements (see appendix A for description of individual components). We use a SR 830 lock-in amplifier with external I/V-converter, which is either an inhouse construction or a DL instruments 1211. Voltage sources are SR 830 (AUX out) or HP 3245A for V_{SD} , and HP 3245A or YK 7651 for gating. In chapter 4, a SR 560 preamplifier is used to mix AC and DC signals instead of a transformer. ‘ Π ’ refers to Π -filters, and ‘F’ to different filtering systems at low temperature, as discussed in the main text. Blue and red mark parts of the setup that are at low temperature and room temperature, respectively.

at room temperature. In order to prevent this noise from reaching the sample, we need to filter the wires running through the cryostat.

The filtering is usually done in several stages. The working mechanism of all these stages is to dissipate as much high frequency noise as possible while letting the DC signal pass (low-pass filter)¹. At room temperature, this is achieved with LC-filters (also called Π -filters), at low temperatures with different RLC-filters like resistive coaxial wires or microceramic capacitors. As an example, we mention the so-called ‘tapeworm filter’, which consists of twisted pairs of wires packed in a Cu foil[45]. High frequency components of the current are expelled from the core of the wires (skin ef-

¹The lock-in AC modulation is low enough in frequency to be unaffected by the filtering.

fect) and experience a higher resistance R as well as a higher inductance L along the conductor, while the capacitive coupling to the Cu foil acts like a short to ground for them. The efficiency of our filtering was determined by measuring T_{el} via broadening of Coulomb resonances as a function of T_{ph} , in a regime where thermal broadening dominates over Γ -broadening[46]. The lowest T_{el} obtained in these measurements was $T_{el} \sim 50$ mK.

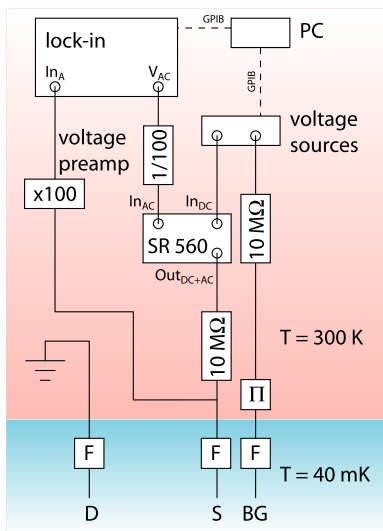


Figure 2.8: Typical setup for current biased measurements (see appendix A for description of individual components). We use a SR 830 lock-in amplifier. Voltage source is a HP 3245A, and a SR 560 preamplifier is used as mixer for AC and DC current. The voltage preamplifier is an inhouse construction. ‘ Π ’ refers to Π -filter, and ‘F’ to different filtering systems at low temperature, as discussed in the main text. Blue and red mark parts of the setup that are at low temperature and room temperature, respectively.

The measurement principle at low temperatures is similar to that at room temperature, but we need to take care of a couple of parameters to optimize the sensitivity of our setup. For instance, since we are at temperatures well below 1 meV^2 , the lock-in AC modulation V_{AC} must be reduced accordingly, such that $eV_{AC} < k_B T$. However, this is a tradeoff, because a smaller modulation causes a smaller signal/noise ratio. We typically apply $V_{AC} = 5$ -

²For $T = 1$ K, $k_B T/e \sim 100 \mu\text{V}$

10 μeV superimposed on a bias voltage V_{SD} and measure the current that flows through the device as a response (Fig. 2.7). An I/V-converter amplifies the current signal and transforms it into a voltage signal that is read out by the lock-in amplifier. The I/V-converter introduces an offset in V_{SD} that needs to be identified and corrected. In all data that we present in the following chapters, this artificial V_{SD} offset is rectified. Fig. 2.8 shows a typical setup for current biased measurements used in chapter 4.

Chapter 3

Even-Odd Andreev Transport due to the Kondo Effect

We now turn towards the experimental results of this thesis by focusing on the interaction between Andreev reflections and Kondo physics in a single-wall carbon nanotube (SWCNT) quantum dot (QD) with superconducting leads. In such a system, we can use the sequential filling of quantized levels, and the accompanying alternation between odd and even occupation of the QD, to switch Kondo correlations on and off. The same is true for superconductivity under the influence of a magnetic field. The high degree of control allows a detailed analysis of the interaction between the two many-particle processes. Please note that the content of this chapter has been published in similar form [47].

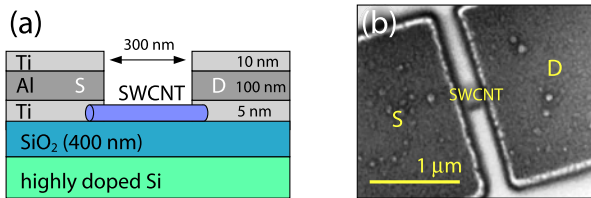


Figure 3.1: **a** Schematic of the device, illustrating the Ti/Al/Ti composition of the leads. The Si substrate serves as a backgate electrode. **b** SEM micrograph of an actual device.

3.1 Introducing remarks

The device used in this experiment corresponds to the illustrations in Fig. 3.1. A metallic SWCNT is contacted to source (S) and drain (D) leads as described in chapter 2. In addition to a Ti adhesion layer and an Al layer, these contacts feature Ti cover layers to prevent oxidation of the Al (Fig. 3.1a). Al is the actual superconductor with a bulk critical temperature of $T_C = 1.2$ K. From transport measurements through the SWCNT, we rather obtain a T_C of 0.9 K, which corresponds to a reduced BCS gap Δ for the proximity induced superconductivity in the Ti layer. The spacing between S and D is approximately 300 nm. The highly doped Si substrate is used as a backgate electrode (BG). A SEM micrograph of an actual device similar to the one measured is shown in Fig. 3.1b.

A QD forms on the SWCNT due to tunnelling barriers at the interfaces to S and D. When the leads are in the normal state, we expect the Kondo effect to take place below a characteristic temperature T_K when the coupling strengths of the QD to the leads, $\Gamma_{S,D}$, are large enough, and when the number of electrons on the QD is odd (Fig. 3.2a). The spins of the electrons in the leads screen the unpaired spin on the QD, producing additional resonances pinned to the chemical potentials of the leads, $\mu_{S,D}$. If superconducting contacts are used instead of normal ones, a competition between the Kondo effect and superconductivity takes place since the two phenomena rely on the formation of opposed spin singlet states. If $\Delta > k_B T_K$, the Kondo correlations are suppressed, whereas they persist in the opposite regime, opening a highly conducting channel for the Josephson effect (Fig. 3.2b) [48]. We report here on finite-bias transport through a SWCNT QD with superconducting contacts in the most interesting regime of intermediate coupling, where Kondo correlations are of similar magnitude as superconducting ones.

All measurements are taken with an AC voltage of $10 \mu\text{V}$ and at a phonon temperature of $T_{ph} \sim 25$ mK where not indicated otherwise. For the normal state data, we use a magnetic field of 0.1 T applied perpendicular to the wafer plane to suppress superconductivity in the leads.

3.2 Results

Fig. 3.3 summarizes the main results we will be discussing in the following. Fig. 3.3a shows a plot of the differential conductance G in the normal state and Fig. 3.3b the corresponding one in the superconducting state. In the normal state a sequence of larger and smaller Coulomb blockade (CB) diamonds are seen (dashed lines), corresponding to a sequence of nearly equally

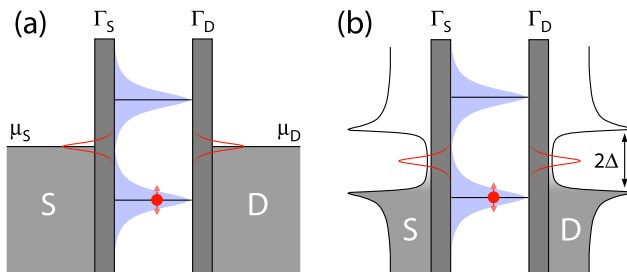


Figure 3.2: **a** QD with two normal leads and an odd number of electrons. The Kondo effect produces additional resonances pinned to μ_S and μ_D . **b** When the leads are superconducting, a competition between Kondo correlations and Cooper pair formation is expected. The Kondo effect prevails if $k_B T_K > \Delta$.

spaced levels on the SWCNT QD, which are filled sequentially. The number of electrons on the dot therefore alternates between odd and even.

It is also seen that G around $V_{SD} = 0$ V is suppressed and featureless in the even valleys, but is increased assuming structure in the odd ones. In the CB diamond labelled **3**, there is a pronounced peak at $V_{SD} = 0$ V, suggesting the appearance of a Kondo resonance. Indeed, the dependence of G on temperature T (Fig. 3.3c), measured in the middle of this valley at $V_{SD} = 0$, follows the expected dependence [17]

$$G(T) = G_0 [1 + (2^{1/s} - 1)(T/T_K)^2]^{-s} \quad (3.1)$$

with a Kondo temperature of $T_K = 0.75$ K. Here, G_0 is the low temperature saturation conductance of the Kondo resonance peak, $G_0 \sim 0.1e^2/h$, and $s = 0.22$. In the other odd valleys, the Kondo resonances are split by $\sim 100 \mu\text{V}$, which is much larger than the Zeeman splitting due to the applied magnetic field of $B = 0.1$ T, amounting to $\sim 20 \mu\text{V}$. The origin of this splitting is at present not known, but could be due to exchange with ferromagnetic catalyst particles or another nanotube [49].

The normal state data can be used to deduce a number of parameters. The source, drain and backgate (BG) capacitances are $C_{S,D} \sim 50, 100$ aF and $C_{BG} \sim 4$ aF, leading to a gate-coupling $\alpha = C_{BG}/C_\Sigma \sim 0.026$, where $C_\Sigma = C_S + C_D + C_{BG}$. The charging energy $U_C = e^2/C_\Sigma$ and the level spacing δE are in the range of 0.7-1 meV and 1.4-1.8 meV, respectively. Whereas this SWCNT QD is nearly symmetric in its electrostatic coupling, it is quite asymmetric in its electronic one. The total level broadening amounts to $\Gamma = \Gamma_S + \Gamma_D \sim 0.2$ meV with an asymmetry of $\Gamma_S/\Gamma_D \sim 50$.

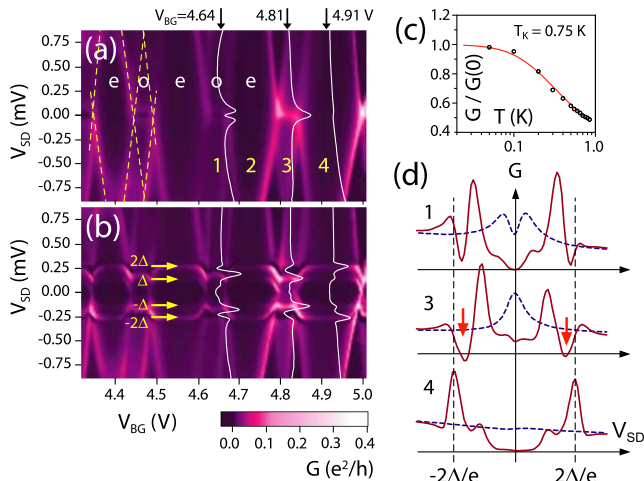


Figure 3.3: **a** Differential conductance G plot as a function of bias voltage V_{SD} and gate voltage V_{BG} in the normal state, at the base temperature of the cryostat ($T_{ph} = 25$ mK). Superconductivity in the leads is suppressed by a magnetic field of 0.1 T. **b** The same measurement with superconducting leads. Additional features due to Andreev tunnelling are visible. **c** Linear conductance G measured as a function of temperature T in the middle of charge state **3**. **d** Detail view of the curves overlaid in **a** and **b** for charge states **1**, **3**, and **4** in the normal (dashed blue) and superconducting (red) state.

This asymmetry is deduced independently from the measured current peaks in G at the border of the CB diamonds at finite bias and from the reduced low temperature zero bias conductance of the Kondo ridge **3**, amounting to $G_0 \sim 0.1 e^2/h$.

Looking next at the superconducting state, we see that the major changes in G are confined to a voltage band of -0.26 meV $< V < 0.26$ meV, corresponding to $\pm 2\Delta$. Above 2Δ , i.e. $|V| > 2\Delta/e$, quasi-particle current is possible and the main modification is caused by the peak in the superconducting density of state (DOS), leading to a peak-like feature in G . Below the 2Δ -gap, first order charge transfer processes are forbidden and charge has to be carried by higher order Andreev processes [28; 29; 30]. The first Andreev process, which is of second order, results in a peak-like structure in the vicinity of $|V| = \Delta/e$. Due to the higher order, this peak and all subsequent ones should be smaller than the quasi-particle peak. The suppressed G in the superconducting state is observed together with the dominant 2Δ

and the smaller Δ -peak in the middle of an even charge state (even valley), see e.g. curve labelled **4** in Fig. 3.3d.

In contrast, in the odd charge states, the 2Δ -feature is not present or does not appear at $|V| = 2\Delta/e$. Starting to view the data from large bias voltage, the first peak appears closer to Δ/e rather than $2\Delta/e$, with a preceding negative G , see curve labelled **3** in Fig. 3.3d. Hence, there is a striking even-odd asymmetry in the finite-bias G features in the superconducting state, which is not caused by the CB resonance at the edges of adjacent charge states, where the situation is expected to be more complex. The even-odd alteration of the MAR structure suggest a relation to Kondo physics. To model this, we first extract important parameters from an analysis of the data in the middle of an even valley where Kondo correlations are absent.

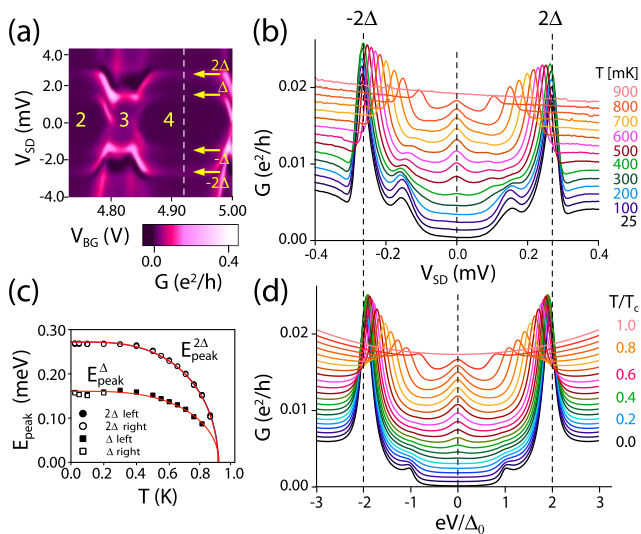


Figure 3.4: **a** Detail plot showing the charge states labelled **2**, **3**, and **4**. The vertical dashed line indicates the position in the even state **4** where the following measurements are taken. **b** Measured G versus temperature V_{SD} for different temperatures. The curves are shifted upwards by $10^{-3} e^2/h$ for clarity. **c** 2Δ and Δ peak positions $E_{peak}(T)$ together with a BCS T -dependence of Δ . **d** Result of a model calculation following [28].

3.3 Even charge state

Fig. 3.4a-d discusses the temperature dependence of G in the middle of the even charge state, at the position of the dashed line in Fig. 3.4a; Fig. 3.4b shows the measurement taken in valley **4**, and Fig. 3.4d is a model calculation. The experiment displays pronounced quasi-particle current peaks at $E_{peak} = \pm 2\Delta$, and weaker MAR peaks at $\pm\Delta$.

The evolution of $E_{peak}^{j\Delta}(T)$ with temperature T is shown in Fig. 3.4c together with an approximate BCS gap function

$$E_{peak}^{j\Delta} = K_{j\Delta}\Delta_0 \tanh(1.74\sqrt{T_C/T-1}) \quad (3.2)$$

where we used the BCS correlation $\Delta_0 = 1.76k_B T_C$. The fit yields $T_C = 0.9$ K, which corresponds to $\Delta_0 = 0.135$ meV, in good agreement with the value of $E_{peak}^{2\Delta}(0)$. Further, we obtain $K_{2\Delta} = 2.0$ and $K_{\Delta} = 1.15$ for the two peaks. The slight increase of K_{Δ} above the expected value of 1 is not accounted for. It might be due to the fact that we measure dI/dV instead of I , which can induce small shifts in the observed voltage values. We will use the value $\Delta_0 = 0.13$ meV as the zero temperature gap parameter in the following. The relevant parameters expressed in units of Δ_0 are: $U_C = 5-8$, $\delta E = 10-14$, $\Gamma \sim 1.5$ and $k_B T_K \sim 0.5$. The zero bias peak in Fig. 3.4b, appearing at intermediate temperatures, can be explained by direct tunnelling of quasi-particles that are thermally activated across the gap.

The good agreement with the BCS relation of the peak positions motivates the modelling of G using the BCS DOS in the leads¹. The model uses Andreev tunnelling through a single resonant level positioned at energy ϵ [28]. The following parameters in units of Δ_0 were used: $\Gamma_S = 1.0$, $\Gamma_D = 0.03$ and $\epsilon = 7$. The BCS DOS was broadened by $0.1 \Delta_0$, accounting for the averaging in the experiment due to the ‘small’ AC bias. A remarkably good agreement is found (Fig. 3.4d).

3.4 Odd charge state

We now turn our attention to the odd charge states. We point out that the zero bias high- G Kondo ridge, which is associated with the Kondo resonance and visible in the normal state, is not seen in the superconducting state (see Fig. 3.3a and b). This is in contrast with previous results which correspond to larger values of T_K compared to Δ [48; 30]. Although the Kondo resonance is not visible at zero bias in the superconducting state, we

¹Model calculations performed by A. Levy-Yeyati, J. C. Cuevas, and A. Martín-Rodero

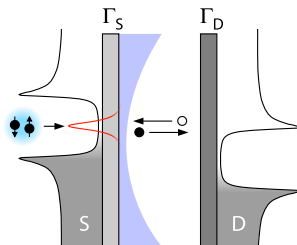


Figure 3.5: This figure illustrates our proposal to understand the appearance of the strong Δ -feature in the odd valleys. A Kondo resonance persists on one electrode side only. Because it is pinned to that chemical potential, it will strongly enhance the Δ -feature in Andreev tunnelling.

suspect it to be responsible for the even-odd asymmetry of the Δ -feature in the superconducting state.

In the Kondo regime, the single spin on the QD in the odd state is screened by exchange with conductance electrons from the leads. If the electrons are bound in Cooper pairs in the leads, the Kondo temperature is renormalized, assuming a smaller value T_K^* [50]. This renormalization is sensitive to the actual parameters $\Gamma_{S,D}$ and Δ . Due to the asymmetry in the coupling, it may happen that a Kondo resonance with a reduced width forms on the contact with the larger coupling, whereas on the other contact the Kondo resonance is suppressed. This is illustrated in Fig. 3.5 for a bias voltage of $V = -\Delta/e$. Again, this scenario is modelled considering a single-level Anderson Hamiltonian with interaction $U_C = 5-10 \Delta_0$ coupled to S and D contacts². The experimentally deduced $\Gamma_{S,D}$, including the strong asymmetry, were used. To deal with the interaction term, we use a finite U_C slave-boson mean field approach which accounts reasonably well for the low energy spectral density in the Kondo regime [51]. The approach yields renormalized parameters $\tilde{\epsilon}$, $\tilde{\Gamma}_{S,D}$, which depend both on the gate and on the bias voltage. These parameters are obtained in the normal state and introduced into the calculation of the subgap current as in Ref. [28].

The result of the comparison is shown in Fig. 3.6: Fig. 3.6a and Fig. 3.6b correspond to the normal state experiment and model, respectively. We indicate the level position ϵ (instead of V_{BG}) and the bias voltage V_{SD} in units of Δ_0 to facilitate the comparison. Vertical dashed lines mark $\pm U_C/2$. Please note that the experiment corresponds to $U_C = 7-8$, while the

²Model calculations performed by A. Levy-Yeyati, J. C. Cuevas, and A. Martín-Rodero

calculation was done $U_C = 5$ and $U_C = 10$, where the latter is shown here. The Kondo resonance is reproduced with a remarkably good agreement. Fig. 3.6c and Fig. 3.6d correspond to the superconducting state experiment and model, respectively. Here, horizontal dashed lines indicate $V_{SD} = 2\Delta/e$ and $V_{SD} = \Delta/e$. The dominance of the Δ -feature in the odd valley (**3**) is clearly present, as is a similar cross-over from odd to even filling. There are also some differences: in the experiment the Δ -feature bends to larger V_{SD} -values in the middle of the odd state, whereas this feature is rather flat in the calculation.

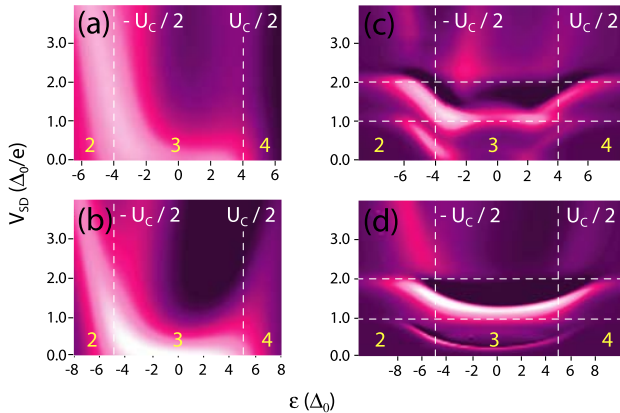


Figure 3.6: Comparison of G in the odd valley labelled **3** with a model calculation based on a single-level Anderson model with finite Coulomb interaction U_C that is evaluated by a mean field slave-boson approach. The experiment corresponds to $U_C = 7-8$, while the calculation is presented for $U_C = 10$. We show in **a** the normal state experiment, in **b** the normal state model, in **c** the superconducting state experiment, and in **d** the superconducting state model.

3.5 Summary

In conclusion, we have discovered a pronounced even-odd effect in the Andreev structure in transport through a QD with superconducting contacts. More precisely, the feature at $V_{SD} = \pm\Delta/e$ is enhanced in charge states with an odd number of electrons on the QD. This effect is related to the competition between superconductivity and the Kondo effect, which takes

place in these charge states when the leads behave as normal metals. In the presence of superconductivity in the leads, the Kondo effect persists if $k_B T_K > \Delta$, but is suppressed in the opposite regime [48]. In our device, the coupling of the QD to the two leads is highly asymmetric, such that $\Gamma_S/\Gamma_D \sim 50$. The Kondo effect is therefore suppressed on the side with low coupling (opaque tunnel barrier), but persists on the other one (transparent tunnel barrier), giving rise to an enhancement of the Δ -feature, but not to the characteristic Kondo ridge around zero bias.

Similar results were obtained independently in InAs nanowires[52]. The explanation put forward in that work relies also on the interplay between Andreev transport and the Kondo effect, but not on the asymmetry between Γ_S and Γ_D , which is smaller than in our device. Future experiments will need to address this discrepancy.

Chapter 4

Tuning the Josephson Current With the Kondo Effect

In chapter 3, we studied how the Kondo effect can interact with Andreev transport through a single-wall carbon nanotube (SWCNT) quantum dot (QD) with superconducting leads at finite bias voltage. In a next step, we can now analyse how Kondo correlations change the behaviour of the Josephson current in such a system, i.e. how coherent tunnelling of Cooper pairs through a QD is affected by the formation of a Kondo singlet state. In order to achieve this, we need to improve the control over high frequency dissipation processes in and around our device. We do so by deliberately introducing additional resistors in the on-chip environment. Part of this work was published in [53].

4.1 Introducing remarks

Fig. 4.1a shows a schematic of the device used in this experiment. A metallic SWCNT is contacted to source (S) and drain (D) leads as described in chapter 2. Al is a superconductor with a bulk critical temperature of $T_C = 1.2$ K. The spacing between S and D is approximately 550 nm, and the highly doped Si substrate is used as a backgate electrode (BG). The main modification of this sample relative to the one presented in the previous chapter consists of additional on-chip resistors in the Au lines leading to the superconducting Al contacts. In Fig. 4.1b, the on-chip resistors and Al leads are highlighted in orange and blue, respectively. In the framework of

the extended resistively and capacitively shunted junction (RCSJ) model, these resistors correspond to the parameter R (Fig. 4.1c) that influences the characteristics of a Josephson junction at finite current bias. We define $R \sim 2 \text{ k}\Omega$ in order to create an overdamped Josephson junction, as discussed in chapter 1.

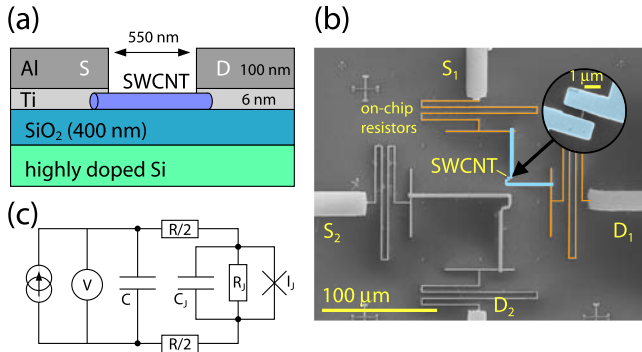


Figure 4.1: **a** Cross section of the nanotube with electrodes and backgate **b** Scanning electron micrograph of the electrical on-chip environment of the nanotube. **c** Schematic of the SWCNT Josephson junction with its environment according to the extended RCSJ model.

Proximity induced superconductivity through carbon nanotube QD was first explored in suspended devices with no backgate electrode (BG) [5]. More recently, tunable supercurrents could be detected in the resonant tunnelling conduction regime, where the transmission of the contacts approaches unity [38]. In this regime, the discrete spectrum of the nanotube is still preserved and the maximum value of the supercurrent is observed when the QD is on resonance. A superconducting quantum interference device (SQUID) was fabricated with carbon nanotubes as weak links: supercurrent π phase shifts occurred when the number of electrons in the nanotube dot was changed from odd to even [54], corresponding to the transition from a magnetic to a nonmagnetic state. Sharp discontinuities in the critical current at this $0-\pi$ transition in relation with the even-odd occupation number of the nanotube quantum dot were also observed in SWCNT junction devices [39]. As pointed out in the SQUID experiment [54], a Josephson current can be observed in the Kondo regime when the Kondo temperature T_K is large compared to the superconducting gap Δ , confirming previous experiments where supercurrents were not directly determined [48; 55].

Our device is in an intermediate coupling regime where T_K is comparable to Δ . We explore in detail the competition between Josephson and Kondo physics by monitoring on the same device the bias dependence of the differential conductance in the normal state and the Josephson current in the superconducting state as a function of the gate voltage.

4.2 Setup details and junction parameters

Measurements are done in a dilution refrigerator with a base temperature of $T_{ph} \sim 40$ mK. The cryostat is equipped with a three stage filtering system consisting of LC filters at room temperature, resistive micro-coax wires and finally micro-ceramic capacitors in a shielded metallic box, which also contains the samples and is tightly screwed onto the cold finger. The on-chip resistors implemented lithographically in the Au lines of the sample serve as additional filters against voltage fluctuations (Fig. 4.1b). We use a lock-in technique with either an AC voltage of 5 or 10 μ V, measuring differential conductance $G = dI/dV$, or an AC current of 10 pA, measuring differential resistance dV/dI , both as a function of an additional DC bias voltage (V_{SD}) or current (I), respectively. From simple electrostatic considerations, we can calculate values for the parameters shown in Fig. 4.1c. We obtain a rough estimate of $C_J \sim 100$ aF from the charging energy $U_C = e^2/2C_J$. The junction resistance R_J represents the contribution of quasi-particles to dissipation at frequencies of the order of the plasma frequency of the junction, ω_P . C represents the capacitance between the leads. It is mainly determined by the capacitance of the metallic leads to the highly doped BG within the electromagnetic horizon of the junction¹, and can be estimated to $C \sim 8$ pF. Due to this large value of C , it is possible that the finite resistivity of the BG contributes to dissipation at very high frequency. Since we cannot neglect the effects of this high frequency dissipation, we need to take C and R into consideration and work with the extended RCSJ model, as explained in chapter 1.

4.3 Results

We first characterize the SWCNT QD with the electrodes driven normal by a small magnetic field ($B = 0.1$ T). The charge stability diagram (plot of G as a function of V_{SD} and V_{BG}) displays a regular sequence of Coulomb blockade (CB) diamonds over a wide range of V_{BG} . For further analysis, we concentrate on the gate voltage region between 3 and 4 V (Fig. 4.2a). It

¹We estimate the horizon as $2\pi c/\omega_p$ to some centimeters, depending on R_J .

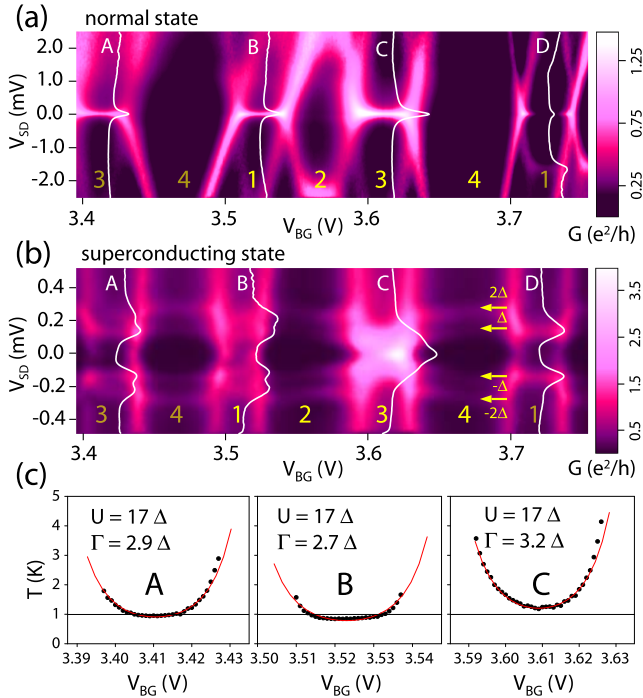


Figure 4.2: Colour scale plot showing V_{BG} and V_{SD} dependence of G ; **a** normal state, **b** superconducting state. White lines correspond to vertical sections of G versus V_{SD} in the middle of the four Kondo ridges labelled A to D. **c** V_{BG} dependence of the Kondo temperature T_K extracted on the Kondo ridges far from the degeneracy points. Red lines are fits to Eq. 4.1, the black line corresponds to $T_C = 1.0$ K. U_C and Γ are given in units of Δ .

shows a fourfold periodicity in the size of the CB diamonds [8], which indicates a clean nanotube with the twofold orbital degeneracy of the electronic states preserved. We extract $U_C = 2.5 \pm 0.3$ meV as estimated from the size of Coulomb blockade diamonds with an odd number of electrons. In all states with odd occupation, the Kondo effect manifests itself through a high conductance region around zero bias, the so called ‘Kondo ridge’. The Kondo temperature T_K can be estimated from the half width at half maximum (HWHM) of the peaks of these lines, which can be fitted by Lorentzian curves [17]. T_K goes through a minimum of the order of 1 K in the center

of the ridges and increases on the edges. It is possible to follow this gate dependence along the Kondo ridges A to C (Fig. 4.2c). The intensity on ridge D is too weak for such an analysis. T_K can be well fitted by the expression predicted by the Bethe Ansatz

$$T_K = \sqrt{U_C \Gamma / 2} e^{-\frac{\pi}{8U_C \Gamma} |4\epsilon^2 - U_C^2|}, \quad (4.1)$$

where ϵ is the energy shift measured from the particle-hole degeneracy point where $\epsilon = 0$ [20]. Taking $U_C = 2.5$ meV as determined above, the value of T_K at $\epsilon = 0$ leads to the characteristic coupling energies $\Gamma = \Gamma_S + \Gamma_D$ between the electrodes for each Kondo ridge (Fig. 4.2c). The V_{BG} dependence of T_K yields the ratio α between the electrostatic energy eV_{BG} and the Fermi energy of the nanotube ϵ equal to 20 ± 1 . This value agrees to within 20% with the value deduced from the normal state conductance data. This fit is based on the single level Anderson impurity model and is only valid when U_C/Γ is sufficiently large and $|\epsilon| \ll U_C$, since close to the Coulomb resonances, the charge number on the QD is not well defined anymore. For all Kondo ridges, $T \ll T_K$, so the maximum conductance of the ridges yields the asymmetry of the coupling Γ_S/Γ_D as described by the Breit-Wigner formula

$$G_0 = \frac{2e^2}{h} \frac{4\Gamma_S \Gamma_D}{(\Gamma_S + \Gamma_D)^2}, \quad (4.2)$$

and we obtain asymmetries of 6.8, 6.2, 2.5, and 70 for A, B, C, and D, respectively.

By switching off the magnetic field, we allow the leads to become superconducting. Fig. 4.2b shows G for the same gate voltage range as in Fig. 4.2a, but for a smaller V_{SD} range. The BCS-like density of states (DOS) in the electrodes leads to new features in the stability diagram, namely horizontal lines at $V_{SD} = \pm 2\Delta/e$ and $V_{SD} = \pm \Delta/e$ due to the onset of quasi-particle tunnelling and Andreev reflection, respectively. We can derive the value of the superconducting gap $\Delta = 0.15 \pm 0.02$ meV, which corresponds well to the expected $T_C \sim 1$ K for the bilayer Ti/Al.

Although they have similar T_K in the normal state, the Kondo ridges A, B, C, and D show a very different behaviour when the electrodes are superconducting: the Kondo ridges A, B, and D are suppressed or reduced in amplitude by superconductivity, reflecting that $T_K < T_C$ in the center of the Kondo ridge. Contrary to ridge A, B, and D, that show a minimum at zero bias, there is a strong enhancement of conductance in ridge C, with G reaching a value roughly four times larger than in the normal state. Note that the states A, C, and D show an enhancement of conductance at $V_{SD} = \Delta/e$ to values larger than the conductance at $V_{SD} = 2\Delta/e$. This

effect, which is described in detail in the previous chapter, is attributed to a situation where the Kondo resonance survives only on one side of the QD in the presence of superconductivity due to asymmetrical coupling [47]. As a consequence, no Kondo ridge is observed around $V_{SD} = 0$ V, but G is enhanced for $V_{SD} = \pm\Delta/e$. An alternative explanation was brought forward in [52] that does not involve a coupling asymmetry. However, we suggest that the data in Fig. 4.2 supports our model. The Kondo ridges in Fig. 4.2a show asymmetries of 70 (D), 6.8 (A), 6.2 (B), and 2.5 (C), in descending order. Looking next at the white lines in Fig. 4.2b that represent cuts of G versus V_{SD} through the middle of the Kondo states, we realize that the enhancement of the Δ -feature is most pronounced in state D, where the asymmetry is largest. In A, the Δ -feature is only slightly elevated above the 2Δ -feature, corresponding to a more symmetrical coupling. The coupling becomes even more symmetrical in state B, where the 2Δ -feature is dominant over the Δ -feature. State C represents an exception, because there the Kondo correlations survive fully in the superconducting state, as we can see from the peak at $V_{SD} = 0$ V as well as from the accordingly high T_K in Fig. 4.2c. In that case, the Kondo resonance persists on both sides of the QD, and we observe both a zero bias ridge and an enhancement of the Δ -feature, regardless of the rather symmetrical coupling [50; 56].

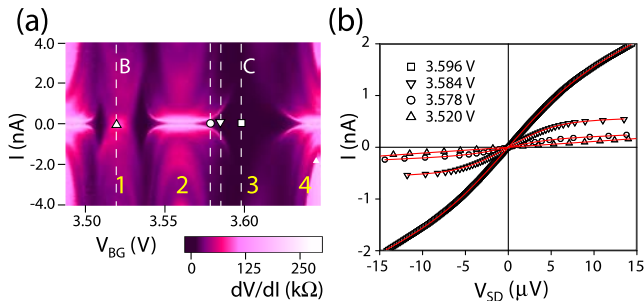


Figure 4.3: **a** Colour scale plot of the differential resistance dV/dI as a function of V_{BG} and DC bias current I . **b** I - V characteristics for different values of V_{BG} . Red lines are fits using Eq. 4.3.

For a measurement of the supercurrent, the device has to be current biased. We simultaneously use AC and DC bias while measuring the resulting voltage drop. From the AC part, we obtain data on the differential resistance dV/dI (Fig. 4.3a). By numerical integration, we get I - V curves that show a supercurrent branch and a smooth transition to a resistive branch

with higher resistance (Fig. 4.3b). The transition between the two regimes is not hysteretic, and the supercurrent part exhibits a nonzero resistance R_S at low bias even if we subtract the contribution of the on-chip resistances R . This behaviour is characteristic of overdamped Josephson junctions, as pointed out in chapter 1, and is a consequence of the electromagnetic environment that is illustrated in Fig. 4.2 c. To extract the supercurrent, we use a theory that explicitly includes the effect of the electromagnetic environment onto the junction in the frame of the extended RCSJ-model [38; 39]. Using the external resistor R as input parameter, we can thus extract the critical current I_c (defined as the maximum value of $|I_J(\phi)|$ over ϕ) and the junction resistance R_J , for every measured BG voltage, from a fit to

$$I(V) = \left\{ I_c \operatorname{Im} \left[\frac{I_{1-i\eta}(I_c \hbar / 2ek_B T)}{I_{-i\eta}(I_c \hbar / 2ek_B T)} \right] + \frac{V}{R_J} \right\} \frac{R_J}{R_J + R}, \quad (4.3)$$

where $\eta = \hbar V_{SD} / 2eRk_B T$, and $I_\alpha(x)$ is the modified Bessel function of complex order α [39]. This solution assumes a sinusoidal current-phase relation $I_J = \sin(\Delta\phi)$, where $\Delta\phi$ is the difference in the Ginzburg-Landau phase between S and D². The resulting values are plotted as a function of V_{BG} in Fig. 4.4a and b. The junction conductance $G_J = 1/R_J$ relates well to the differential conductance $G_S = 1/R_S$ extracted from the AC part of the current biased data, especially around the resonance degeneracy points where the conductance is high. The normal state conductance G_N deviates from G_S most notably in the states B and C, where Kondo physics plays a key role. In state B, $G_N > G_S$ whereas the ridge in state C persists in the superconducting state, resulting in a further enhancement of the conductance.

I_C exhibits peaks at the maximum values of the conductance (Fig. 4.4b). Its behaviour between peaks varies strongly in states with even and odd occupation. In the following we focus on the Kondo ridges B and C. Whereas the supercurrent on ridge C varies nearly proportionally to the conductance, we observe a sharp drop of supercurrent on ridge B as indicated by grey arrows in Fig. 4.4b. This is related to the fact that $T_K > T_C$ on ridge C, such that the Kondo effect persists and the excess electron on the QD remains screened in the superconducting state (see Fig. 4.2c). In contrast, $T_K < T_C$ on ridge B near $\epsilon = 0$, which results in a suppression of the Kondo singlet state, and the QD hosts a magnetic doublet state instead. Fig. 4.5 illustrates how the tunnelling of Cooper pairs is affected by this difference: In the case of $T_K > T_C$, Cooper pair transport profits from the high conductance Kondo channel, whereas for $T_K < T_C$ the two electrons of a Cooper pair have to tunnel through the QD sequentially via virtual states.

²The approximation yields excellent results, as we see in Fig. 4.3b, but we need to be aware that in general, $I_J(\Delta\phi)$ can have a much more complex form.

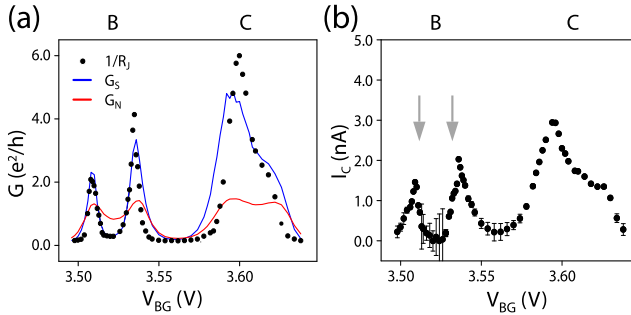


Figure 4.4: **a** Conductances $G_J = 1/R_J$ (black circles), G_S (blue line), and G_N (red line). **a** V_{BG} dependence of the critical current I_C extracted from fits of Eq. 4.3 to the I-V curves in Fig. 4.3b.

This results in a suppression of I_C as well as a change in the phase difference $\Delta\phi$ by π . We therefore term this the ‘ π state’, and refer to the passage from one to the other as ‘ $0-\pi$ transition’. The phase change accompanying such a transition can be traced in experiments with superconducting quantum interference devices (SQUID) [54; 57].

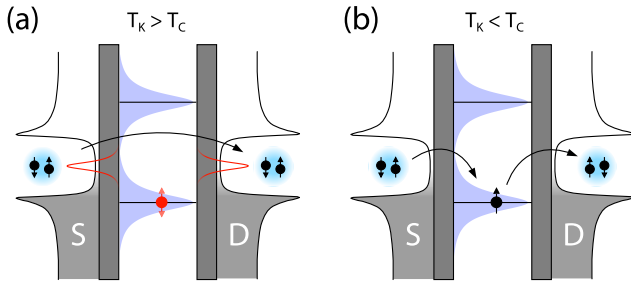


Figure 4.5: Model picture for the $0-\pi$ transition: **a** For $T_K > T_C$, the unpaired spin on the QD is screened by the Kondo effect, and Cooper pair tunnelling from S to D is enhanced. **b** For $T_K < T_C$, the unpaired spin remains unscreened, and the two electrons of a Cooper pair have to tunnel through the QD sequentially via virtual states. This results in a suppression of I_C as well as a change in the phase difference $\Delta\phi$ by π .

At this stage we compare our experimental findings to approximate zero-

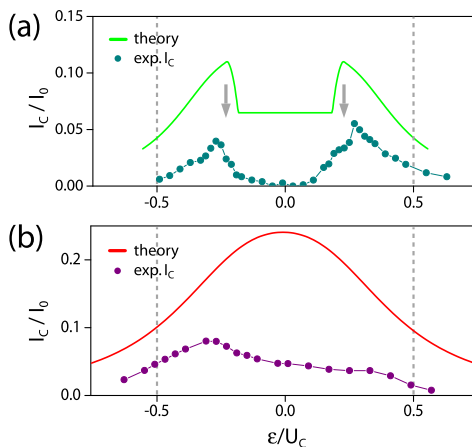


Figure 4.6: Comparison with FRG calculations: Calculated $I_C(\epsilon)$ in units of $I_0 = e\Delta/\hbar$ for $\Gamma = 2\Delta$, $\Gamma/U_C = 0.11$, $\Gamma_R/\Gamma_L = 6$ in **a** and $\Gamma = 2\Delta$, $\Gamma/U = 0.2$, $\Gamma_R/\Gamma_L = 3$ in **b**. Experimental data for $I_C(\epsilon)$ are shown for Kondo ridge B in **a** and Kondo ridge C in **b**.

temperature functional renormalization group (FRG) calculations, which allow for extracting both the stability regions of the screened singlet and magnetic unscreened doublet phases and the complete $I_J(\phi)$ relation within a model of an Anderson impurity coupled to two superconducting electrodes [20]³. It was previously observed that the Josephson current cannot be simply described as a single function of the ratio T_K/Δ [58]. The relevant parameters are the Coulomb energy U_C , the level position ϵ related to V_{BG} , and the transmission of the electrodes Γ_S and Γ_D compared to Δ . In Fig. 4.6 we present a comparison of our experimental data to theoretical calculations for I_C as a function of ϵ , for similar values of theoretical and experimental parameters. It is remarkable that the gate dependence of the critical current on the Kondo ridges can be qualitatively described. In particular, theory predicts the existence of a singlet/doublet ($0-\pi$) transition on ridge B at nearly the right value of V_{BG} when renormalized with the charging energy U_C (grey arrows), and the absence of a $0-\pi$ transition for ridge C, corresponding to higher values of T_K . One point of disagreement between theory and experiment concerns the amplitude of I_C in the π state region (around $V_{BG} = 3.65$ V). I_C is theoretically found to be reduced by only a

³Calculations performed by C. Karrasch and V. Meden.

factor of two compared to its value in the singlet region whereas basically no trace of superconductivity could be detected experimentally. It is known, however, that the π -phase current computed from the approximate FRG is too large compared to numerical renormalization group (NRG) data, which are known to be more accurate at the center of the Kondo ridge, the only region where NRG data can be obtained [20].

Finally, let us emphasize the importance of the asymmetry of the transmission of the electrodes which tends to reduce considerably the supercurrent. This is particularly striking for the data on ridge D, for which $\Gamma_D/\Gamma_S = 70$, where no supercurrent could be measured in spite of a value of T_K of the order of 1 K. This reduction of I_C by the asymmetry of contacts is also found in FRG calculations [20]. It is moreover accompanied by a modification of the stability regions for the singlet (screened) and doublet (magnetic) states which strongly depend on the phase difference $\Delta\phi$ between the superconducting electrodes. The non-magnetic singlet state is stabilized with respect to the magnetic doublet state in the vicinity of $\phi = \pi$, which results in a strong modification of the current-phase relation which unfortunately cannot be checked in a single I_C measurement [20].

4.4 Additional data

In this section, we would like to discuss an alternative method of extracting supercurrent values. We study a zero bias peak in voltage biased measurements and verify that it can be interpreted as a supercurrent. We have the opportunity to compare the current corresponding to this peak to the fitted value of I_C over several charge states.

The normal state data in Fig. 4.7a exhibits resonant tunnelling with $G > e^2/h$ at $V_{BG} = 0.98$ V, which is the signature of Fabry-Perot oscillations that replace the Coulomb diamond pattern for $\Gamma > U_C$ [59]. When the coupling Γ becomes large enough, neighbouring level on the SWCNT start overlapping strongly. Rather than acting as a QD with a well defined charge number, the SWCNT now forms an electron waveguide, and the conductance can reach the theoretical limit of $4e^2/h$. The maximum G on resonance, $1.2 e^2/h$, corresponds to an asymmetry of ~ 12 . In our device, the Fabry-Perot pattern is only observed over a small region. The charge state labelled **3** is clearly in the CB regime again, as is indicated by yellow dashed lines. A rough estimate yields $G_0 \sim 0.75 e^2/h$ and $HWHM \sim 80 \mu\text{eV}$ for the Kondo ridge that is observed there, from which we get a coupling asymmetry $\Gamma_S/\Gamma_D \sim 9.5$ and $T_K \sim 1$ K.

With superconducting leads, the charge stability diagram is modified in the expected way. Horizontal lines at bias voltages of $V_{SD} = \pm 2\Delta/e$ and

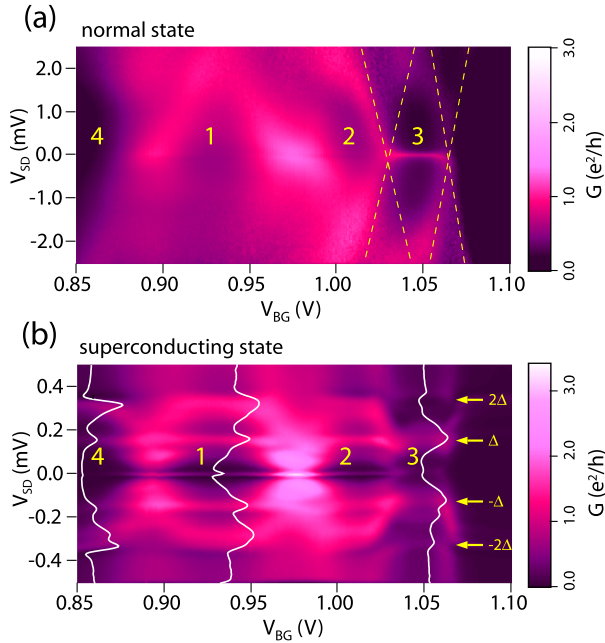


Figure 4.7: **a** G versus V_{BG} and V_{SD} in the normal state. The resonance between the states **1** and **2** exhibits $G > 1 e^2/h$, which indicates that the device is in the Fabry-Perot regime. **b** The same measurement with superconducting leads. White lines represent cuts of G versus V_{SD} through the middle of the states labelled **4**, **1**, and **3**.

$V_{SD} = \pm\Delta/e$ mark the onset of direct quasi-particle tunnelling and Andreev tunnelling, respectively. White lines over the plot are line graphs of G versus V_{SD} through the middle of the states labelled **4**, **1**, and **3**. Apparently, the Δ -feature is enhanced in the Kondo state **3**, which can either be due to a Kondo resonance persisting on one side of the QD for asymmetric coupling [47] or to Kondo correlations surviving on both sides when $k_B T_K > \Delta$ [50; 56]. Without further analysis, both explanations seem possible in this case. Multiple Andreev reflections emerge in **4**, **1**, and **2**, corresponding to third order processes for $V_{SD} = \pm 2\Delta/3e$.

In addition to the subgap structure, a narrow ridge shows up around $V_{SD} = 0$ mV. We exclude thermally activated direct quasi-particle tunnelling

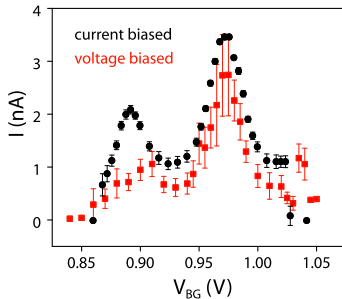


Figure 4.8: Comparison of values of I_C obtained from current and voltage biased data with different methods, as described in the main text. A constant BG shift between the two measurement is corrected.

as the origin of this ridge, because the peak assigned to that effect in the previous chapter appeared only at temperatures above 400 mK, whereas the present data corresponds to a cryostat temperature of 40 mK. Similar features were attributed to Andreev states under finite relaxation in the presence of Kondo correlations [50] or a proximity induced supercurrent in the Fabry-Perot regime [60]. In the latter case, the magnitude of the supercurrent was estimated by half the area under the peak. Since the zero bias ridge we observe is most pronounced in states without Kondo physics, we follow the interpretation of [60]. Both the finite width of the peak and its limited height can be understood in terms of the dissipation introduced by the electromagnetic environment, as discussed in the extended RCSJ model. We thus have the chance to compare values of I_C obtained by different methods from current and voltage biased measurements. First, we repeat the fitting procedure that we already used around $V_{BG} \sim 3.6$ V [39]. We fit a solution of the extended RCSJ model to I-V curves from current biased measurements. However, we do not have enough dI/dV data (AC excitation) for this gate region. Instead, we perform the fits with I-V curves from DC voltage measurements. We know that these measurements suffer from very low frequency random drifts in the voltage amplifier that need to be corrected manually, producing errors that are not accounted for in the error bars of the fitting results. In the gate region around $V_{BG} \sim 3.6$ V, I_C fits from DC data were overall very similar to the ones from AC data, but with 10 %-30 % larger peak values. The values of I_C gained from these fits are shown in black in Fig. 4.8.

Next, we try to extract I_C from the area under the ridge in Fig. 4.7b.

This is tricky because of the substantial background due to MAR processes. We look at individual cuts of G versus V_{SD} and fit the zero bias peak to a Lorentzian form that uses the baseline offset y_0 , the center of the peak x_0 , the full width of the peak at half height w , and the area under the peak A as free parameters. It is clear that such a fit can only be precise to an order of magnitude, because it implies a bias independent background, which is certainly not the case on resonance. Nevertheless, it is interesting to note that the resulting values, shown in Fig. 4.8 in red, agree reasonably well with the more precise current biased data. Please note, however, that these are values corresponding to the **full** area under the peaks, in contrast to [60]. In our opinion, this result implies that the zero bias peak can be interpreted as directly related to the supercurrent, but not used as a reliable measure of its precise value.

4.5 Summary

In conclusion, we have studied the interaction between Kondo correlations and a supercurrent I_C in a SWCNT QD with superconducting leads. In particular, we have analysed how I_C responds to changes in the Kondo temperature T_K in a regime where $k_B T_K \sim \Delta$. In agreement with FRG calculations, we observe the transition of the unpaired spin on the QD from a nonmagnetic singlet state ($k_B T_K > \Delta$) to a magnetic doublet state ($k_B T_K < \Delta$). By tuning T_K via V_{BG} , we can control this transition.

Chapter 5

Topgated Ge/Si Nanowires with Superconducting Leads

In this chapter, we present transport measurements on a topgated Ge/Si core/shell nanowire (NW) with superconducting leads. The motivation to work with Ge/Si NW instead of single-wall carbon nanotubes (SWCNT) is provided by the results of the previous two chapters. We have seen there that the interplay between Kondo physics and superconductivity depends decisively on the coupling strength between the quantum dot (QD) and the leads, $\Gamma = \Gamma_S + \Gamma_D$, as well as the coupling asymmetry Γ_S/Γ_D . It would therefore be highly desirable to work with a device where $\Gamma_{S,D}$ can be tuned independently. Ge/Si core/shell NW appear very promising in this respect because of the possibility to define tunable tunnel barriers within them by application of topgates (TG).

5.1 Introducing remarks

The NW used in this chapter¹ consist of a (semiconducting) Ge core with a diameter of typically 10-15 nm, enclosed in a 1.7 nm thick Si mantle. Electrical transport takes place via hole states through the Ge core, while the Si mantle prevents the formation of a Schottky barrier [61] and enables ohmic contact to source (S) and drain (D) leads. By choosing 30 nm of Al for the leads, we obtain transparent superconductor-semiconductor contacts at low temperatures (Fig. 5.1a). A QD is defined by TG composed of Ti/Au

¹NW growth by Y. Hu in the group of C. Lieber, Harvard University.

(5 nm/50 nm) that locally deplete the density of states (DOS) in the NW, thus creating tunnel barriers whose transparency can be tuned by the voltages applied to the TG, $V_{TG1,2}$ (Fig. 5.1c) [43]. A 5 nm thick layer of Al_2O_3 grown by atomic layer deposition (ALD) isolates the TG from the NW.

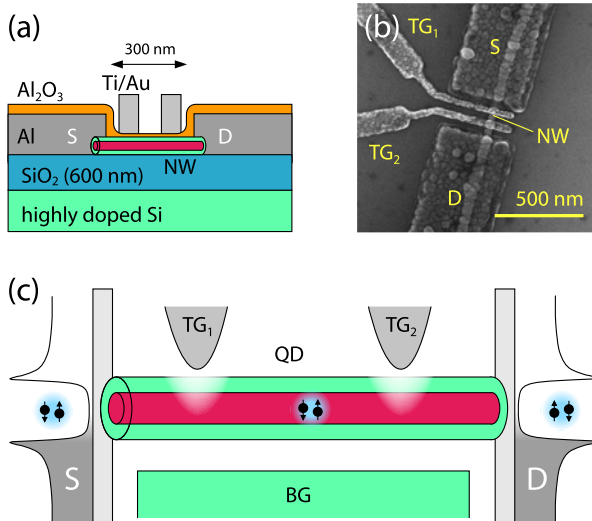


Figure 5.1: **a** Cross section of the NW with S and D electrodes, TG and backgate (BG). **b** Scanning electron micrograph of a NW device identical to the one measured. **c** Schematic representation of the desired functionality: A NW is coupled to superconducting leads through transparent contacts. A QD is formed between the TG which locally deplete the DOS in the semiconducting NW.

Previous studies [62] have established that a superconducting proximity effect can occur in Ge/Si core/shell NW. Multiple Andreev reflections (MAR) and gate dependent critical currents were observed. However, the contact separation was reported as 100-150 nm in that case, whereas we are forced to increase it to 300 nm in order to make space for the two TG (Fig. 5.1a and b).

5.2 Results

Fig. 5.2 presents room temperature measurements of the response of G to the backgate (BG) voltage V_{BG} and TG voltages V_{TG1} and V_{TG2} . In Fig. 5.2b,

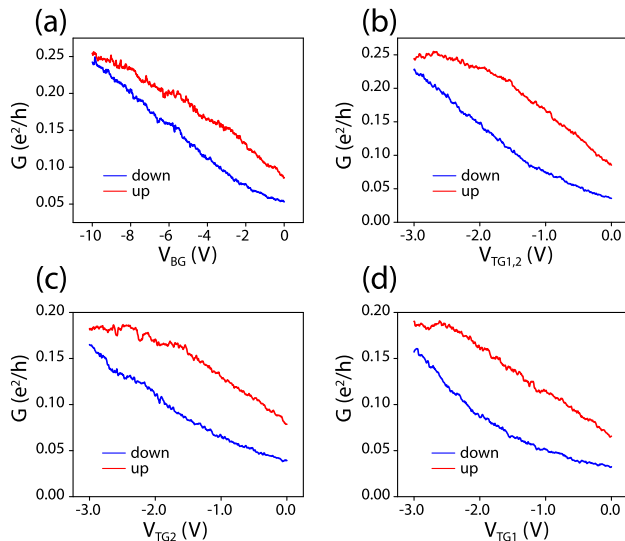


Figure 5.2: Gate response of G to various gate voltages: **a** G versus V_{BG} . **b** G versus $V_{TG1,2}$, applied to both TG simultaneously. **c** G versus V_{TG2} . **d** G versus V_{TG1} .

the same voltage is applied simultaneously to both TG. All gate voltages not indicated in a graph are floating. The device exhibits characteristic changes in G associated with the accumulation/depletion of charge carriers in a semiconductor. Since electrical transport is mediated by holes, a negative gate voltage raises the DOS, thus increasing G . When both TG are active, the slope of the graph is slightly steeper than for only one TG, because the **global** gating effect of the individual TG on the NW DOS adds up. From these data, we cannot determine if the TG have the desired **local** gating effect.

We now turn towards measurements at low temperatures. In order to prevent freezing out of the DOS in the NW, it is helpful to apply strong negative gate voltages during cooldown. Without this method, we find that the device quickly loses its conductivity as thermal activation of charge carriers is reduced, and cannot be reactivated at low temperatures. We therefore apply $V_{BG} = -32$ V and $V_{TG1,2} = -4$ V during cooldown procedure. Fig. 5.3a shows a plot of G versus V_{BG} and V_{SD} at a temperature of 250 mK and with a magnetic field of 0.1 T applied to suppress superconductivity. Both

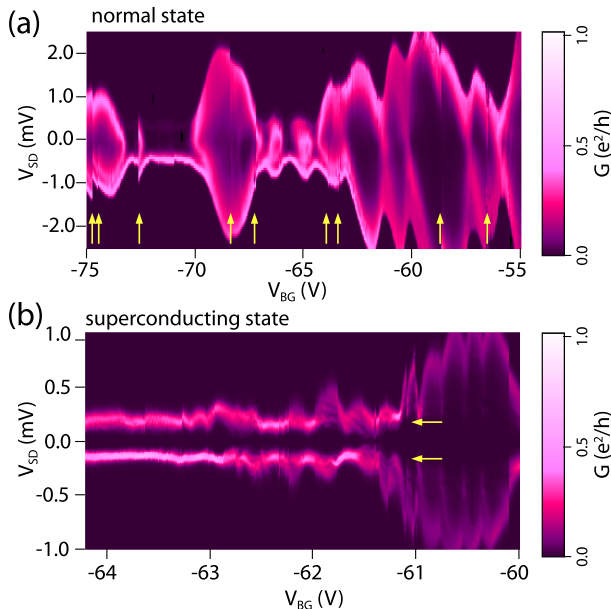


Figure 5.3: **a** Plot of G versus V_{BG} and V_{SD} in the normal state at a temperature of 250 mK and with $V_{TG1,2} = -4$ V. **b** Plot of G versus V_{BG} and V_{SD} in the superconducting state, this time for $T_{ph} = 25$ mK and with $V_{TG1,2} = 0$ V.

TG are at -4 V, which is the maximum voltage we dare to apply without risking an electrical breakdown in the Al_2O_3 layer. We see Coulomb blockade (CB) diamonds with varying size, indicating that the charging energy U_C is not constant over many charge states. In certain regions, U_C appears to be too small to produce well resolved CB diamonds. Yellow arrows mark positions of charge instabilities in the dielectric surrounding the device. We suspect the Al_2O_3 layer to be a major source of these instabilities, because they turn up much more frequently here than in previous samples without TG. No Kondo effect is observed in any of the charge states.

Next, we switch the magnetic field to allow superconductivity in the leads. A measurements of G versus V_{BG} and V_{SD} with $B = 0$ T is shown in Fig. 5.3b, at a temperature of $T_{ph} = 25$ mK and with $V_{TG1,2} = 0$ V. Again, we observe CB diamonds of varying size, but this time, there is a region of low G for bias voltages between $\sim \pm 0.2$ mV. Presumably, this is due to the gap in the superconducting DOS of the leads that we expect to dominate

electrical transport between $V_{SD} = \pm 2\Delta$. The distinct features at constant bias (arrows) are cautiously interpreted as the onset of direct quasi-particle tunnelling. The value for Δ corresponding to the gap size, $\Delta \sim 90 \mu\text{eV}$, is close to the anticipated energy. By following [62], we calculate the according BCS coherence length as $\xi_0 = \hbar\nu_F/\pi\Delta \sim 300 \text{ nm}$ with $\nu_F = 1.5 \times 10^5 \text{ m s}^{-1}$. Please note that this is equal to the spacing between S and D, which we could not reduce due to limitations in the lithography process. In the absence of clear signatures of Andreev processes like MAR, we leave superconductivity aside and focus on the effect of the TG instead.

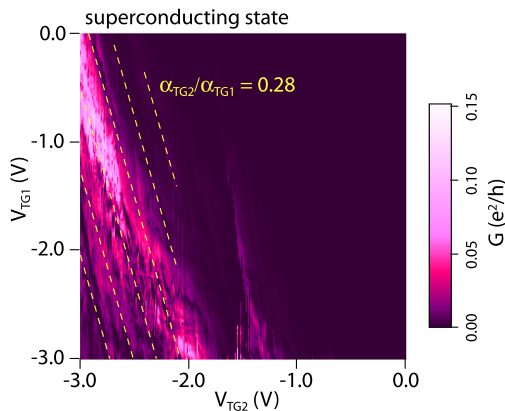


Figure 5.4: Plot of G as a function of V_{TG1} and V_{TG2} for $B = 0 \text{ T}$, $V_{SD} = 0 \text{ V}$, and $V_{BG} = -60 \text{ V}$. From the slope of the CB peaks (yellow dashed lines), we can estimate the relative efficiencies of the two TG.

Since our goal is to study the **local** gating effect of the two TG, we first need to determine their **global** gating effect, and learn how to cancel it. Fig. 5.4 shows a measurement of G as a function of V_{TG1} and V_{TG2} for $B = 0 \text{ T}$, $V_{SD} = 0 \text{ V}$, and $V_{BG} = -60 \text{ V}$. Although interrupted by frequent charge instabilities that manifest themselves as discontinuities with arbitrary slopes, CB peaks can be made out for negative gate voltages. The levels on the QD corresponding to these CB peaks shift in energy as V_{TG1} , V_{TG2} change, and we can follow the evolution of the peaks in order to estimate the relative gating efficiencies α_{TG1} , α_{TG2} . We obtain $\alpha_{TG2}/\alpha_{TG1} = 0.28$ from the slope indicated by yellow dashed lines. This value can then be used to drive the two TG in opposite directions such that their global gating effect on the QD levels cancel. The only changing parameter should then be the

asymmetry of the tunnel barriers under the TG, assuming that they respond to V_{TG1} and V_{TG2} in the intended way.

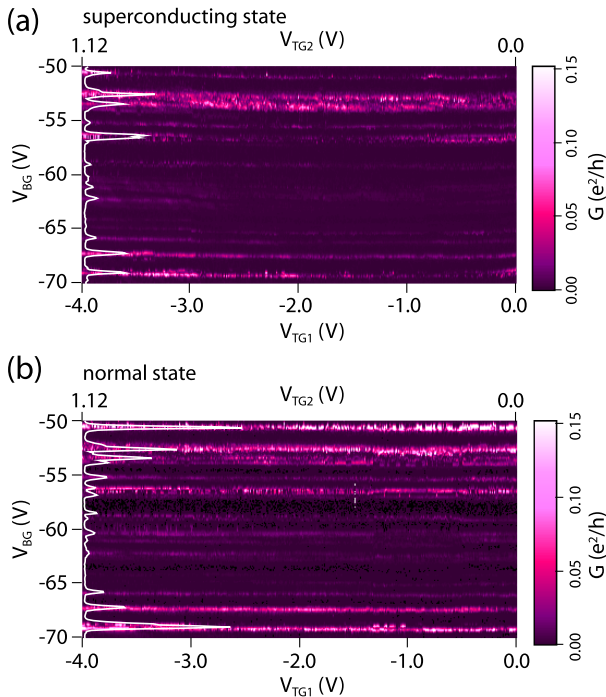


Figure 5.5: CB peaks under the influence of changing TG asymmetry. V_{TG1} and V_{TG2} are plotted at the bottom and top of the figures, respectively. Individual CB peaks appear as horizontal lines. **a** Superconducting state with $B = 0.1$ T. **b** Normal state with $B = 0$ T.

The resulting plots are shown in Fig. 5.5 for $V_{SD} = 0$ V with superconducting (a) and normal (b) leads. Starting from zero voltage (right side), V_{TG1} and V_{TG2} are driven to negative and positive voltages until they arrive at $V_{TG1} = -4$ V and $V_{TG2} = 1.12$ V, respectively (see scales at top and bottom of plot). In vertical direction, CB peaks can be traced as a function of V_{BG} , as indicated by white line graphs of G versus V_{BG} . Clearly, the contributions of the two TG on the QD level energies cancel, because the positions of the CB peaks with respect to V_{BG} are unaffected by the horizontal

axis. The ratio $\alpha_{TG2}/\alpha_{TG1} = 0.28$ extracted from Fig. 5.4 is obviously valid over a large range of both V_{BG} and V_{TG} . Surprisingly, though, the change in V_{TG1}/V_{TG2} taking place from right to left seems to have no effect on the amplitude of the CB peaks whatsoever. According to the Breit-Wigner formula

$$G \propto \frac{4\Gamma_S\Gamma_D}{(\Gamma_S + \Gamma_D)^2} \quad (5.1)$$

we expect to observe a modulation of the peak height with changing asymmetry. For large asymmetry, the CB peaks should be considerably suppressed. The constant peak height suggests that our TG have no local effect on the QD tunnel barriers. Instead, we can only make out the global gating effect on the NW DOS and the QD level positions. This is in contrast to the results obtained in [63]. The only difference between the two measurements in Fig. 5.5 is an overall lower G with superconducting leads, which is related to the gap we observed in Fig. 5.3b.

5.3 Summary

The measurements discussed in this chapter represent our first steps towards a Josephson device with tunable tunnel barriers. A Ge/Si core/shell NW with superconducting leads is studied. Two TG are defined between the leads in addition to a BG. We observe CB diamonds with varying size at low temperatures, and a conductance gap that appears when the leads are superconducting, and which we interpret as the suppression of quasi-particle for bias voltages between $\pm 2\Delta$. However, no signature of Kondo physics or higher order Andreev processes is found. On the one hand, we are limited by the small U_C of < 0.5 meV in certain BG regions, which makes it difficult to resolve features inside CB diamonds spectroscopically. On the other hand, an estimation of the superconducting BCS coherence length ξ_0 yields a value close to the spacing L between our contacts. In contrast to previous work on Ge/Si NW Josephson junctions [62], we can therefore not claim to be in a regime where $L \ll \xi_0$. Finally, we drive our TG in opposite directions such that the energies of the QD levels remain constant, yet are unable to control the coupling of the QD to the leads via V_{TG1}/V_{TG2} , which we find very surprising. The results motivate us to return to SWCNT based devices, where we obtained more favourable values for Γ/U_C and Γ/Δ in the past.

Chapter 6

Topgated Carbon Nanotubes with Superconducting Leads

In this chapter, we report on transport measurements through topgated single-wall carbon nanotubes (SWCNT) with superconducting leads. Because of the limitation that we encountered during our work with Ge/Si core/shell nanowires (NW) in chapter 5, we decided to return to SWCNT based devices with a similar geometry. Indeed, the results are much more encouraging, both with respect to Kondo physics and superconducting proximity effect. We discuss data from two devices that attract our attention for different reasons. The measurements are rather recent, and the interpretation must be regarded as work in progress.

6.1 Introducing remarks

A schematic illustration of our device is shown in Fig. 6.1a, next to a scanning electron micrograph in Fig. 6.1b. A SWCNT is contacted to source (S) and drain (D) leads composed of Ti/Al (5 nm/46 nm). The spacing between S and D amounts to 450-500 nm. Topgates (TG) consisting of 50 nm of Pd are added on top of a 5 nm thick Al_2O_3 layer grown by atomic layer deposition (ALD). A quantum dot (QD) is defined by tunnel barriers forming at the interfaces of the SWCNT to the leads, resulting in a finite coupling strength $\Gamma_{S,D}$ of the QD to S or D. The TG are patterned directly at these interfaces with the intention of controlling $\Gamma_{S,D}$ via the overlap of the orbital part of the electron wave function on the QD with the leads. This requires

a high precision in the alignment of the TG, which makes the lithography process more challenging than for our previous devices. The functionality we ultimately aim for is displayed in Fig. 6.2: by adjusting Γ_S and Γ_D individually, we would like to control the level broadening and the strength of the Kondo correlations on our QD in the presence of superconducting leads.

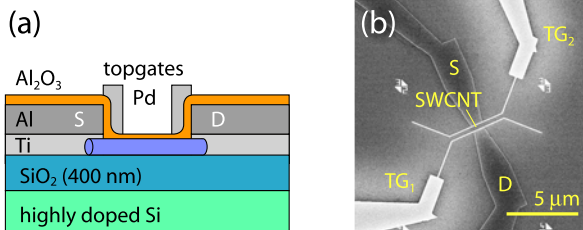


Figure 6.1: **a** Cross section of the nanotube with electrodes and backgate. **b** Scanning electron micrograph of a finished device.

An important issue concerns the choice of dielectric to isolate the TG from the carbon nanotube. Early devices in other groups employed a 40 nm thick layer of SiO₂ grown by plasma enhanced chemical vapour deposition (PECVD) [64]. Later experiments relied on 4 nm of Al₂O₃¹ [65] or 10-15 nm of SiO₂ [46] evaporated locally under the TG. The motivation behind this was the suspicion that the oxide layer could be responsible for scattering in the carbon nanotube as well as charge instabilities that produce discontinuities during gate sweeps. Recently, ALD grown Al₂O₃ has become an attractive alternative because of the uniformity of the dielectric and the reliability against electrical breakdown [66; 67].

Since we are looking for Kondo physics and superconducting proximity effect, we are only interested in devices that display a room temperature resistance below 100 kΩ. Unfortunately, we find this criterium only to be fulfilled by metallic SWCNT, who have a high charge carrier density and cannot be depleted locally. In the following, we will discuss data from two metallic SWCNT ‘A’ and ‘B’. In A, we observe interesting subgap features, while we concentrate on a TG tunable Kondo effect under ferromagnetic exchange interaction in B. Due to a systematic error during fabrication, one TG has a short to the device in both cases and is kept floating. In the following, we only consider the effect of the remaining TG.

¹2 nm of Al was evaporated, followed by an oxidation step. This process was repeated to obtain 4 nm of Al₂O₃.

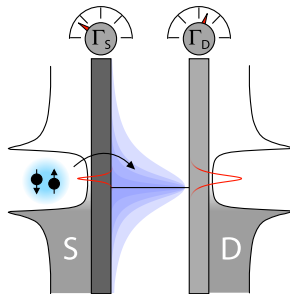


Figure 6.2: The desired functionality of a tunable Josephson QD: adjustable $\Gamma_{S,D}$ allow for controllable level broadening and Kondo correlations in the presence of superconducting leads.

6.2 Results for device A

Fig. 6.3a shows a measurement of the differential conductance G through device A versus backgate (BG) voltage V_{BG} and bias voltage V_{SD} . The superconducting critical field is experimentally determined to amount to $\sim 0.2 \text{ T}^2$. We apply $B = 0.4 \text{ T}$ and $V_{TG} = 0.3 \text{ V}$ for the present measurement. In this BG region, the device exhibits Coulomb blockade (CB) diamonds with a charging energy $U_C \sim 0.2\text{-}0.3 \text{ meV}$ as estimated from the size of the smallest diamonds. We do neither observe Kondo correlations nor a distinct even-odd alternation in the size of the diamonds, so we cannot identify the occupation of the highest orbital on the QD.

Let us analyse the conduction pattern around the resonance at $V_{BG} = 9.35 \text{ V}$ more closely. In addition to the CB diamonds, we can see lines running parallel to the diamond edges, and very faint horizontal ridges crossing the central (right) diamond at about $V_{SD} = \pm 0.03 \text{ mV}$ ($\pm 0.11 \text{ mV}$). We interpret these as signatures of excited states and inelastic cotunnelling thresholds, see e.g. [65].

With $B = 0 \text{ T}$, the leads become superconducting, and the stability diagram is modified (Fig. 6.3b). Strong horizontal lines at $V_{SD} = \pm 0.143 \text{ mV}$ and $\pm 0.088 \text{ mV}$ are interpreted as the onset of direct quasi-particle tunnelling and the first Andreev reflection, respectively. Interestingly, we find that the V_{SD} values at which these two features appear can be increased by

²This value is unusually high. We ascribe it to the fact that the magnetic field we apply lies in the wafer plane. The cross section of the superconducting leads in the field is therefore very small.

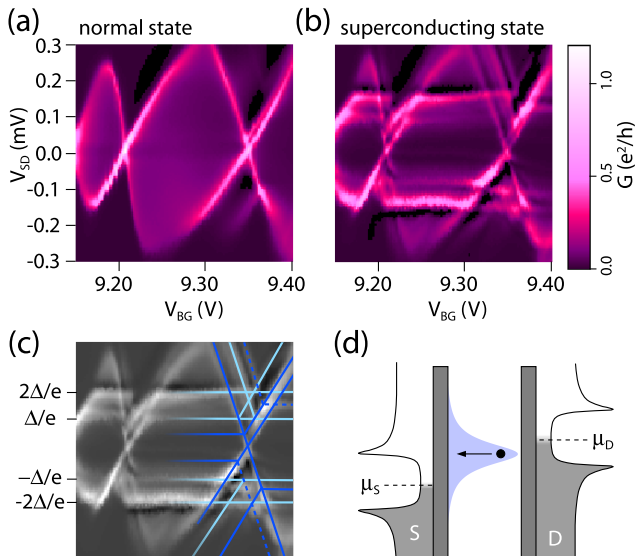


Figure 6.3: **a** G versus V_{BG} and V_{SD} with $B = 0.4$ T and $V_{TG} = 0.3$ V. **b** The same measurement repeated for $B = 0$ T. **c** Surprisingly, the normal state features (dark blue) persist in the superconducting state. **d** Following [68], we propose the existence of subgap quasi-particle states in the superconducting DOS of our leads.

$\sim 10\%$ for different V_{TG} , but their ratio never exceeds ~ 1.7 . We speculate that the negative differential conductance next to the 2Δ -feature (black regions) causes a shift in the apparent position of the peak and effectively reduces the measured Δ . Around resonance, several additional lines appear parallel to the diamond edges, representing the energetically split CB diamonds due to the BCS density of states (DOS) in the leads (chapter 1). However, the splitting is incomplete, amounting to less than $\pm 2\Delta/e$. Even more surprisingly, the normal state features are still visible, in contrast to our expectations. Similar transport behaviour was observed in InAs NW [68] and attributed to the existence of quasi-particle states within the superconducting gap [69].

For better comparison, we extract all lines from the measurements with normal and superconducting leads independently, and plot them together in Fig. 6.3c. Dark blue lines correspond to features that we observe in the normal as well as the superconducting state. Dashed lines are extracted from

the superconducting state, but their positions suggest that they originate from normal state processes. Obviously, these features represent resonant tunnelling through the ground state and first excited state of the QD, although it is unclear why they persist when the leads are superconducting. One possible source for subgap quasi-particle states is the Ti layer of the leads that profits from proximity induced superconductivity. Fig. 6.3d shows an illustration of a QD with superconducting leads that have a non-vanishing quasi-particle DOS within the gap, as proposed in [69]. Bright blue lines in Fig. 6.3c mark features that are clearly related to superconductivity, namely the onset of direct quasi-particle tunnelling at $V_{SD} = \pm 2\Delta/e$, the first Andreev reflection at $V_{SD} = \pm\Delta/e$, and CB diamond edges split apart in bias voltage by the superconducting gap. However, the CB diamonds split up by $V_{SD} = \pm\Delta$ instead of $\pm 2\Delta$. This is in agreement with a finite subgap quasi-particle DOS in the leads, as one can see in Fig. 6.3d: a level is pinned to the upper peak in the BCS DOS of S. Because of the existence of subgap quasi-particles in D, this situation will result in resonant transport of electrons from D to S down to a bias voltage of $V_{SD} = \Delta/e$. The line then merges into the horizontal feature marking the lowest order Andreev reflection.

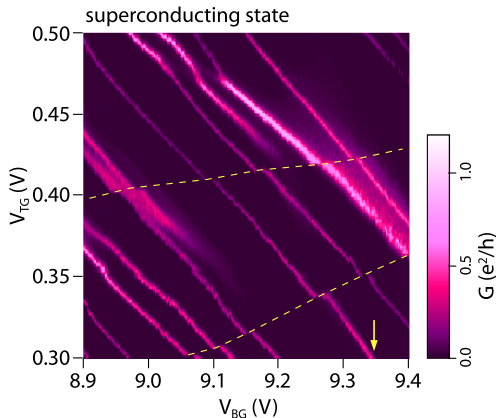


Figure 6.4: G versus V_{BG} and V_{TG} for $B = 0$ T and $V_{SD} = 0$ V.

Fig. 6.4 shows a measurement of G versus V_{BG} and V_{TG} , with $B = 0$ T and $V_{SD} = 0$ V. Yellow dashed lines indicate charge instabilities in an oxide layer resulting in gating discontinuities. Apparently, the instabilities are

sensitive both to the TG and the BG, and switch reproducibly at certain positions within the potential landscape. The CB resonance that we studied in Fig. 6.3 is marked by an arrow at the corresponding TG voltage. The energies of the levels on the QD shift with V_{TG} with well defined slopes, reflecting the global gating effect of the TG. At second glance, we realize that the distance between CB resonances, as well as their conductance, vary with V_{TG} . We ascribe this to changes in the orbital part of the electron wave function on the QD, which influences the overlap between the QD and the leads. Thus, although our SWCNT is metallic, we face a system of discrete resonances with tunable amplitude. In the following, we will study a second device where we apply this tunability to the Kondo effect.

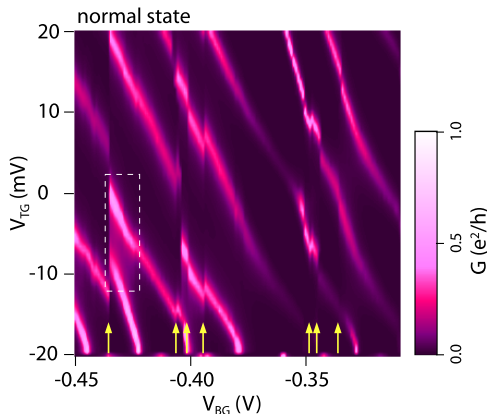


Figure 6.5: G versus V_{BG} and V_{TG} for $B = 0.4$ T and $V_{SD} = 0$ V in a second device, B. Charge instabilities appearing at certain values of V_{BG} are marked by yellow arrows.

6.3 Results for device B

In Fig. 6.5, we present a similar measurement as in Fig. 6.4, but for device B and with an applied magnetic field of $B = 0.4$ T. We can observe bright lines, corresponding to resonant transport, whose position in V_{BG} changes with V_{TG} . Charge instabilities (yellow arrows) seem to be insensitive to V_{TG} for this device, because they appear at constant V_{BG} . The most interesting regions of this figure are those where two resonances approach each other

and the conductance between them increases, e.g. as highlighted by a white, dashed frame. In the following, we will study one of these regions in detail and discover that the feature is due to a TG dependent Kondo correlation.

Fig. 6.6a displays the same feature as inside the white frame in Fig. 6.5. By restricting ourselves to a smaller V_{BG} range, we can minimize the effect of gate switching due to charge instabilities, which is a precondition for a systematical analysis. At this point, we have no information regarding the occupation of the QD (odd/even), but we anticipate our later results and identify the two levels as odd (**o**) and even (**e**). Before turning our attention to the normal state behaviour of the **o** diamond, we shall have a look at the charge transport with superconducting leads.

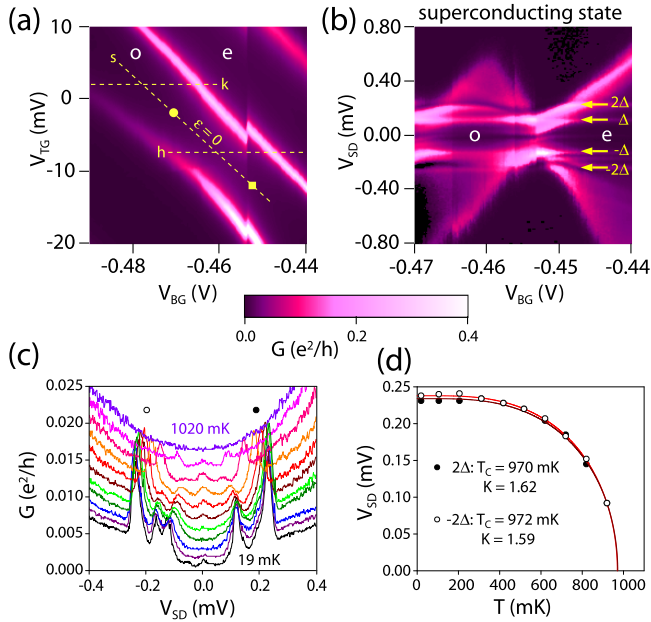


Figure 6.6: **a** Plot of G versus V_{BG} and V_{TG} in the region we will study in the following. The dashed lines **h**, **k**, and **s** mark the voltage range for subsequent measurements. **b** Charge stability diagram with superconducting leads, corresponding to the dashed line **h** in figure **a**. **c** Cuts of G versus V_{SD} for rising temperatures through the middle of a CB diamond. **d** Temperature dependence of the 2Δ peak positions. We obtain $\Delta_0 = 1.41k_B T_C$ instead of the usual BCS factor 1.76.

By switching off the magnetic field, we allow the leads to become superconducting. Fig. 6.6b depicts a measurement of G versus V_{BG} and V_{SD} for $B = 0$ T and $V_{TG} = -7.5$ mV. The matching values of V_{TG} and V_{BG} are marked in Fig. 6.6a by a horizontal line (**h**). We see the two CB diamonds **o** and **e** in addition to horizontal lines that we interpret as the onset of direct quasi-particle tunnelling at $V_{SD} = \pm 2\Delta/e$, and Andreev reflections at $V_{SD} = \pm\Delta/e$. The value of Δ that we extract from the spacing of the quasi-particle tunnelling peaks, $240 \mu\text{eV}$, is associated with a critical temperature $T_C = 790$ mK, which is lower than in previous devices (chapters 3-4). In order to obtain a more reliable value of T_C , we measure G versus V_{SD} for different temperatures in the middle of a CB diamond without Kondo correlations. Fig. 6.6c shows the resulting plot, where we use an offset of $10^{-3} e^2/h$ between subsequent curves for better visibility. We can trace the evolution of the peak positions with temperature, noticing that the Δ -features are still present at the second to highest temperature (920 mK). At 1020 mK, however, all signs of superconductivity are gone. In a next step, we determine the peak positions of both 2Δ -features for every measurement and plot them versus T (Fig. 6.6d). A fit to the BCS function

$$2\Delta(T) = K \cdot 1.76k_B T_C \tanh(1.74\sqrt{T_C/T - 1}) \quad (6.1)$$

yields in both cases $T_C \sim 970$ mK and $K \sim 1.6$. While this value of T_C is in good agreement with values in previous chapters, the suppression of K below 2 is a surprise, because BCS theory predicts that $\Delta(0) = \Delta_0 = 1.76k_B T_C$. We note that the Δ -feature appears at $V_{SD} = \pm 120 \mu\text{V}$, which is exactly half of $2\Delta/e$, as expected. The most obvious conclusion to be drawn from this observations is that the BCS relation $\Delta_0 = 1.76k_B T_C$ is not valid in our device. Rather, we get $\Delta_0 = 1.41k_B T_C$.

We would now like to focus on the normal state characteristics of the CB diamond labelled **o**. Fig. 6.7a shows a measurement of G in dependence of V_{BG} and V_{SD} with an applied field of $B = 0.4$ T, and $V_{TG} = 2$ mV. The corresponding voltage range is marked in Fig. 6.6a by the dashed line **k**. In addition to the edges of the CB diamond, which are very faint on its left side, a ridge of increased G can be seen around $V_{SD} = 0$ V that we attribute to the spin-1/2 Kondo effect. The fact that no Kondo correlations are observed in the normal state in **e** (data not shown) supports our interpretation of odd/even occupation of the QD for the two levels. In order to establish if the approaching of resonant lines and increased conductance in Fig. 6.6a is correlated to Kondo physics, we measure G versus V_{SD} and V_{TG} while at the same adjusting V_{BG} to stay at the center of the level ($\epsilon = 0$). This means that we drive V_{TG} and V_{BG} in opposite directions with relative rates determined from the slope of line **s** in Fig. 6.6a, and follow the development

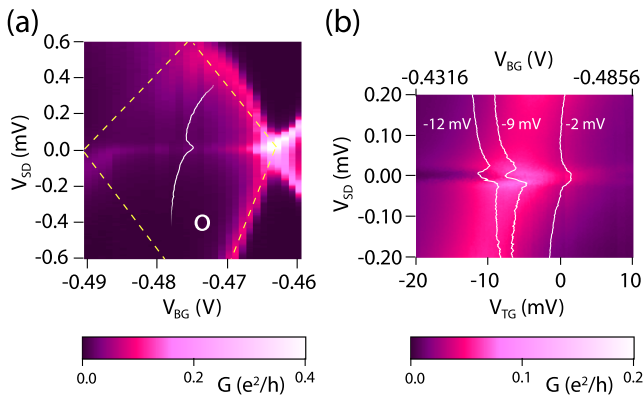


Figure 6.7: **a** G versus V_{BG} and V_{SD} for $B = 0.4$ T and $V_{TG} = 2$ mV. A Kondo ridge is observed around $V_{SD} = 0$ V throughout the diamond marked by yellow dashed lines. **b** G in dependence of V_{SD} along the line **s** in Fig. 6.6a, with $B = 0.4$ T. V_{BG} is used to stay at the center of **o** as we drive V_{TG} . The Kondo ridge, which is split for $V_{TG} = -20$ mV, evolves into a single peak at $V_{TG} = 10$ mV.

of the Kondo ridge along this line. The resulting plot is shown in Fig. 6.7b. A distinct Kondo ridge is visible at positive and small negative TG voltages. For $V_{TG} < -5$ mV, however, a dip in G develops at $V_{SD} = 0$ V. For $V_{SD} = -20$ mV, the Kondo ridge is clearly split.

Why should a Kondo ridge split? As we have discussed in chapter 1, an applied magnetic field will induce a Zeeman splitting of spin up and spin down components that results in two Kondo ridges at $V_{SD} = \pm g\mu_B B/e$, where $g = 2$ for electrons in a SWCNT, and μ_B is the Bohr magneton. The splitting observed for $V_{TG} = -12$ mV, $\Delta V \sim 50$ μ V, would correspond to $B = 0.21$ T, which is actually much less than the applied field $B = 0.4$ T. Even more mysterious is the emergence of a clear peak for more positive TG values in Fig. 6.7b, as emphasized by a white line graph at $V_{TG} = -2$ mV. Obviously, this transition in dependence of V_{TG} cannot be understood in terms of Zeeman splitting alone.

In order to characterize the response of the Kondo ridge to B , we measure G as a function of B and V_{SD} at the positions highlighted in Fig. 6.7b. Fig. 6.8a presents the result for $V_{TG} = -2$ mV. A linear background is subtracted in all graphs of Fig. 6.8. At low magnetic field, superconductivity dominates electrical transport, preventing the appearance of the Kondo effect. For $|B| > 0.2$ T, superconductivity is suppressed, and we can follow the

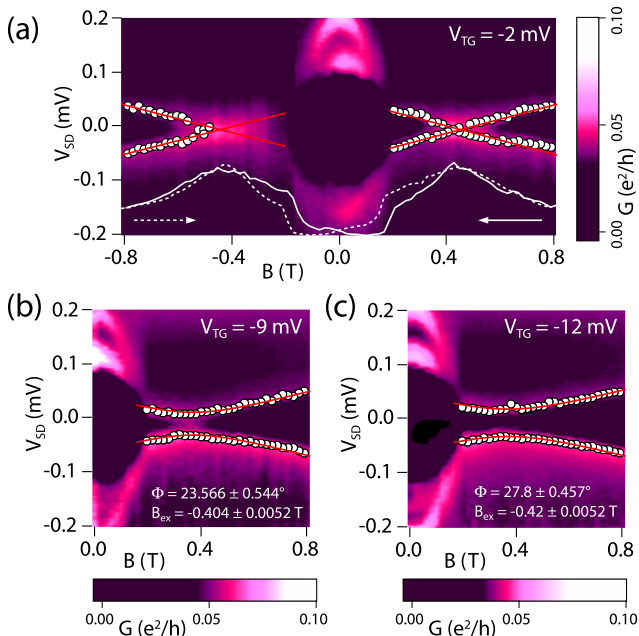


Figure 6.8: Response of G versus V_{SD} to an applied magnetic field B , with a sweep direction from positive to negative field. A linear background is subtracted in all data. **a** Measurement for $V_{TG} = -2$ mV. At low magnetic field, the Kondo effect is suppressed by superconductivity. For $|B| > 0.2$ T, we can observe linear splitting of the two spin components with magnetic field. The crossing at finite field indicates the presence of a ferromagnetic exchange field B_{ex} as explained in the main text. White dots correspond to maximum values of G , red lines represent linear fits with $g \sim 2.24$. **b** A similar measurement at $V_{TG} = -9$ mV reveals an avoiding in agreement with the dip in Fig. 6.7b at the respective value of V_{TG} . Red lines represent fits to a model assuming a constant exchange field B_{ex} with an angle ϕ relative to B . **c** For $V_{TG} = -12$ mV the dip becomes more pronounced.

evolution of the two spin components of the Kondo ridge in B . White dots correspond to maximum values of G , red lines represent linear fits. From the slope of these lines, we estimate $g \sim 2.24$, roughly consistent with a spin-1/2 Kondo effect. The most striking feature of the measurement is the fact that the two spin components do not cross at $B = 0$ T, but at $B \sim \pm 0.44$ T. A white solid (dashed) line depicts the equilibrium conductance as a function of B for a sweep from $B = 0.8$ T to -0.8 T (vice versa). A hysteretic

behaviour is apparent from the mirror symmetry in this data. Fig. 6.8a is reminiscent of the Kondo effect in a system coupled to a ferromagnetic material, where an effective exchange field B_{ex} is introduced by tunnelling events between the QD and the ferromagnet [70; 49; 71; 72]. In such systems, the spin up and spin down components are energetically degenerate when B_{ex} is compensated by B , resulting in a crossing of the lines [71; 72]. However, in contrast to the experiments described in [70; 71; 72] there are no ferromagnetic parts in the metal film of our device, and neither in the chip carrier or the bonding wires. The only possible source of a ferromagnetic exchange field are Fe catalyst particles that enable the growth of SWCNT by the chemical vapour deposition method (see chapter 2). These particles are naturally expected to remain in the vicinity of the SWCNT after their growth, and it is feasible that a tight coupling between the SWCNT QD and a Fe particle results in a magnetic exchange field. Indeed, exactly this concept was invoked to interpret a Kondo splitting at $B = 0$ T in a device consisting of a SWCNT contacted to Cr/Au leads [49]. Following this work, we propose a ferromagnetic exchange field B_{ex} , induced by a Fe catalyst particle close to the SWCNT QD, to be the most likely explanation for the observation of a hysteretic crossing of the two spin components at finite B .

We notice a qualitatively different behaviour upon repeating the measurement for $V_{TG} = -12$ mV (Fig. 6.8b). The lines corresponding to the two spin components of the Kondo ridge still converge at $B \sim 0.4$ T, but this time avoid each other, producing a dip at the according value of V_{TG} in Fig. 6.7b. Again, this can be compared to earlier results, where a misalignment between B and B_{ex} was identified as the origin of such an avoiding [71]. Red lines represent fits to a model assuming a constant exchange field B_{ex} with an angle ϕ relative to B . It is at present unclear whether this interpretation is valid in our case, where crossing and avoiding are observed in the same device and even the same charge state. Still, the TG dependent splitting of the Kondo ridge at $B = 0.4$ T appears to stem from a TG dependent ferromagnetic exchange field that can either result in crossing or avoiding spin components, producing a zero bias peak ($V_{TG} = -2$ mV) or dip ($V_{TG} = -12$ mV) for $B = -B_{ex}$, respectively. We are currently trying to understand this observation.

In Fig. 6.9, we present similar measurements as in Fig. 6.7b for two additional charge states. Both show a split Kondo ridge in dependence of V_{TG} , while V_{BG} is adjusted simultaneously to remain at the center of the charge state ($\epsilon = 0$). The Kondo ridge in Fig. 6.9a is split at $V_{TG} = -5$ mV, evolving into a single peak around $V_{TG} = 5$ mV. Interestingly, a distinct splitting is recovered for $V_{TG} = 10$ mV, demonstrating that this effect is not monotonous with V_{TG} . Finally, the Kondo ridge in Fig. 6.9b remains split for the whole scan range of V_{TG} , but the peak separation decreases

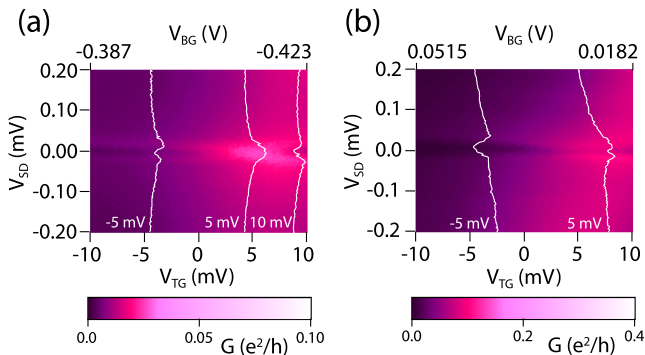


Figure 6.9: Additional measurements of Kondo splitting at $B = 0.4$ T in dependence of V_{TG} in two different charge states: **a** Evolution of a Kondo ridge from zero bias dip to zero bias peak between -5 mV and 5 mV TG voltage. For $V_{TG} = 10$ mV, a distinct zero bias dip (splitting) is recovered. **b** Kondo ridge with decreasing peak separation between $V_{TG} = -5$ mV and $V_{TG} = 5$ mV.

from $V_{TG} = -5$ mV to $V_{TG} = 5$ mV, signalling an incomplete development towards a zero bias peak.

Coming back to Fig. 6.5, we suggest that we have identified the mechanism that gives rise to regions of increased G and reduced peak spacing, as inside the white frame. Both phenomena can be attributed to the manifestation of a Kondo effect whose behaviour around zero bias is sensitive to V_{TG} . More precisely, by simultaneously driving V_{TG} and V_{BG} , we can follow the TG dependence of the Kondo effect while staying in the middle of a charge state ($\epsilon = 0$). We observe the evolution of a zero bias dip, corresponding to an avoiding of the two spin components of the Kondo ridge in an external magnetic field B , into a zero bias peak, marking a crossing at finite field. We assign this effect to the presence of a ferromagnetic exchange field B_{ex} , which we suspect is created by the coupling of the SWCNT to a Fe catalyst particle. How exactly this exchange field is influenced by V_{TG} is at present unclear.

6.4 Conclusion for devices A and B

In conclusion, we have studied the electrical transport through two topgated SWCNT devices with superconducting leads. Device A exhibits a rich and highly resolved spectroscopy, allowing us to gain information about the DOS

for quasi-particles in the Ti/Al leads. In device B, we observe a highly interesting effect regarding the tunability of a Kondo state by a TG voltage. The splitting of the Kondo ridge in an external magnetic field B and in the presence of a ferromagnetic exchange field B_{ex} is sensitive to V_{TG} , evolving from a zero bias dip into a zero bias peak. This result, albeit not understood in detail, serves to show that a wealth of new phenomena becomes accessible through the application of TG to SWCNT QD devices, and motivates further research in that direction.

Chapter 7

Summary and Outlook for Chapters 3-6

In this thesis, we study quantum dots (QD) fabricated from single-wall carbon nanotubes (SWCNT). The SWCNT are connected to source (S) and drain (D) leads by tunnelling contacts whose transparency is characterized by their respective coupling parameters, Γ_S and Γ_D . The leads consist of a Ti/Al double layer and become superconducting below the critical temperature, $T_C \sim 1$ K. By application of an external magnetic field B , we can suppress superconductivity and drive the leads into the normal state.

We measure the electrical transport through these QD systems at temperatures well below 1 K. The differential conductivity G in dependency of a bias voltage V_{SD} and a backgate voltage V_{BG} reflects the successive filling of electron states on the QD, revealing whether the occupation is odd or even. For an odd occupation and normal metal leads, the Kondo effect will dominate transport when the coupling of the QD to the leads, $\Gamma = \Gamma_S + \Gamma_D$, is large enough. The associated energy scale is parameterized by the Kondo temperature T_K . In the presence of a BCS density of states (DOS) in the leads, a competition sets in between superconductivity and the Kondo effect. Both processes rely on the formation of opposing spin singlet states involving electrons in the leads. For $T_C > T_K$, the Kondo effect is suppressed, whereas it persists in the opposite regime, $T_C < T_K$. Both regimes have previously been studied in similar samples by electrical transport spectroscopy [48; 55].

In chapter 3, we report on the discovery of a third regime by studying a QD with highly asymmetrical coupling, $\Gamma_S/\Gamma_D \sim 50$. With superconducting leads, this asymmetry gives rise to a Kondo effect pinned to one lead only, illustrating the fact that T_K dominates over T_C at one contact, whereas $T_C > T_K$ at the other. As a result, we observe a significant enhancement of

a particular feature in non-equilibrium transport, the Andreev reflection, in states with this kind of asymmetrical Kondo effect.

In chapter 4, we expand our scope of investigation by comparing Kondo physics to the supercurrent I_C that is transported through the QD. We extract the full supercurrent by following a fitting procedure based on the ‘extended resistively and capacitively shunted junction model’ for overdamped Josephson junctions [38; 39]. Using V_{BG} to tune T_K within one odd charge state, we drive the QD from one regime ($T_K > T_C$) to the other ($T_K < T_C$). Since I_C is very sensitive to the Kondo effect, it acts as a probe for the transition that occurs at the crossing between the two regimes [54]. In a second odd charge state with larger Γ , T_K is always larger than T_C , and consequently no transition is observed.

Chapters 5 and 6 document our efforts to gain more direct control over the Kondo effect by means of topgates (TG). Ideally, such TG would allow us to tune Γ_S and Γ_D individually, thus greatly increasing the possibilities for comprehension and manipulation of these complex systems. In chapter 6, we report on a TG dependent Kondo effect in the presence of an effective ferromagnetic field [70; 71]. Albeit not based on direct control over $\Gamma_{S,D}$, this result has caught our interest and might stimulate further research in the same direction.

Future experiments with supercurrents through QD will likely achieve a much higher degree of control over the properties of individual devices, either by application of TG or by embedding the QD in a superconducting quantum interference device (SQUID), see [54; 57]. With the advent of novel fabrication techniques, it might become routinely possible to obtain high transparency contacts to semiconducting SWCNT, who offer much more tunability in terms of $\Gamma_{S,D}$ than metallic ones. Generally, while SWCNT seem to be a perfect system for the investigation of spin properties in QD, they suffer from a number of problems regarding device fabrication. In addition to the inability to grow semiconducting or metallic SWCNT selectively, the contact quality of individual SWCNT to metallic leads is subject to factors beyond the control of current fabrication techniques. If these issues can be overcome, SWCNT QD devices will become a yet more powerful tool for the exploration of highly correlated electron systems, and maybe even for their application in information technology.

Chapter 8

AMR Measurements in Thin Films

In this chapter, we will give an overview over magnetoresistance measurements performed on thin ferromagnetic films. Since the topic is not directly related to the main part of this thesis, it is presented as a stand-alone segment, including some comments on sample fabrication and measurement setup, but without a complete theory section. We started this side project in order to support research on carbon nanotube spintronics within our group. Our data should be helpful to understand the behaviour of these materials when used as leads to single-wall carbon nanotubes (SWCNT) under varying magnetic fields. The project was later continued and expanded in the project work of J. Hyötylä [73].

8.1 Introducing remarks

Spin transport through SWCNT and through graphene contacted by ferromagnetic leads is attracting a lot of interest due to the prospect of creating spin selective building blocks in information technology [74; 75]. A major challenge in this context is finding a suitable contact material that exhibits large spin polarization as well as good electrical contact to SWCNT/graphene. A very promising option for SWCNT is PdNi alloy (30 % Pd, 70 % Ni) with an estimated spin polarization P^1 of 10 % [76]. However, we know little about the exact magnetic properties of this material, especially since the leads consist of thin films that are created by evaporation. The behaviour

¹ P is defined as $\frac{I^+ - I^-}{I^+ + I^-}$ where I^+ , I^- correspond to the currents of majority and minority spin electrons.

of such films can deviate from that of bulk material due to geometrical constraints or impurities. In this work, we study the anisotropic magnetoresistance signals of PdNi and PdNi/Co films in order to identify their preferred magnetization orientation (easy axis).

8.2 The anisotropic magnetoresistance effect

The term ‘anisotropic magnetoresistance’ (AMR) describes the observation that in ferromagnetic transition metals, a current experiences a resistance that depends on the angle of the current relative to the magnetization of the film. The phenomenological dependence can be written as

$$\rho(\theta) = \rho_{\perp} + \Delta\rho \cos^2(\theta) \quad (8.1)$$

where ρ_{\perp} , ρ_{\parallel} refer to the orientation of the current relative to the magnetization and $\Delta\rho \equiv \rho_{\parallel} - \rho_{\perp}$. θ is the angle between the magnetization and the current path. Often, but not always, ρ_{\parallel} is greater than ρ_{\perp} . A microscopic theory explaining this behaviour implies a two-current model (conductivities for spin up and spin down electrons are separated and additive) in a bulk crystal where s electrons carry most of the current and s-d scattering is dominant. The anisotropy of the magnetoresistance arises from less than cubic symmetry in the s-d scattering caused by spin-orbit interaction [77].

When working with thin films, we have to be aware of some additional implications:

- The size of $\Delta\rho$ depends on film thickness and surface conditions as well as grain size.
- Substrate temperature, vacuum quality and evaporation rate during film deposition are crucial.
- At low temperatures, surface scattering may become dominant over bulk scattering. This can make interpretation of the data difficult. However, a rough Drude model estimation² of the mean free path l_0 in our films reveals $l_0 \sim 1.4$ nm, which is an order of magnitude smaller than the thickness of our films. Bulk scattering should therefore still be important.

²We used $l_0 = \tau * v_0$ where $\tau = m_e / \rho n e^2$ and $v_0 = 0.3 * 10^6$ m/s as in bulk Ni. $m_e = 9 * 10^{-31}$ kg (\sim free electrons), $\rho = 50$ n Ω m from measurements, $n = 1.4 * 10^{29}$ m⁻³ by considering only the s electrons of the Ni

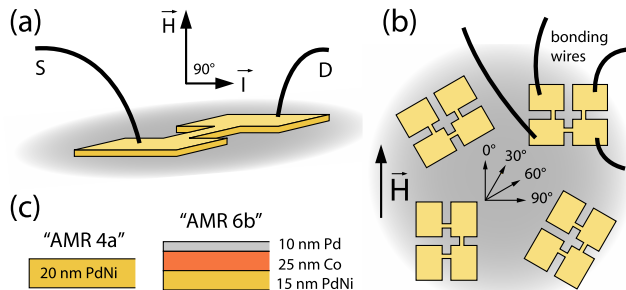


Figure 8.1: Device schematic: **a** Sketch of a device mounted orthogonal to the magnetic field. **b** Sketch of a number of devices mounted parallel to the magnetic field. The orientation of the strips on the wafer corresponds to an angle between the current and the magnetic field. **c** Side view displaying the composition and thicknesses of the metallic films.

8.3 Sample preparation

We lithographically define thin strips ($0.5 \mu\text{m} \times 100 \mu\text{m}$) as conductors between large bonding pads (Fig. 8.1a). Several of these strips are implemented on one wafer piece at different angles (Fig. 8.1b). A thin metallic film is then evaporated in the Balzers PLS 500 system. Evaporation pressures range around $1.0\text{e-}7$ mbar, and the sample is cooled below 273 K. We present data on two devices. The first, labelled ‘AMR 4a’, consists of a single layer of 20 nm PdNi, while the second, ‘AMR 6b’, is composed of 15 nm PdNi + 25 nm Co + 10 nm Pd (Fig. 8.1c). We will discuss both measurements sequentially.

8.4 Measurement setup

An AVS-47 resistance bridge is used to measure the two-point resistance of our strips at low temperatures (4.2 K in a ^4He bath or 1.8 K in a ^4He cryostat). All data is taken at a voltage excitation of $300 \mu\text{V}$ after verifying that the signal is identical to the one taken with an excitation of $100 \mu\text{V}$. Both setups feature a fixed magnet that we sweep between ± 1 T with a rate of 0.1 T/min, again after checking that the signal does not shift relative to lower rates. The amplitude is suppressed by $\sim 0.01\%$ compared to the amplitude at 0.05 T/min, which we think is safe to neglect. Two dipsticks with different sample orientations allow us to mount the devices either such that

the magnetic field direction lies in the wafer plane (‘inplane’) or orthogonal to it (‘out of plane’), as illustrated in Fig. 8.1a and b.

8.5 Results for ‘AMR 4a’

Due to details in the control of the electron beam during lithography, strips with different angular orientation vary slightly in width. Naturally, this leads to variations in their resistance. In order to compare data from several strips in one graph, we normalize them with respect to their resistance at zero magnetic induction, $B = 0$ T, where the strip magnetization points in the direction of the easy axis of the film. For a ferromagnet, this is not the case for zero applied field ($\mu_0 H = 0$ T) because of the unknown intrinsic magnetization M of the material. We use $H = B/\mu_0 - M$, where μ_0 is the permeability of free space, and determine the value of H where $B = 0$ T from the hysteretic shift between magnetic field sweeps in ‘up’ and ‘down’ direction (Fig. 8.2a). This shift of about 0.11 T is in agreement with independent magnetization measurements on extended PdNi films evaporated in our lab [76].

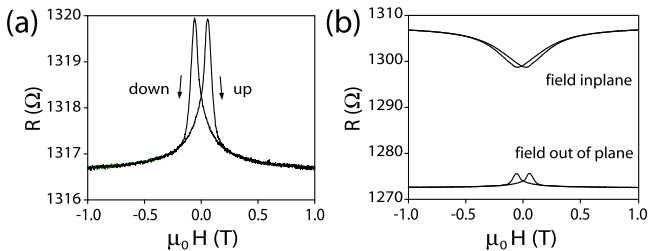


Figure 8.2: **a** Typical AMR signal of the strips on ‘AMR 4a’ with an orthogonal magnetic field. **b** comparison of measurements with inplane and orthogonal magnetic field for one device. The angle between current and the magnetic field was 60° in the inplane case.

Fig. 8.2a displays a typical AMR signal for the devices on ‘AMR 4a’ with the magnetic field orthogonal to the wafer plane. The resistance is highest for $B = 0$ T and saturates at high fields ($\mu_0 H = \pm 1$ T) where the magnetization of the film is forced to point in the direction of H . Although full saturation is not reached at ± 1 T, we will use this value as an approximation for a qualitative discussion. The resistances peak values of the different devices range from 700 Ω up to 3 k Ω , but all devices display the same hysteresis and

relative peak height. The resistance change from $B = 0$ T to $\mu_0 H = 1$ T, normalized by the value at $B = 0$ T, corresponds to the relative peak height and can be identified with $\rho(\theta)$ from Eq. 8.1. On the one hand, if the easy axis of the strip points in the direction of H , we expect to see no peak at all for a single domain, because the magnetization will never rotate away from this axis. Instead, it will flip by 180° when H reaches the coercive field H_{coer} . This flip will ideally not be accompanied by a change in R . On the other hand, if the easy axis and H form an angle of 90° , the magnetization of the film will slowly rotate out of the external field axis as B approaches 0 T, and then rotate back as H increases and forces the magnetization to follow. Both the width of the peak (or the dip) and its magnitude therefore indicates if the measured strip has its easy axis far from the axis of H .

Mounting the sample on a second dipstick with the wafer plane oriented along H yields a different picture. Fig. 8.2b compares two measurements for the same device. The lower curves correspond to an orthogonal magnetic field as in Fig. 8.2a, while the upper curves were taken with the wafer aligned parallel to the field. From the orientation of that specific strip on the wafer surface, we can determine the angle between the current and the external magnetic field H to be 60° . The resistance at $B = 0$ T is not the same in both cases, which we assign to structural changes in the sample between two cooldowns. These data indicate that the easy axis of the film has a strong out of plane component, since the peak width (associated with the magnetization flip) is much narrower for this case. The same tendency is derived from the PdNi magnetization measurements in [76].

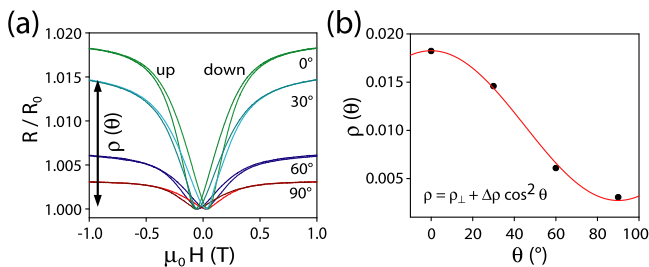


Figure 8.3: **a** Different measurements for inplane external magnetic field normalized by the value for $B = 0$ T, R_0 . **b** Fit to the expected \cos^2 dependency of Eq. 8.1.

An analysis of several strips with different angles relative to the field (see Fig. 8.3a) reveals the expected \cos^2 dependency (Fig. 8.3b). The resistance

is highest when H forces the film magnetization into the direction of the current (0°) and decreases as the angle between the I and H increases. However, the resistance is not flat for 90° , which is in agreement with our assumption of a strong out of plane component of the easy axis. It is quite probable that the non-cylindrical cross section of our wire causes $B \perp I$ **inplane** and $B \perp I$ **out of plane** to be different. As an alternative explanation, we should mention that the wafer, and therefore the strip, is maybe not perfectly aligned relative to the magnet, and the indicated angles could be off by perhaps 5° . A truly 90° measurement might yield a flat line at $R/R_0 = 1$.

Overall, the data from Fig. 8.2b and Fig. 8.3a suggest that the easy axis of the film lies mostly **out of plane**, but has a certain inplane component that forms an angle of almost 90° with the strip direction. The maximum AMR signal $\rho(\theta)$ is seen for $\theta = 0^\circ$ and amounts to nearly 2%.

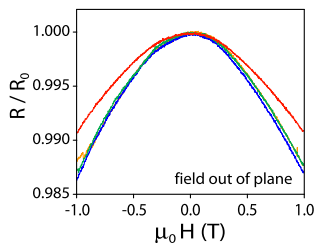


Figure 8.4: ‘AMR 6b’: Measurements for different strips normalized by the maximum resistance of each curve for H orthogonal to the wafer plane. The peaks are much broader than for the PdNi film, and the magnetization does not saturate at 1 T.

8.6 Results for ‘AMR 6b’

The situation is different for the second sample, labelled ‘AMR 6b’, which consists of PdNi, Co and Pd on top of each other (see Fig. 8.1c). In this case, the strong magnetization of Co is expected to dominate the magnetic behaviour of the strip, forcing the PdNi to follow. Let us first have a look at the data for a magnetic field orthogonal to the wafer plane. Fig. 8.4 displays four of these sweeps normalized by the maximum resistance of each curve, which ranges from 370Ω to 485Ω . Three of the sweeps show perfect alignment, while the fourth seems a bit more broadened. Unfortunately, no higher magnetic field was available to drive the magnetization into saturation.

tion. However, we can conclude from the large width of the peaks that the easy axis lies not orthogonal to the plane, as was the case for a pure PdNi film. No hysteresis can be made out between up and down sweeps (data not shown). This data is consistent with the results obtained for pure Pd strips with the same geometry [73].

Fig. 8.5a shows measurements for different strips with varying angle relative to H in the wafer plane. All data are normalized by the maximum resistance, R_0 , that appears for $B = 0$ T. In the strip that is aligned with H (labelled 0°), the resistance is constant save for a relatively sharp switching at low field, whose origin we discuss in the next paragraph. The largest change in R/R_0 occurs for a strip forming an angle of 90° with H and amounts to about 2.4%. The data implies that the easy axis of the magnetic film is **inplane** and **parallel** to the strip, and therefore to the current I . Fig. 8.5b demonstrates that $\rho(\theta)$ follows Eq. 8.1. Again, independent magnetization measurements with extended films of the same material are in agreement with this data [76].

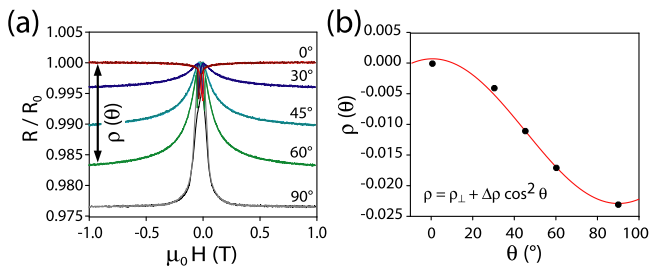


Figure 8.5: **a** Different measurements for inplane external magnetic field normalized by the maximum resistance value, R_0 . **b** Fit to the expected \cos^2 dependency.

We can analyse the individual curves in detail by looking at Fig. 8.6a-e. We notice sharp, hysteretic dips at low field in all curves save for 90° . Measurements with pure Co films show qualitatively identical results [73]. The explanation we propose for these switches is illustrated in Fig. 8.6i-iv, for an angle of 45° between H and I . A black arrow stands for H , while the magnetization of the film itself is represented by a red arrow. We assume the easy axis to point along I , so as H decreases from Fig. 8.6i to ii, the magnetization rotates until it lies parallel to the strip orientation. From Fig. 8.6ii to iii, the magnetization performs a flip of 180° , jumping from one direction of its easy axis to the opposite one in order to decrease the angle to H . Afterwards, it starts rotating away from I , until it points

completely in the direction of H again (Fig. 8.6iv). The absence of such a narrow dip in Fig. 8.6e agrees with this explanation, because in this case, a magnetization reversal as described above would not change the angle (90°) between H and the magnetization. Since all of these switches are not infinitely sharp, and especially since such a switch can be observed for an angle of 0° , we must assume that the film includes several magnetic domains that rotate/switch independently. It is also well possible that the easy axis has a finite component pointing out of the wafer plane, such that a certain degree of rotation is unavoidable with our setup geometry.

8.7 Summary

We present AMR measurements for thin strips of two different materials, PdNi and PdNi/Co. The motivation of this work was to learn more about the magnetic characteristics of these strips as prospective contact materials for SWCNT devices. From a qualitative interpretation of our results, we can draw a number of conclusions:

- In both devices, an AMR signal is clearly visible and can be explained in the framework of established phenomenological descriptions [77].
- In our samples, the easy axis of PdNi stands approximately **orthogonal** to the wafer plane, while that of Co is **inplane** and **parallel** to the strip.
- For PdNi, the maximum AMR signal $\rho(\theta)$ is seen for $\theta = 0^\circ$ and amounts to nearly **2%**. For PdNi/Co, the signal reaches **2.4%** and occurs when $\theta = 90^\circ$.

The easy axis orientation parallel to the strip and the larger AMR signal show that a Co top layer improves the magnetic characteristics of the film. Indeed, pure Co leads are successfully used for graphene spintronics [75]. For SWCNT devices, however, Co leads suffer from bad contact and low yield, which is why a PdNi/Co double layer appears promising [76]. By looking at the magnetic films only, we conclude that such a double layer has the same advantageous properties as a pure Co film. Unfortunately, we cannot be certain that the magnetization of the PdNi layer follows that of the Co layer completely. The suitability of these films for spintronics experiments with SWCNT will also depend on parameters that are beyond the scope of this work.

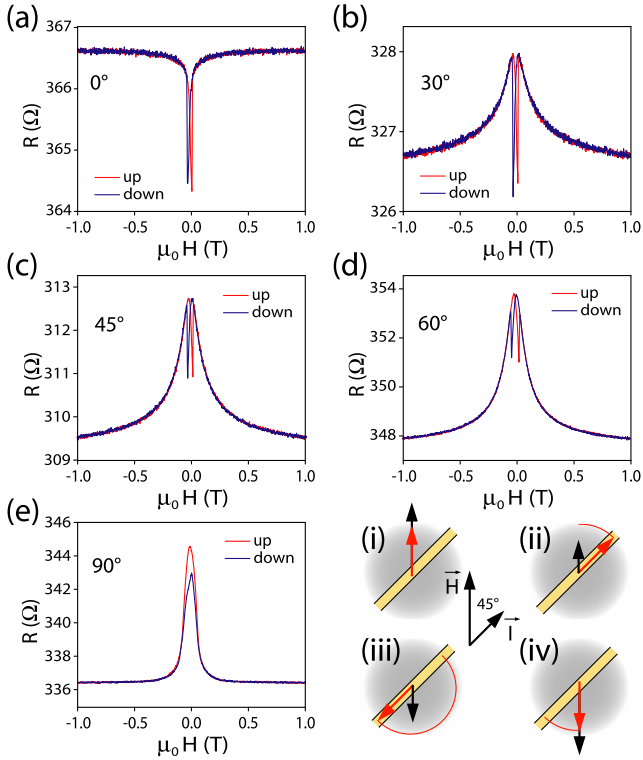


Figure 8.6: a-e The narrow dip at low magnetic field is easier to follow when the curves of Fig. 8.5a are plotted individually. i-iv The sharp switch at low applied field (H) can be explained with a magnetization reversal from one direction of the easy axis (ii) to the other one (iii) while H is swept through zero and to negative values (corresponding to an arrow in the downwards direction).

Bibliography

- [1] S. Iijima, *Nature* **354**, 56 (1991).
- [2] C. Schönberger, *Semiconductor Science and Technology* **21**, 1 (2006).
- [3] T. W. Ebbesen et al., *Nature* **382**, 54 (1996).
- [4] K. Tsukagoshi, B. W. Alphenaar, and H. Ago, *Nature* **401**, 572 (1999).
- [5] A. Y. Kasumov et al., *Science* **284**, 1508 (1999).
- [6] N. Hamada, S. Sawada, and A. Oshiyama, *Physical Review Letters* **68**, 1579 (1992).
- [7] S. J. Tans et al., *Nature* **386**, 474 (1997).
- [8] M. R. Buitelaar, A. Bachtold, T. Nussbaumer, M. Iqbal, and C. Schönberger, *Physical Review Letters* **88**, 156801 (2002).
- [9] A. Bachtold et al., *Physical Review Letters* **84**, 6082 (2000).
- [10] R. Landauer, *IBM J. Res. Dev.* **1**, 223 (1957).
- [11] M. Büttiker, *Physical Review Letters* **57**, 1761 (1986).
- [12] S. Heinze et al., *Physical Review Letters* **89**, 106801 (2002).
- [13] M. Kastner, *Physics today* **46**, 24 (1993).
- [14] R. Hanson, L. P. Kouwenhoven, J. R. Petta, S. Tarucha, and L. M. K. Vandersypen, *Reviews of Modern Physics* **79**, 1217 (2007).

- [15] J. Kondo, *Progress of Theoretical Physics* **32**, 37 (1964).
- [16] L. P. Kouwenhoven and L. Glazman, *Physics World* **14**, 33 (2001).
- [17] D. Goldhaber-Gordon et al., *Physical Review Letters* **81**, 5225 (1998).
- [18] J. Nygard, D. H. Cobden, and P. E. Lindelof, *Nature* **408**, 342 (2000).
- [19] Y. Meir, N. S. Wingreen, and P. A. Lee, *Physical Review Letters* **70**, 2601 (1993).
- [20] C. Karrasch, A. Oguri, and V. Meden, *Physical Review B* **77**, 024517 (2008).
- [21] C. W. J. Beenakker, *Physical Review B* **46**, 12841 (1992).
- [22] J. Bardeen, L. N. Cooper, and J. R. Schrieffer, *Physical Review* **108**, 1175 (1957).
- [23] M. Tinkham, *Introduction to Superconductivity*, McGraw-Hill, 1996.
- [24] N. W. Ashcroft and N. D. Mermin, *Solid State Physics*, Brooks Cole, 1976.
- [25] W. Buckel and R. Kleiner, *Supraleitung: Grundlagen und Anwendungen*, Wiley-VCH, 2004.
- [26] W. Belzig, A. Brataas, Y. V. Nazarov, and G. E. W. Bauer, *Physical Review B* **62**, 9726 (2000).
- [27] W. Meissner and R. Ochsenfeld, *Naturwissenschaften* **21**, 787 (1933).
- [28] A. L. Yeyati, J. C. Cuevas, A. López-Dávalos, and A. Martín-Rodero, *Physical Review B* **55**, R6137 (1997).
- [29] G. J. A. N. Bratus, V. S. Shumeiko, and G. Wendin, *Physical Review B* **60**, 1382 (1999).
- [30] M. R. Buitelaar et al., *Physical Review Letters* **91**, 057005 (2003).
- [31] P. G. de Gennes, *Reviews of Modern Physics* **36**, 225 (1964).
- [32] A. F. Andreev, *Sov. Phys. JETP* **19**, 1228 (1964).
- [33] M. Octavio, M. Tinkham, G. E. Blonder, and T. M. Klapwijk, *Physical Review B* **27**, 6739 (1983).

- [34] V. L. Ginzburg and L. D. Landau, Zh. Eksperim. i. Teor. Fiz. **20**, 1064 (1950).
- [35] B. D. Josephson, Reviews of Modern Physics **36**, 216 (1964).
- [36] C. W. J. Beenakker and H. van Houten, Physical Review Letters **66**, 3056 (1991).
- [37] P. Joyez, *The single Cooper pair transistor: a macroscopic quantum device*, PhD thesis, Université Paris 6, 1995.
- [38] P. Jarillo-Herrero, J. A. van Dam, and L. P. Kouwenhoven, Nature **439**, 953 (2006).
- [39] H. I. Jorgensen, T. Novotný, K. Grove-Rasmussen, K. Flensberg, and P. E. Lindelof, Nano Letters **7**, 2441 (2007).
- [40] J. M. Martinis and R. L. Kautz, Physical Review Letters **63**, 1507 (1989).
- [41] H. Dai, Accounts of Chemical Research **35**, 1035 (2002).
- [42] J. Furer, *Growth of single-wall carbon nanotubes by chemical vapor deposition for electrical devices*, PhD thesis, University of Basel, 2006.
- [43] Y. Hu et al., Nature Nanotechnology **2**, 622 (2007).
- [44] *Oxford Instruments Superconductivity, Kelvinox Dilution Refrigerator and Superconducting Magnet System. Operator's Handbook (Oxford Instruments, Tubney Woods Abington, UK, 2001)*.
- [45] H. Bluhm and K. A. Moler, Review of Scientific Instruments **79**, 014703 (2008).
- [46] M. Gräber, *Accessing the quantum world through electronic transport in carbon nanotubes*, PhD thesis, University of Basel, 2006.
- [47] A. Eichler et al., Physical Review Letters **99**, 126602 (2007).
- [48] M. R. Buitelaar, T. Nussbaumer, and C. Schönberger, Physical Review Letters **89**, 256801 (2002).
- [49] J. Nygard et al., arXiv:cond-mat/0410467 (2004).
- [50] E. Vecino, M. R. Buitelaar, A. Martín-Rodero, C. Schönberger, and A. L. Yeyati, Solid State Communications **131**, 625 (2004).

- [51] G. Kotliar and A. E. Ruckenstein, *Physical Review Letters* **57**, 1362 (1986).
- [52] T. Sand-Jespersen et al., *Physical Review Letters* **99**, 126603 (2007).
- [53] A. Eichler et al., *Physical Review B* **79**, 161407(R) (2009).
- [54] J.-P. Cleuziou, W. Wernsdorfer, V. Bouchiat, T. Ondarcuhu, and M. Monthieux, *Nature Nanotechnology* **1**, 53 (2006).
- [55] K. Grove-Rasmussen, H. I. Jorgensen, and P. E. Lindelof, *New Journal of Physics* **9**, 124 (2007).
- [56] C. Buizert, A. Oiwa, K. Shibata, K. Hirakawa, and S. Tarucha, *Physical Review Letters* **99**, 136806 (2007).
- [57] J. A. van Dam, Y. V. Nazarov, E. P. A. M. Bakkers, S. D. Franceschi, and L. P. Kouwenhoven, *Nature* **442**, 667 (2006).
- [58] L. I. Glazman and K. A. Matveev, *JETP Letters* **49**, 659 (1989).
- [59] W. Liang et al., *Nature* **411**, 665 (2001).
- [60] H. I. Jorgensen, K. Grove-Rasmussen, T. Novotný, K. Flensberg, and P. E. Lindelof, *Physical Review Letters* **96**, 207003 (2006).
- [61] W. Lu, J. Xiang, B. P. Timko, Y. Wu, and C. M. Lieber, *Proc. Natl. Acad. Sci. USA* **102**, 10046 (2005).
- [62] J. Xiang, A. Vidan, M. Tinkham, R. M. Westervelt, and C. M. Lieber, *Nature Nanotechnology* **1**, 208 (2006).
- [63] Y. Hu, J. Xiang, G. Liang, H. Yan, and C. M. Lieber, *Nano Letters* **8**, 925 (2008).
- [64] N. Mason, M. J. Biercuk, and C. M. Marcus, *Science* **303**, 655 (2004).
- [65] S. Sapmaz, C. Meyer, P. Beliczynski, P. Jarillo-Herrero, and L. P. Kouwenhoven, *Nano Letters* **6**, 1350 (2006).
- [66] G. Götz, G. A. Steele, W.-J. Vos, and L. P. Kouwenhoven, *Nano Letters* **8**, 4039 (2008).
- [67] H. O. H. Churchill et al., *Physical Review Letters* **102**, 166802 (2009).
- [68] Y.-J. Doh, S. de Franceschi, E. P. A. M. Bakkers, and L. P. Kouwenhoven, *Nano Letters* **8**, 4098 (2008).

- [69] R. C. Dynes, J. P. Garno, G. B. Hertel, and T. P. Orlando, *Physical Review Letters* **53**, 2437 (1984).
- [70] A. N. Pasupathy et al., *Science* **306**, 86 (2004).
- [71] J. R. Hauptmann, J. Paaske, and P. E. Lindelof, *Nature Physics* **4**, 373 (2008).
- [72] L. Hofstetter et al., arXiv:0910.3237v1 (2009).
- [73] J. Hyötylä, Anisotropic magnetoresistance in thin magnetic films, Project work, University of Basel, 2008.
- [74] S. Sahoo et al., *Nature Physics* **1**, 99 (2005).
- [75] N. Tombros, C. Jozsa, M. Popinciuc, H. T. Jonkman, and B. J. van Wees, *Nature* **448**, 571 (2007).
- [76] G. Gunnarsson, *Transport Measurements on Single Wall Carbon Nanotube Multiterminal Devices with Normal and Ferromagnetic Contacts*, PhD thesis, University of Basel, 2008.
- [77] T. R. McGuire and R. I. Potter, *IEEE Transactions on Magnetics* **11**, 1018 (1975).
- [78] A. Zorin, *Review of Scientific Instruments* **66**, 4296 (1995).
- [79] K. Montavon, B. Heimann, and M. Steinacher, Inhouse construction, department for physics at the university of basel.

Appendix A

Fabrication and Measurement Information

- **Wafer characteristics**

<i>Substrate material</i>	highly doped Si
<i>Dopant</i>	p, Boron
<i>Resistivity</i>	0.003-0.005 Ωm
<i>Thickness of SiO₂ layer</i>	400 nm
<i>Size of wafer pieces</i>	1 cm x 1 cm

- **Cleaning procedure**

1. Sonicate in Acetone (10 min)
2. Rinse in 2-propanol and dry
3. Place in UVO-cleaner for 10 minutes (model 42 by Jelight Company)
4. Place in Oxygen Plasmalab^{80Plus} by Oxford:

<i>gas</i>	O ₂
<i>flow</i>	16
<i>pressure</i>	25 mTorr
<i>RF power</i>	200
<i>time</i>	30 s

- **CVD catalyst**

1. Dissolve 30 mg of Al₂O₃ in 20 ml 2-propanol
2. Dissolve 93 mg of Fe(NO₃)₃·9H₂O in 20 ml 2-propanol

3. Dissolve 27 mg of MoO_2Cl_2 in 20 ml 2-propanol
4. Sonicate these three stock solutions for ~ 12 h
5. Mix 0.5 ml of each stock solution together with 18.5 ml of 2-propanol to a total volume of 20 ml
6. Sonicate final product for ~ 12 h

• **CVD process**

1. Place wafer piece in UVO-cleaner for 10 minutes (model 42 by Jelight Company)
2. Sonicate catalyst for 2 h
3. Leave catalyst standing for 10 minutes to let biggest catalyst particles sediment
4. Apply 1-2 drops of catalyst to wafer while it is spinning at 4000 rpm
5. Place wafer in center of CVD oven on spoon (quartz glass)
6. Seal tube
7. Open gas valves to Ar(104 l/h), CH_4 (44 l/h), and H_2 (8 l/h)
8. flush for 2 minutes
9. Close valves to CH_4 and H_2
10. Switch furnace on, target temperature $T_{tar} = 950$ °C
11. When $T = T_{tar}$, open H_2 , close Ar, open CH_4
12. Wait for 10 minutes
13. Close CH_4 , switch furnace off
14. When $T = 550$ °C, close H_2
15. When $T = 330$ °C, close Ar, take out wafer

• **E-beam lithography**

1. Cover wafer with PMMA/MA 33 % (AR-P 617 from ALLRESIST, undiluted)
2. Spin to obtain 100 nm film (4000 rpm, time= 40 s, ramp= 4 s)
3. bake out on hotplate (200 °C for 10 minutes)
4. Cover wafer with PMMA (AR-P 671.09 950K from ALLRESIST, diluted)
5. Spin to obtain 200 nm film (4000 rpm, time= 40 s, ramp= 4 s)

6. bake out on hotplate (180 °C for 10 minutes)
7. Write small/large structures with SEM (Zeiss Supra 40):

<i>Working distance</i>	17 mm
<i>Acceleration voltage</i>	20 kV
<i>Writefield_{small}</i>	100 μm
<i>Aperture_{small}</i>	10 μm
<i>Area dose_{small}</i>	240 μAs/cm ²
<i>Line dose_{small}</i>	1000 pAs/cm (expose lines twice)
<i>Writefield_{large}</i>	2000 μm
<i>Aperture_{large}</i>	120 μm
<i>Area dose_{large}</i>	240 μAs/cm ²
8. Develop for 90 s in 4-Methyl-2-pentanone (25 %), 2-propanol (75 %)
9. Rinse in 2-propanol and dry
10. Evaporation in Balzers-Pfeiffer PLS 500:

<i>Sample temperature</i>	0 °C
<i>Base pressure</i>	10 ⁻⁷ mbar
<i>Rate</i>	2-3 Å/s
11. Lift-off in Acetone
12. Rinse in 2-propanol and dry

• **ALD process**

1. Mount sample in ALD chamber, pump
2. Heat up to $T_{ALD} = 225$ °C
3. Start program:

step	command	number	time
0	pulse	0	0.1
1	wait	-	10
2	pulse	2	0.04
3	wait	-	10
4	goto	0	50

4. Wait until $T = 80$ °C
5. Vent chamber, take out sample

- **Bonding**

<i>Model</i>	4523 AD by CMTec
<i>Power₁</i>	2.31
<i>Time₁</i>	3.9
<i>Force₁</i>	1.2
<i>Power₂</i>	1.68
<i>Time₂</i>	5.9
<i>Force₂</i>	0.8
<i>Tail</i>	1.9
<i>Tear</i>	3.3
<i>Mode</i>	manual

- **Stanford Research SR 830 DSP lock-in amplifier**

<i>Frequency</i>	77.77 Hz
<i>Time constant</i>	300 ms
<i>Signal input</i>	A-B, ground
<i>Input impedance</i>	10 M Ω
<i>Reserve</i>	normal
<i>Coupling</i>	AC
<i>AUX Output impedance</i>	< 1 Ω

- **Hewlett Packard HP 3245A universal source**

<i>Output impedance</i>	< 0.5 Ω
-------------------------	----------------

- **Yokogawa YK 7651 programmable DC source**

<i>Output impedance</i>	\leq 2 m Ω
-------------------------	---------------------

- **Stanford Research SR 560 low-noise preamplifier**

<i>Input impedance</i>	100 M Ω
<i>Source</i>	A-B
<i>Gain</i>	10
<i>Coupling</i>	DC
<i>Filter</i>	low-pass (100 Hz)
<i>Filter slope</i>	18 dB
<i>Output impedance</i>	50 Ω

- **Inhouse built voltage divider**

<i>R₁</i>	10 k Ω
<i>R₂</i>	100 Ω

- **Inhouse built high gain I/V converter**

<i>Gain</i>	10 ⁹
<i>Input coupling</i>	DC
<i>Input impedance</i>	\sim 5.6 k Ω at 77 Hz
<i>Typical V_{SD} offset</i>	0.1 mV

- **DL Instruments 1211 current preamplifier**

<i>Gain</i>	10^8
<i>Rise time</i>	10 ms
<i>Input resistance</i>	2 k Ω
<i>Typical V_{SD} offset</i>	0.17 mV

- **Inhouse built voltage preamplifier**

<i>Gain</i>	100
<i>Input impedance</i>	

- **Π -filter**

<i>Attenuation at 0.3 MHz</i>	40-60 dB
-------------------------------	----------

- **Resistive coax wires¹**

<i>Attenuation at 1 GHz</i>	60 dB/m
<i>Attenuation at 10 GHz</i>	200 dB/m

- **Tapeworm filter[79]**

<i>Attenuation at 1 GHz</i>	60 dB (estimated)
<i>DC resistance</i>	64 Ω

- **Oxford superconducting coil magnet**

<i>Maximum field at 4.2 K</i>	8 T
<i>Current decay in persistent mode</i>	10^{-4} /h
<i>Homogeneity over 10 mm sphere</i>	10^{-3}

¹Attenuation values from [78]

Publication List

Publications in journals

- *Even-odd Effect in Andreev Transport through a Carbon Nanotube Quantum Dot*
A. Eichler, M. Weiss, S. Oberholzer, A. Levy-Yeyati, J. C. Cuevas, A. Martín-Rodero, and C. Schönberger, PRL **99**, 126602 (2007)
- *Tuning the Josephson current in carbon nanotubes with the Kondo effect*
A. Eichler, R. Deblock, M. Weiss, C. Karrasch, V. Meden, C. Schönberger, and H. Bouchiat, PRB **79**, 161407(R) (2009)

Poster contributions

- *Andreev Spectroscopy of a CNT Quantum Dot*
A. Eichler, M. Weiss, S. Oberholzer, and C. Schönberger, poster contribution for the seminar “Spin Physics of Superconducting Heterostructures” in Bad Honnef, December 2006
- *Even-odd Effect in Andreev Transport through a Carbon Nanotube Quantum Dot*
A. Eichler, M. Weiss, S. Oberholzer, A. Levy-Yeyati, J. C. Cuevas, A. Martín-Rodero, and C. Schönberger, poster at the “Frontiers in Nanoscale and Technology” workshop in Basel, January 2008
- *Spin physics in SWCNT quantum dots with ferromagnetic and superconducting leads*
G. Gunnarsson, A. Eichler, H. Aurich, M. Weiss, J. Trbovic, and C. Schönberger, poster for the NCCR review panel, April 2008

Oral presentations

- *Andreev Spectroscopy of Single-Walled Nanotubes*
seminar talk at the University of Konstanz, 30 November 2006
- *Modulation of Andreev reflections and Josephson current by the Kondo effect in SWCNT quantum dots*
talk at the annual meeting of the Swiss Physical Society in Geneva, 27 March 2008
- *Modulation of Andreev reflections and Josephson current by the Kondo effect in SWCNT quantum dots*
presentation at the European HYSWITCH project meeting in Paris, 4 April 2008
- *Carbon Nanotubes as Quantum Supercurrent Transistors*
presentation at the workshop “The Global Challenges - How can Nanotechnology help?” in Venice, 21 April 2008
- *Tuning the Josephson Current in CNT with the Kondo Effect*
seminar talk at the seminar “Unconventional Proximity Effects in Novel Materials” in Bad Honnef, 14 November 2008
- *Tuning the Josephson Current in CNT with the Kondo Effect*
conference talk at the Nanotech UHA-UNIBAS conference in Mulhouse, 9 June 2009
- *Supercurrents through single level Kondo impurities in carbon nanotubes*
invited talk at the annual meeting of the “GDRI: Graphene and Nanotubes” in Coma-ruga, Spain, 19-23 October 2009

Curriculum Vitae

Alexander Timothy Eichler
Born 18 April 1981 in Fulford, York, GB

Education

- August 1997 - December 2000
Gymnasium (high school) Oberwil, CH Matura type A (Greek and Latin)
- October 2001 - September 2004
Bachelor of Science in Physics at the University of Basel
- October 2004 - May 2006
Master of Science in Physics at the University of Basel
Master thesis under the supervision of Prof. C. Schönberger: “Electrical transport through a carbon nanotube quantum dot coupled to superconducting leads”
- June 2006 - December 2009
PhD thesis at the University of Basel under the supervision of Prof. C. Schönberger: “Quantum Dot Josephson Junctions in the Kondo Regime”

Professional positions

- August 2005 - July 2006
Physics teacher at a Gymnasium (high school) in Basel
- June 2006 - February 2009
Research assistant in the group of Prof. C. Schönberger at the Physics Department of the University of Basel

For valuable lectures during my studies I am indebted to: C. Bandle, C. Bruder, R. Buser, M. Calame, M. Grote, M. Hegner, H.-C. Im Hof, H. Kraft, B. Krusche, D. Loss, H. Mühry, B. Scarpellini, I. Sick, C. Schönenberger, L. Tauscher, F.-K. Thielemann, D. Trautmann, H. Walser, and D. Zumbühl

Acknowledgements

At this point, I am very happy to acknowledge all the people whose help and support have made this work possible. First of all, I would like to thank my supervisor, Christian Schönenberger, for his perpetual motivation and resourcefulness throughout the years. Christian, I felt privileged to work with you, and I value highly what you have done for me. Second, I owe very much to Markus Weiss, whose expertise in experimental and theoretical matters was invaluable from beginning to end. Markus, you were an esteemed and trusted colleague in the daily battle against Murphy's Law. Many thanks to Jesper Nygård for co-refereeing my thesis defense.

To all of my office mates, I offer my gratitude for countless hours of discussion and mutual support, but also for the fits of laughter we suffered together. Andreas Kleine, Lukas Hofstetter, Oren Knopfmacher, Frank Freitag, Hagen Aurich, Szabolcs Csonka, Dino Keller, and Jürg Furer filled up a considerable part of my waking time with their brilliant ideas and utter nonsense, and I am grateful for both. Further, I would like to mention the rest of the group: Michel Calame, Andreas Baumgartner, Wangyang Fu, Haichao Huang, Jelena Trbovic, Jon Agustsson, Jan Brunner, Toni Fröhlich, Alexey Tarasov, Roman Huber, Laetitia Bernard, Erasmus Bieri, Matthias Gräber, Teresa Gonzalez, Gunnar Gunnarsson, Jianhui Liao, Stefan Oberholzer, Sense Jan van der Molen, Songmei Wu, and Zheng-Ming Wu, thank you all for sharing the boiling fumes and blinking lights of the lab with me, and making my life the richer for it. Jon, why did we never construct that poultry computer?

During my project, I had the opportunity to collaborate with many scientists from abroad to whom I feel indebted. For chapter 3, we enjoyed the theoretical support of Alfredo Levy-Yeyati, Juan-Carlos Cuevas, and Alvaro Martín-Rodero from the Universidad Autónoma de Madrid. Alfredo, thank you also for the chance to visit the beautiful city of Madrid. For chapter 4, we worked together with Richard Deblock and Hélène Bouchiat from the LPS Orsay, Paris. Hélène and Richard, it was great being in your lab for

that month, I learned a lot from you both. On the theory side, I am grateful to Christoph Karrasch and Volker Meden from the University of Aachen. Christoph, it was a pleasure meeting you at Bad Honnef. The sample used in chapter 5 was fabricated in collaboration with Yongjie Hu and Charles Lieber at Harvard University. Yongjie, thank you for your tireless effort throughout that month. The experiment presented in chapter 8 was designed and analysed together with Gunnar Gunnarsson and Jelena Trbovic. For valuable discussion and input at several stages of the project, I would like to thank W. Belzig, S. Guéron, T. Novotný, J. Paaske, Y. Avishai, B. Röthlisberger, C. Bruder, and Elke Scheer.

Of course, experimental science would be almost impossible without the help of our mechanical and electrical workshops. I gratefully acknowledge the high quality work that we depended on in so many instances. A special mention must go to Daniel Sacker and Dominik Sifrig for their vital role in our lab adventures. Similarly, I felt fortunate to have all administrative problems solved by Barbara Kammermann and Astrid Kalt. I can still hear the phrase “Don’t worry, we took care of that long ago.”

Additional thanks go to Martina Eichler for her help in mastering the occasional English problem, and for proofreading part of the thesis.

Finally, I dedicate this work to you, Nadine. Your loving presence has turned my world upside down, and I look forward to a long, bright future at your side. Thank you.